The role of interneuronal networks in hippocampal ripple oscillations

Frequency dynamics and response to GABA modulators

Dissertation

zur Erlangung des akademischen Grades
doctor rerum naturalium
(Dr. rer. nat.)
im Fach Biologie

eingereicht an der
Lebenswissenschaftlichen Fakultät
der Humboldt-Universität zu Berlin

von
M.Sc. José Ramón Donoso Leiva

Präsidentin der Humboldt-Universität zu Berlin
Prof. Dr.-Ing. Dr. Sabine Kunst

Dekan der Lebenswissenschaftlichen Fakultät
Prof. Dr. Richard Lucius

Gutachter: 1. Prof. Dr. Richard Kempter

2. Prof. Dr. Imre Vida

3. Prof. Dr. Roger Traub

Tag der mündlichen Prüfung: 26. Juli, 2016

Abstract

Hippocampal sharp wave-ripples (SWRs) are electrographic events that have been implicated in memory consolidation. A SWR is characterized by a fast (>90 Hz) oscillation, the ripple, superimposed on a slow (<30 Hz) sharp wave. In vivo, the fast component can express frequencies either in the ripple range (140–200 Hz) or fast-gamma range (90–140 Hz). Episodes in both bands exhibit intra-ripple frequency accommodation (IFA). In vitro, ripples are frequency-resistant to GABA modulators. These features constrain the type of mechanisms underlying the generation of the fast component. A prominent hypothesis proposes that a recurrent network of parvalbumin-immunoreactive basket cells (PV^+BC) is responsible for setting the ripple frequency. The focus of the present thesis is on testing to which extent the PV^+BC network can account for the aforementioned features of SWRs, which remain unexplained. Here, I simulated and analyzed a physiologically constrained *in silico* model of the PV^+BC network in CA1 under different conditions of excitatory drive. The response of the network to transient excitation exhibits both IFA in the ripple band and frequency resistance to GABA modulators. The expression of IFA in the fast gamma band requires the involvement of pyramidal cells in a closed loop with the PV^+BC network. The model predicts a peculiar relationship between the instantaneous frequency of ripples and the time course of the excitatory input to CA1. This prediction was confirmed in an *in vitro* model of SWRs. Additionally, I study the involvement of oriens lacunosum-moleculare interneurons (O-LM) during SWRs *in vitro*. I characterize the excitatory currents received by O-LM cells during SWRs and investigate the factors that determine their recruitment. Together, these results clarify several previously unexplained characteristics of ripple oscillations, advancing our understanding of the hippocampal processes involved in memory consolidation.

Zusammenfassung

Hippokampale Sharp Wave-Ripples (SWRs) sind rhythmische elektrografische Ereignisse, die für die Konsolidierung von Erinnerungen eine Rolle spielen. Eine SWR ist durch eine schnelle Oszillation (>90 Hz, 'ripple') charakterisiert, die sich mit der langsameren 'sharp wave' (<30 Hz) überlagert. In vivo kann die Frequenz der schnellen Oszillation im ripple-Bereich (140–200 Hz) oder auch im schnellen Gamma-Bereich liegen (90–140 Hz). Für Episoden aus beiden Frequenzbereichen kann die sogenannte 'intra-ripple frequency accommodation' (IFA) beobachtet werden. In vitro ist die ripple-Frequenz resistent gegenüber GABA-Modulatoren. Alle diese Eigenschaften dienen als Beschränkungen für Modelle, die das SWR Phänomen erklären können. Eine weit verbreitete Hypothese besagt, dass ein rekurrentes Netzwerk von Parvalbumin-immunoreaktiven Korbzellen (parvalbumin-immunoreactive basket-cells; PV^+BC) für die ripple-Frequenz verantwortlich ist. Es liegt im Fokus dieser Arbeit, zu testen, inwieweit das PV^+BC Netzwerk die erwähnten, bisher unerklärten, ripple-Eigenschaften erklären kann. Ich analysiere dazu ein in-silico Model des PV^+BC Netzwerks für verschiedene Zustände von exzitatorischem Input. Wenn das Netzwerk durch eine schnelle Folge von exzitatorischen Pulsen getrieben wird, kann in der transienten Antwort IFA beobachtet werden. Die IFA ist hier jedoch auf das ripple-Frequenzband beschränkt und die Frequenz ist resistent gegenüber GABA-Modulatoren. Um IFA im schnellen Gamma-Bereich beobachten zu können, benötigt das Netzwerk eine Rückkopplung mit Pyramidalzellen. Das Model sagt vorher, dass IFA während der ansteigenden Phase der Exzitation das Frequenzmaximum erreicht. Ich bestätige diese Vorhersage in einem in-vitro Model für SWRs. Weiterhin untersuche ich die Beteiligung von oriens lacunosum-moleculare (O-LM) Interneuronen während der SWRs in vitro. Ich charakterisiere die exzitatorischen Ströme, die O-LM Zellen während der SWRs empfangen und untersuche die Faktoren, die ihre Einbeziehung bestimmen. Zusammengenommen erklären diese Resultate einige bisher unerklärte Eigenschaften von ripple-Oszillationen. Dies erweitert unser Verständnis hippokampaler Prozesse, die an der Konsolidierung von Erinnerungen beteiligt sind.

Contents

1 Introduction

The sound of a beating heart can provide valuable information about the operation of this vital organ. Even for a naive listener, the rhythmic nature of its beating reveals a cyclical mechanical process taking place. If we are familiar with the heart function and anatomy, we can associate the sounds with the closure of different valves and thereby identify different phases of the cardiac cycle. A trained ear can go even further with the help of a stethoscope. By placing the instrument at different locations on the chest, and adjusting its diaphragm to emphasize high-pitched or low-pitched sounds, it is possible to auscultate different components of the cardiac clockwork and identify a wide variety of dysfunctions. As the mechanical action of the heart is uncovered by the rhythmic sounds it generates, an important aspect of the operation of the brain can be revealed by its electrical activity.

The hippocampus, a part of the brain that is critically involved in the formation of new memories, generates a variety of rhythmic electrical signals that appear associated to different behavioral states. By 'listening' to these rhythms and figuring out the anatomical components generating them, we can get insights on the processes taking place in the hippocampus when performing its function.

The present thesis concerns with the physiological mechanisms underlying sharp wave-ripples (SWR); a peculiar rhythm that can be observed in the hippocampus during deep sleep and quiet wakefulness. These transient, high-frequency ($\sim$200 Hz) oscillations have been implicated in memory consolidation and other cognitive functions. In the present chapter, I briefly introduce some fundamental concepts regarding network oscillations, hippocampal function and anatomy, the role of SWRs in cognitive function and the basic circuit elements that are relevant for the forthcoming chapters.

1.1 Network oscillations and brain function

In the brain, it is possible to record a variety of electrical signals both at the scalp and intracranially. Such signals can exhibit different oscillatory patterns depending on the activity in which the animal is engaged. For example, theta (4–12 Hz) rhythms have been shown to be enhanced across several areas of the neocortex when a human subject is required to memorize a list of items (Meltzer et al., 2008). Gamma (30–90 Hz) is predominant during attentive states such as when a predator is lurking its pray (Bouyer et al., 1981). Beta rhythms (15–30 Hz) increase their power during preparation of a movement, and decreases it at the onset of the movement execution (Jasper and Penfield, 1949). Other oscillations are predominant when the animal is not actively engaged with the environment, these are the so called 'default' patterns of cortical activity (Ganzetti and Mantini, 2013). For example, during deep stages of sleep, brain activity is characterized by a wide-spread slow wave ($<$ 1Hz) pattern. Such activity has been shown to be relevant for the consolidation of recently acquired memories (Huber et al., 2004).

Several lines of evidence point at the functional relevance of brain rhythms (Buzsáki and Draguhn, 2004): (1) their power and incidence have been shown to be correlated with per-

formance on different cognitive tasks (Klimesch, 1999; Varela et al., 2001; Sederberg et al., 2007), (2) alterations of these rhythms appear associated with a variety of neuropsychiatric conditions (Schnitzler and Gross, 2005; Başar and Güntekin, 2008; Buzsáki and Watson, 2012) and (3), their frequencies in relation to behavior are largely conserved across mammalian species, regardless of brain size (Buzsáki and Wang, 2012; Buzsáki and Moser, 2013). It is therefore important to uncover the physiological mechanisms giving rise to these oscillations in order to understand their role in supporting brain function.

Brain rhythms (henceforth, network oscillations) reflect the synchronized activity of many cells. The degree of synchrony of spiking activity can be functionally relevant because it can modulate the impact this activity will have on its postsynaptic targets (Masquelier et al., 2009). Remarkably, the spiking of principal cells is typically constrained within a small range of phases of the ongoing oscillation (O'Keefe and Recce, 1993; Senior et al., 2008). Such temporally organized activity allows the emergence of functional groups of principal cells that fire together. Such 'cell assemblies' (Hebb, 1949) can be further organized into sequences which can be relevant for cognitive functions as will be discussed in section 1.2.3.

The temporally organized firing during network oscillations is mediated, in most cases, by inhibitory activity. An oscillatory wave of inhibition can provide windows of opportunity in which cells are more likely to fire (Whittington et al., 2000). The generation of such inhibitory waves can be achieved by several mechanisms that might involve interactions between interneurons only (Bartos et al., 2007; Schlingloff et al., 2014), and both interneurons and principal cells (Bartos et al., 2007; Stark et al., 2014). However, it is also possible that some forms of oscillatory activity are mediated by interactions between principal cells alone (Draguhn et al., 1998; Traub et al., 1999; Memmesheimer, 2010).

1.2 The role of the hippocampus in brain function

Mammalian species exhibit a huge diversity in terms of habitats, means of locomotion, preferred diets, and social structures. Such diversity imposes different demands for cognitive resources. For some animals vision might be more relevant for their survival; for some others it would be olfaction or hearing. The requirement of higher order cognitive functions might also vary across species. For example, the ability to recognize peers is more relevant for social animals than for non social ones, and proficiency in navigation might be more critical for animals that store their food in hidden places than for those that forage. Consistent with such diversity of 'cognitive demand', the mammalian neocortex exhibits a large variety in terms of structure and connectivity.

In spite of this diversity, however, there is a curved cylindrical structure located at the rim of the mammalian neocortex that remarkably conserves its structure and internal connectivity across species: the hippocampus (Manns and Eichenbaum, 2006). The connectivity between this structure and the rest of the cortex suggests that information from virtually all neocortical regions is funneled to the hippocampus via its adjacent perirhinal and entorhinal cortices (Brown and Aggleton, 2001; Van Strien et al., 2009). This information is processed and conveyed back to the neocortex via the same parahippocampal structures. This puts the hippocampus in a privileged position where it can associate different kinds of highly processed information stemming from different sensory modalities, and use this information to affect or modify its source structures (Buzsaki, 2006). What could be the role of the hippocampus in brain function?

1.2.1 Hippocampus and memory

In humans, damage to the hippocampus and surrounding structures result in profound memory problems. Studies on patients with surgical removal of the hippocampus and some adjacent structures showed that the aquisition of new episodic-declarative knowledge was seriously compromised. However, patients conserved and could use some of their experiences prior to surgery (Scoville and Milner, 2000).

Remarkably, patients with hippocampal lesions exhibit a temporally graded pattern of retrograde amnesia. Memories from earlier in life are easier to recall than those acquired later in life (Ribot and Fitzgerald, 1883; Butters and Cermak, 1988). This lead to the hypothesis of a gradual transfer of labile information from the hippocampus to more permanent traces in the neocortex. In support, animal studies have shown that successful retrieval of remote memories become gradually independent of the hippocampus and more dependent on neocortical areas (Maviel et al., 2004; Wang et al., 2009).

1.2.2 Oscillations in the hippocampal formation

We have identified the hippocampal formation as a biological substrates that plays a crucial role in memory formation. How can we now disclose the operations of the hippocampal circuit when performing its function? As discussed in section 1.1, network oscillations can provide valuable information about the mode of operation of the circuit.

The hippocampal tissue displays a variety of oscillations in its extracellular field. These oscillations correlate with different behavioral states and have been related to different cognitive functions. Theta (4–12 Hz) and gamma (30–90 Hz) rhythms co-occur with periods of interactive behavior such as active exploration of the environment (O'Keefe and Recce, 1993; Bragin et al., 1995). During resting periods and slow wave sleep, on the other hand, short-lived events consisting in fast oscillations superimposed on slower potential deflections (sharp wave) conform what is called a sharp wave-ripple complex (SWR)(Buzsáki, 1986; Buzsáki et al., 1992).

1.2.3 Traces of previous experience in hippocampal activity

Remarkably, there is evidence that the activity of hippocampal principal cells can retain traces of previous experience (Fig. 1.1). Recordings from neurons in the hippocampus during exploratory behavior have shown that principal cells respond to specific locations in the environment. When a rat transverses a linear track, such 'place cells' undergo a sequential activation that corresponds to the sequence of visited places. During slow-wave sleep, the sequences experienced during waking were replayed at a much faster timescale (Lee and Wilson, 2002). Interestingly, this fast replay co-occurred with SWR events. Such replay can also appear in reverse order, co-ocurring with SWRs during awake resting periods (Foster and Wilson, 2006). Regardless of the spatial aspect of the cellular activation, fast replay during sleep showed that activity related to previous experience can be retained for later retrieval.

1.2.4 The role of sharp-wave ripples in brain function

It has been hypothesized that the fast replay observed during SWRs might play a role in the consolidation of experience-induced circuit modifications (Buzsáki, 1989). In this so called 'two-stage memory formation hypothesis' memory traces are acquired or 'encoded' during the

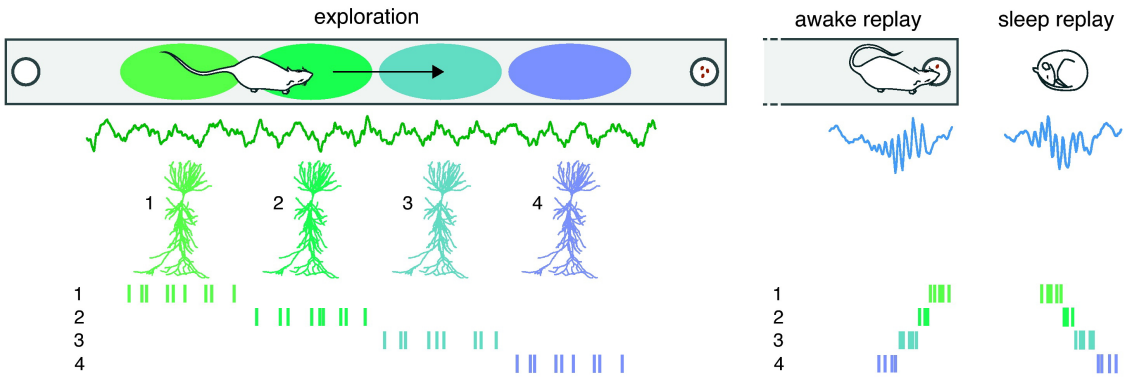

Fig. 1.1: Sharp wave-ripple (SWR)-associated neuronal replay. When a rat is running on a linear track, the local field potential in the hippocampus oscillates at theta frequency (green trace) and place cells (1–4) are successively activated as the rat enters their respective place fields (colored ellipses), yielding a sequence of activation (vertical ticks). Upon arrival at the food well, the rat stops to consume a reward and the place cell sequence reactivates in reverse order (reverse replay) during SWRs (blue trace). In subsequent slow wave sleep and quiet rest periods, place cells reactivate in the same order as during exploration (forward replay) (Girardeau et al., 2009; reproduced with permission from Elsevier).

exploratory (theta) phase. Such initially labile traces are later consolidated during resting periods and slow-wave sleep (i.e., SWR phase)(Buzsáki, 1998; Siapas and Wilson, 1998). There is evidence in support of the involvement of SWRs in memory processes. For example, the incidence of SWRs during sleep is correlated with the amount of successfully learned items in humans (Axmacher et al., 2008). Such increased incidence of SWRs during post-learning sleep has been also observed in rats (Eschenko et al., 2008). Furthermore, electrically-induced disruption of SWRs following behavioral training impaired spatial learning (Girardeau et al., 2009; Ego-Stengel and Wilson, 2010).

The fast replay observed during SWRs has been implicated in several aspects of cognition that go beyond memory consolidation (Carr et al., 2011; Buzsáki, 2015). For example, when a rat is confronted with a previously experienced track, during awake immobility, fast replay anticipates the upcoming behavioral sequence (Diba and Buzsáki, 2007). It has been suggested that such 'fast recall' might play a role in planning future trajectories (Pastalkova et al., 2008; Pfeiffer and Foster, 2013). Furthermore, SWRs-associated sequences that predict previously unexperienced place-sequences often appear during both waking and sleep (Gupta et al., 2010; Dragoi and Tonegawa, 2011). Motivated by this evidence, some authors have pointed at a putative constructive role of the hippocampus, arguing that SWRs could be implicated in the finding of new unexplored paths (Samsonovich and Ascoli, 2005; Buzsáki, 2015) and in the generation of novel solutions to non-navigational problems (Buzsáki and Moser, 2013).

In summary, the operations performed in the hippocampal circuit during SWRs seem to be relevant for memory formation and could also be implicated in several cognitive functions other than memory. The fast, temporally structured sequences of cellular activity generated during SWRs could be involved in the transfer of information from hippocampus to neocor-

tex, the planning of future behavioral sequences, and finding new solutions (paths) based on previous experience.

1.3 Anatomy of the hippocampal formation

A cross section of the hippocampal formation typically exhibits two interlocking c-shaped profiles in which three histologically different areas can be distinguished; the dentate gyrus (DG), the Cornu-amonis (CA) and Subiculum (Fig. 1.2*A*). These areas exhibit a three-layered appearance that distinguishes the hippocampal formation from its adjacent six-layered neocortex (Fig. 1.2*B*). A prominent cell layer mostly contains the somata of principal cells and of some interneurons. In the DG this layer is referred to as granule layer, whereas in the CA region and the Subiculum it is called *stratum pyramidale*. Located deeper with respect to the cellular layer is the *stratum oriens*, which contains a mixture of both afferent and efferent fibers, and interneuron somata. In the DG this areas is referred to as hilus. The most superficial layer is the *stratum moleculare*, which in the CA region is further subdivided into three regions: The most-superficial *stratum lacunosum-moleculare*, which comprises the tufts of apical dendrites; the *stratum radiatum*, which houses the apical dendrites of those neurons located in the *stratum pyramidale*; and the *stratum lucidum*, which is missing in the CA1 area (Fig. 1.2*B*, orange). These subareas are differentially targeted by different interneuron types and afferents from intra and extrahippocampal origin.

The adjacent entorhinal cortex (EC) (Fig. 1.2*B*, light and dark green) constitutes the main gateway between the hippocampal formation and neocortical areas. The connectivity between the EC and the hippocampus suggests a unidirectional flow of information through the hippocampal formation (Amaral and Witter, 1989). Superficial layers II and III of EC project to structures in the hippocampus proper which, in turn, project back to the deep layers of the EC via CA1 and Subiculum (Fig. 1.2*C*). The projections from layer II, which target CA3 directly or via DG, conform the perforant pathway (PP). CA3, in turn, projects to cells within the same area via recurrent collaterals (RC) and to CA1 via Schaffer collaterals (SC). The projections from layer III of the EC, which project directly to CA1, conform the temporoamonic pathway (TA). Thus, the CA1 area constitutes the primary output of the hippocampal formation, where all information converges before being relayed back to the EC. In the following I will focus on the details of the cellular composition and connectivity of the CA1 area.

1.4 The CA1 microcircuit and its afferents

The CA1 area is attractive to study SWRs for several reasons. First, CA1 is the main output of the hippocampal formation, where input from both cortical, intrahippocampal and thalamic input converge. Second, it can generate SWRs when isolated from the rest of the brain (Maier et al., 2003) and therefore contains the minimum circuitry to generate the phenomenon. Third, the CA1 area is also attractive from a modeling perspective due to the large availability of data regarding cell types and network connectivity (Bezaire and Soltesz, 2013).

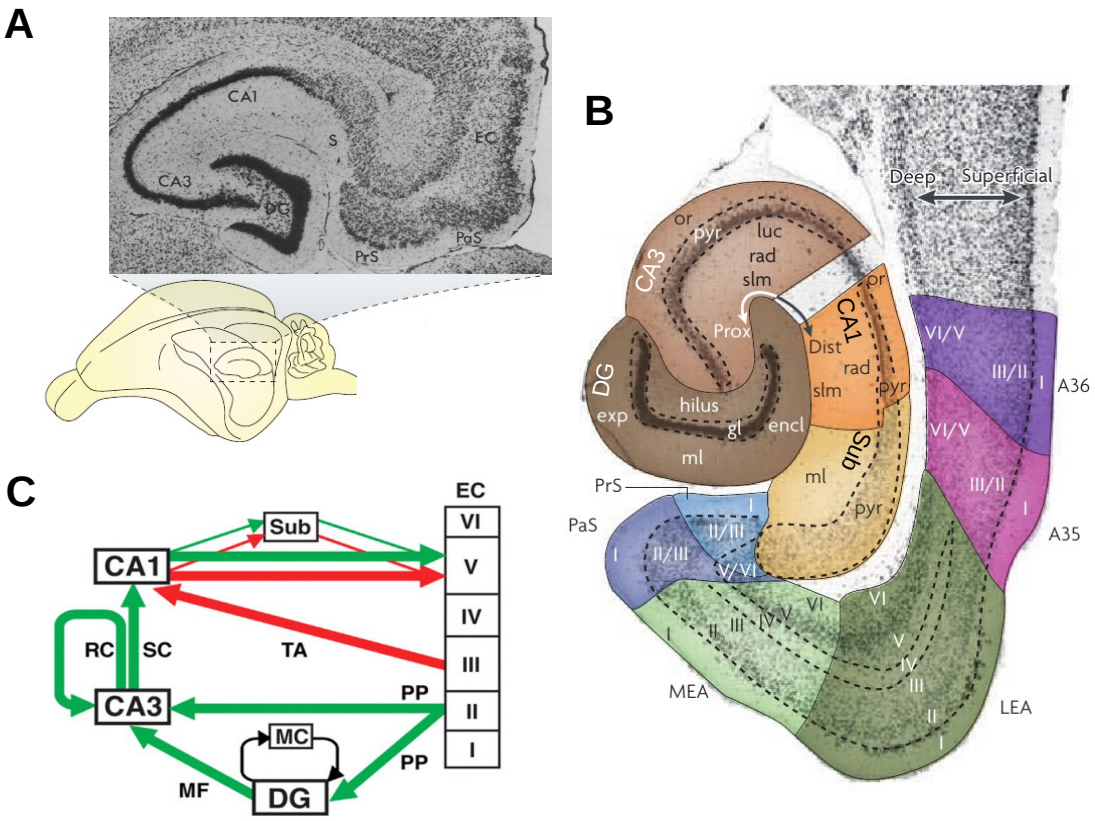

Fig. 1.2: Anatomy of the hippocampal formation. ***A***, Transverse slice of the rat hippocampus where cornu ammonis (CA), dentate gyrus (DG), subiculum (S), presubiculum (PrS), parasubiculum (PaS) and entorhinal cortex (EC) can be distinguished (Amaral and Witter, 1989; reproduced with permission from Elsevier). ***B***, Horizontal cross section (as in *A*) in which the cortical layers and three-dimensional axes are marked. CA, cornu ammonis; dist, distal; encl, enclosed blade of the DG; exp, exposed blade of the DG; gl, granule cell layer; luc, stratum lucidum; ml, molecular layer; or, stratum oriens; prox, proximal; pyr, pyramidal cell layer; rad, stratum radiatum; slm, stratum lacunosum-moleculare. The EC has a lateral (LEA; dark green) and a medial (MEA; light green) aspect. The perirhinal cortex consists of Brodmann areas A35 (pink) and A36 (purple). The Roman numerals indicate cortical layers. (Van Strien et al., 2009; reproduced with permission from Nature Publishing Group). ***C***, Excitatory pathways in the hippocampal formation and EC. Green and red arrows designate the trisynaptic pathway and temporoamonic (TA) pathways, respectively. Sub, subiculum; MC, mossy cells; PP, perforant pathway (Nakashiba et al., 2008; reproduced with permission from AAAS).

1.4.1 Excitatory afferents

Excitatory fibers originating from different brain areas provide afferents to CA1 pyramidal cells and interneurons in a layer-specific manner. Schaffer collaterals from CA3 provide input to structures in the *str. radiatum* and can also project to *str. oriens*. Entorhinal fibers stemming from layer III terminate in the *str. lacunosum-moleculare* and inervate both principal cells and interneurons at their apical tufts (Kiss et al., 1996; Naber et al., 2001;

Takács et al., 2012). The nucleus reuniens of the thalamus projects to the *str. lacunosum-moleculare* where it overlaps with fibers from the entorhinal cortex on both pyramidal cells and interneurons (Wouterlood et al., 1990).

1.4.2 Interneuron types

The CA1 network contains a variety of interneuron types that can be classified based on several features that are relevant for their function. Anatomical criteria consider the structure of their dendritic and axonic arborizations and the location of the cell body (Freund and Buzsáki, 1996). These features are important because the position, extension and orientation of their dendritic and axonic structures can determine the type of afferents they are exposed to, and the structures in their postsynaptic targets they preferentialy innervate, respectively. Interneurons can also be classified according to the molecules they express. For example, neuropeptides such as somatostatin (SOM) and cholecystokinin (CKK), and calcium binding proteins such as parvalbumin (PV) and calbindin (CB) (Freund and Buzsáki, 1996). A third criterion considers dynamical properties such as their spiking behavior (e.g. fast spiking versus regular spiking).

Oriens lacunosum-moleculare (O–LM) cells. These interneurons exhibit a peculiar anatomical arrangement with respect to their somatic location and axonal projection area (Sik et al., 1995; Maccaferri, 2005). Their somata are located in the *str. oriens*, where they give rise to an horizontally orientated dendritic tree that covers the *str. oriens* and part of the *alveus*. As a consequence, the excitatory input onto O-LM cells is primarily local (Blasco-Ibáñez and Freund, 1995), which place them in a privileged position to sample the output of the pyramidal cell network in CA1. The axonal ramifications of O–LM cells project to distal apical dendrites of CA1 pyramidal cells, overlaping with the termination area of fibers from thalamus and entorhinal cortex (Wouterlood et al., 1990; Colbert and Levy, 1992; Empson and Heinemann, 1995), suggesting they can modulate input from these brain regions.

Bistratified cells. The somata of these cells are located in *str. pyramidale* (Buhl et al., 1996; Halasy et al., 1996) where they give rise to a radially oriented dendritic tree that is innervated by SC fibers. Their axons extend to the *str. oriens* and *radiatum*, where they target basal and apical dendrites of pyramids, in alignement with the SC input (Halasy et al., 1996; Maccaferri et al., 2000).

Axoaxonic cells. These cells target exclusively the axon initial segment of pyramidal cells (Somogyi et al., 1983) and have been shown to effectively control its excitability (Dugladze et al., 2012). Their somata can be located in the *str. pyramidale* or *str. oriens* (Buhl et al., 1994). Those located in the *str. pyramidale* exhibit a radial dendritic tree that extends to all layers (Buhl et al., 1994; Pawelzik et al., 2002). Those located in the *str. oriens*, on the other hand, give rise to an horizontal dendritic tree that extends widely along the *str. oriens* (Ganter et al., 2004).

Basket cells (BC). Their cell bodies are typically located in the pyramidal cell layer or in its close vicinity (McBain et al., 1994). Their dendritic trees cover the *str. radiatum* and *str. lacunosum-moleculare* on the apical side, and the *str. oriens* and alveus on the basal

side. The axonal arbors of these cells concentrate on the *str. pyramidale*, extending to the proximal segments of the *str. oriens* and *str. radiatum*, where they preferentially innervate the soma and proximal dendrites of pyramidal cells (Freund and Buzsáki, 1996). These cells can be further classified between those expressing parvalbumin (PV^+) and those expressing CCK (CCK^+). These BC subtypes tend to exhibit different electrophysiological features. PV^+BC are typically fast-spiking cells (Pawelzik et al., 2002), which can reach frequencies above 100 Hz and show no spiking rate adaptation. CCK^+BC, on the other hand, tend to be regular spikers (Freund, 2003). PV^+BC receive input from both SC and local collaterals from CA1 and therefore they can provide both feedforward and feedback inhibition.

1.4.3 Intralaminar connectivity

There is evidence of functional differentiation along the radial axis (deep/superficial) of CA1 (Slomianka et al., 2011). Pyramidal cells located in the deep (closer to the *oriens*) and superficial (closer to the *radiatum*) substrata of CA1 exhibit different physiological features and, most remarkably, different connectivities with BCs (Lee et al., 2014). The CB^+ superficial pyramids provide three times more projections to PV^+BCs than their CB^- counterparts in the deep layers. Furthermore, superficial pyramids receive much weaker ($\sim$3 fold) PV^+BCs mediated inhibition than superficial pyramids. In contrast to deep pyramids, their superficial counterparts are preferentially innervated by CCK^+BC (Valero et al., 2015).

1.5 Mechanisms of sharp-wave ripple generation

In the previous section, I have provided a rough sketch of the CA1 microcircuit and its afferents. The next step is to understand how the components of such microcircuit interact during the time course of a SWR event. In this section, I will first focus on those elements generating the local field potential; the 'sound' of the CA1 'heart' during SWRs. Then, I will describe the activation patterns of different interneuron types involved in the phenomenon. Finally, I will focus on the putative interactions underlying the entrainment of the cellular activity to the ripple oscillation.

1.5.1 Dissecting the local field potential

In the CA1 area, a SWR complex consists of two localized, co-ocurring events in the local field potential (Fig. 1.3). The sharp wave (SW) appears in the *str. radiatum* as a short-lived (40-100 ms) large negative deflection that often appears associated with a fast (140–220 Hz) oscillation in the *str. pyramidale*, the 'ripple' (O'Keefe, 1976; Buzsáki et al., 1983). Such an LFP profile is generated by specific extrasomatic and perisomatic currents in CA1 pyramidal cells, respectively. The current sink-source distribution of the SW typically shows a large sink in the mid-apical dendritic compartment of CA1 pyramids with the corresponding return current in the cell body layers. Such a strong sink in the *radiatum* points at excitatory currents in the apical dendrites of CA1 induced by Schaffer collateral activity (Buzsáki et al., 1983; Sullivan et al., 2011). This suggests that the SW reflects the transient activation of CA3 pyramidal cells. In support, electrically induced discharges of CA3 pyramids generate a similar current distribution, and long-term potentiation of the Schaffer collateral-CA1 synapses increases the amplitude of SWRs (Buzsáki, 1984).

The ripple, on the other hand, reflects the coordinated oscillatory activity of perisomatic targeting interneurons (Ylinen et al., 1995; Schlingloff et al., 2014). The currents

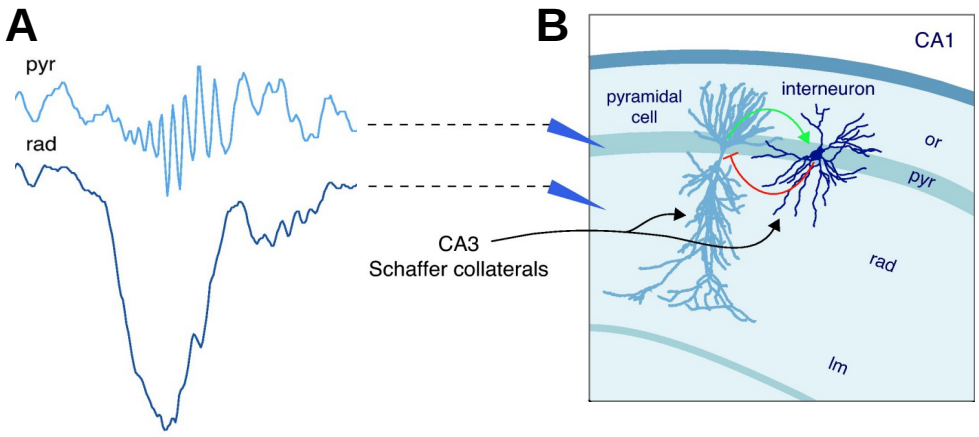

Fig. 1.3: Depth profile of sharp wave-ripples in CA1. ***A***, Simultaneous with the sharp wave recorded in *stratum radiatum* (rad), a high frequency (∼200 Hz) ripple oscillation is recorded in *stratum pyramidale* (pyr). ***B***, Sharp waves in *stratum radiatum* reflect massive excitation of CA1 neurons by CA3 pyramidal cells via the Schaffer collaterals. The concomitant synchronization of the interneuron network at ∼200 Hz generates a ripple in the *stratum pyramidale* (or: *stratum oriens*, lm: *stratum lacunosum moleculare*) (Girardeau et al., 2009; reproduced with permission from Elsevier).

contributed by principal cells in the perisomatic area are almost exclusively mediated by GABAergic synapses (Megías et al., 2001; Papp et al., 2001). When these synapses are synchronously driven across many cells, they generate a train of outward currents that build up constructively in the extracellular field, giving rise to a prominent ripple in the *str. pyramidale*.

1.5.2 Cellular activation during sharp-wave ripples

During a single SWR episode, nearly 10% of the hippocampal neuronal population is activated (Csicsvari et al., 2000). Pyramidal neurons in CA1 exhibit the strongest gain (∼9–fold) in firing rate with respect to non-SWR periods. These cells tend to fire at the trough of the ripple cycle, at a typical rate of ∼10 spikes/s (Csicsvari et al., 2000). Interneurons located in the *str. pyramidale* and proximal substrata, on the other hand, exhibit a 4–fold increase in discharge frequency during SWR. The absolute firing rates of interneurons, however, are considerably higher in comparison to those of principal neurons (∼100 spikes/s) (Csicsvari et al., 1999b, 2000).

The two interneuron types that exhibit the largest increase of activity during SWRs are the PV^+BCs and the bistratified interneurons (Klausberger et al., 2003). Both cell types fire phase-locked to the extracellular ripple, preferentially during the ascending phase of the ripple cycle. In stark contrast to their PV^+ counterparts, CCK^+BCs do not significantly alter their firing rates during SWRs (Klausberger et al., 2005). Such low activity may contribute to disinhibition of both pyramidal cells and PV^+BC, which they innervate (Karson et al., 2009; Buzsáki, 2015). Therefore, PV^+BCs constitute the most likely drivers of fast perisomatic inhibitory activity onto principal cells during SWRs.

Axo-axonic cells, on the other hand, increase their firing probability at the beginning of the SWR, but remain silent at the maximum amplitude and after the ripple episode (Klausberger et al., 2003; Forro et al., 2015). Such a pattern of activity might facilitate the

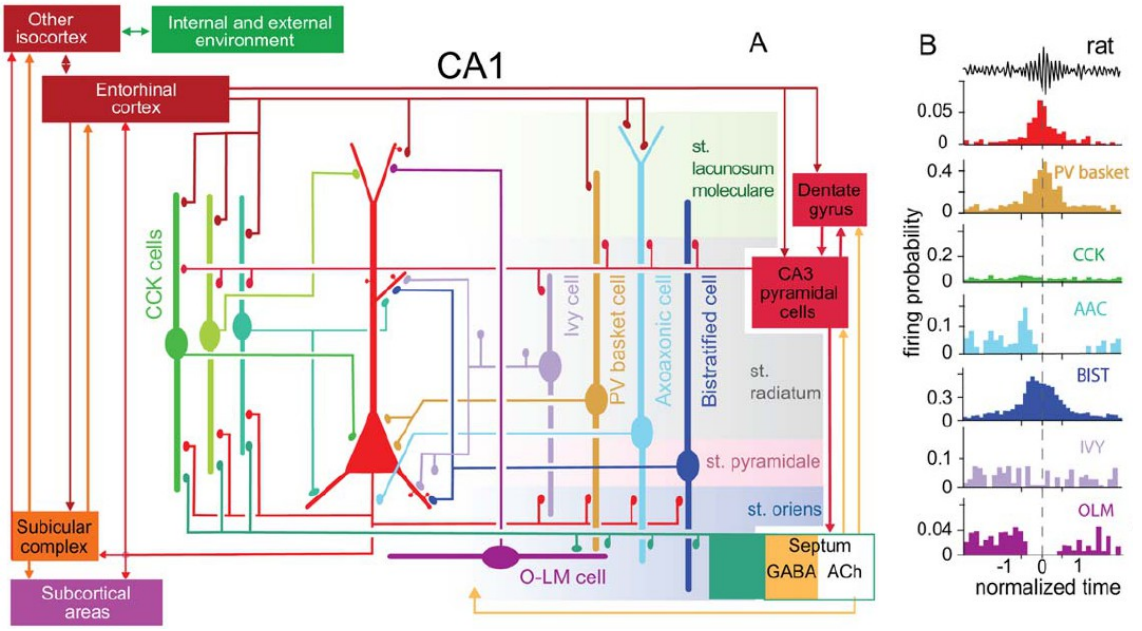

Fig. 1.4: SPW-R-related firing patterns of interneurons. ***A***, Schematic of the main synaptic connections of pyramidal cells (red, middle), three types of CCK-expressing cells (basket cell, perforant path-associated cell, Schaffer collateral-associated cell), ivy cells and PV-expressing basket, axo-axonic, bistratified and O-LM interneurons. Connections among interneurons are not shown. ***B***, Firing probability histograms; averages from several cells of the same type recorded in anaesthetized rats. The start, maximum amplitude and end of the normalized sharp-wave episodes are marked as -1, 0 and 1, respectively. Note different scales for the y-axis (Somogyi et al., 2014).

information transmission from pyramids to their downstream targets during the mid to late phase of the SWR event.

1.5.3 Ripple pacemakers

As we have seen in the previous section, during SWR, both principal cells and interneurons display a highly organized firing pattern. A fundamental question at this point concerns the mechanism responsible for the entrainment of the firing of both interneurons and principal cells to the ripple oscillation. Existing hypotheses differ in where and how the primary oscillation is generated.

Excitation-first models

The two existing models belonging to this class propose that the oscillation is generated in pyramidal cells and then transferred to the interneurons via local principal-to-interneuron connections, but they differ in the mechanism coordinating the oscillation.

In the first of these two models, the primary pacemaker originates in principal cell axons (Traub and Bibbig, 2000). It is hypothesized that the smaller branches of axonal ramifications are connected by gap junctions. Models show that such an electrically coupled

network can generate oscillatory activity in the ripple band if certain conditions in the connectivity and coupling strength are met (Traub et al., 1999; Traub and Bibbig, 2000). In this model, the frequency of the oscillation is determined by the topological structure of the network, and the spike-to-spike latency as spikes propagate and reproduce within the axon plexus.

The second model of this class relies exclusively on local synaptic interactions between principal cells (Memmesheimer, 2010; Jahnke et al., 2015). It is hypothesized that the ripple corresponds to a transient propagation of synchronous activity in the pyramidal cell network, which is mediated by supralinear synaptic integration and dendritic spikes in pyramidal cells. Such synchrony propagation is paced by the stereotypical latency ($\sim$ 5 ms) of the spiking response of principal cells to the arrival of synchronous inputs (Ariav et al., 2003).

Inhibition-first models

A third model proposes that the primary pacemaker is provided by the interneurons themselves which, in turn, would pace the firing of principal cells (Ylinen et al., 1995; Csicsvari et al., 1999b). In this scenario, a recurrent interneuron network of fast spiking basket cells is driven by an input barrage delivered by CA3 via the Schaffer collaterals. Upon stimulation, this recurrent network oscillates at ripple frequency, providing strong perisomatic inhibition and pacing to a population of principal cells.

Several modeling studies have shown that reciprocally connected interneuron networks can self-entrain and generate oscillations when enough excitatory drive is provided to the interneurons (Wang and Buzsáki, 1996; Bartos et al., 2002; Brunel and Wang, 2003; Maex and Schutter, 2003). An interesting aspect of these models is that the determinants of the network frequency depend on the oscillatory state of the network. Under fully synchronized oscillations, the frequency is determined by the level of excitatory drive and properties of the GABAergic synaptic transmission, such as the latency and the rise and decay time constants of the postsynaptic currents (Traub et al., 1996; Wang and Buzsáki, 1996). Under sparsely synchronized oscillations, on the other hand, the frequency is mostly determined by the latency and the rise time of the inhibitory postsynaptic currents, and it is therefore largely independent of changes in the excitatory drive or decay time constant of GABAergic transmission. These oscillatory regimes will be discussed in detail in Chapter 2.

1.6 Aim of this work

The main focus of this thesis is on the mechanisms governing the frequency of interneuronal network oscillations in the context of SWRs. In particular, I address some features of the ripple frequency that remain currently unexplained, namely, its intra-ripple dynamics, its variability across episodes, and its resistance to GABA modulators. To do this, I resort to an *in silico* model of the PV^+BC network in CA1, and an *in vitro* model of SWRs. Additionally, I investigate the recruitment of O-LM interneurons during SWRs *in vitro*.

1.6.1 Intra-ripple frequency accommodation

An interesting peculiarity of ripple oscillations is that they exhibit a higher frequency during the first half of the episode, followed by a monotonic deceleration during the second half. Such a time course of the instantaneous frequency during single episodes has been widely reported in the literature (Ponomarenko et al., 2004; Nguyen et al., 2009; Stark et al., 2014;

Hulse et al., 2016) and has been termed 'intra-ripple frequency accomodation' (IFA). The mechanisms generating such a phenomenon have not been studied so far. In Chapters 2 and 3, I resort to an *in silico* model of the PV^+BC network to provide insights on the mechanisms behind IFA. In Chapter 4, I test the predictions of the *in silico* model in an *in vitro* preparation.

1.6.2 Frequency variability

In vivo, SWRs exhibit a large variability in ripple frequency. Larger-amplitude events appear associated with frequencies in the ripple range (140–200 Hz) whereas lower-amplitude events tend to contain oscillations in the fast gamma (90–140 Hz) range (Csicsvari et al., 1999a; Sullivan et al., 2011; Stark et al., 2014). In Chapter 3, I hypothesize how the differential connectivity described in section 1.4.3 may play a role in setting the frequency of different events.

1.6.3 Frequency resistance to GABA modulators

Experiments *in vitro* have shown that ripple frequency is insensitive to drugs that induce a large increase in the amplitude and/or the decay time constant of fast GABAergic transmission (Papatheodoropoulos et al., 2007; Koniaris et al., 2011; Viereckel et al., 2013). Such frequency-resistance to inhibitory modulation has been interpreted as evidence against an interneuronal pacemaker for ripple oscillations (Viereckel et al., 2013). In Chapter 5, I test the validity of such argument by simulating the effects of GABA modulators on an interneuronal network model under different driving conditions.

1.6.4 Recruitment of O-LM interneurons during hippocampal ripples

A recent study *in vivo* has demonstrated activation of O-LM cells during SWRs. In Chapter 6, I characterize the excitatory currents received by O-LM cells during SWRs *in vitro* and investigate the factors that determine their recruitment.

2 Persistent oscillations

According to the inhibition-first model, ripple oscillations are coordinated by a putative network of recurrently connected basket cells. Upon stimulation, such a network generates waves of inhibitory activity that can entrain the firing of pyramidal cells. Here I analyze the response of a model of the CA1 basket cell network to different levels of persistent excitatory activity. At low levels of excitatory drive, the network exhibits oscillations that emerge from units that fire irregularly. In such a 'high noise' state, the network frequency is insensitive to the level of excitatory drive. With increasing excitation, the network transits towards a fully synchronized regime, which is characterized by units that fire regularly at rates close to the network frequency. In such a 'low noise' state, the network frequency becomes entangled to the firing rate of units, and both variables increase monotonically with input drive. Finally, I assess the robustness of the ripple frequency generated by the interneuronal network when driven by ripple-modulated excitatory input, as in excitation-first models. High modulation depths facilitate the excitatory entrainment of the interneuron network whereas a high mean level of excitation favors the dominance of the interneuronal network. In conclusion, the putative interneuronal network pacemaker can be entrained by a co-existing excitatory pacemaker only if the total excitatory input to the interneurons is strongly modulated with a low mean.

2.1 Oscillations in inhibitory networks

The main hypothesis of the inhibition-first model is that ripple oscillations are coordinated by a network of recurrently connected interneurons. Upon stimulation, such a network is capable of self-organizing its collective activity into oscillations, which can further entrain the firing of pyramidal cells. How do interneuronal networks generate oscillatory activity?

2.1.1 General mechanism of inhibitory self-entrainment

To illustrate the general principle underlying oscillations in inhibitory networks, I will resort to an analogy involving a population of fireflies (Fig. 2.1). Such insects can produce light autonomously, and large groups of them can collectively organize complex patterns of flashing (Smith, 1935; Buck, 1988). Here I will resort to a population composed by an hypothetical type of firefly that expresses a very simple behavioral pattern: they glow in response to a dark environment and they switch off in the presence of light or, more precisely, when the brightness of the environment exceeds a threshold. In addition, let us assume that these fireflies cannot respond instantaneously; the switching of behavior (on/off) occurs with some latency after the environmental brightness has crossed the threshold. If we now assemble a large population of such simple units in a dark environment (Fig. 2.1, bottom), every individual will start to glow, and the population will produce a considerable amount of light. If the population is large enough, the amount of collectively generated light could increase the brightness of the environment to the point where the response threshold is reached (Fig. 2.1, top). After a brief behavioral latency, the whole population will switch off and darkness will

ensue. Once again, in response to the dark environment, the whole population will start to glow and a new cycle will begin. The collective luminous activity of the population oscillates.

From this simple analogy one can already draw two important conclusions: First, a feedback coupling between the collective activity and the individual activity is required: The individual activity constitutes the population activity which, in turn, inhibits and therefore constrains the individual activity. Such coupling depends on several factors such as the size of the population, the intensity of the light emitted by single units, their sensitivity, etc. Second, for an oscillation to ensue, a delay is required. Without the behavioral latency, the population would be in a singular state that could be interpreted as an oscillation of infinite frequency (i.e., the individuals would be active and inactive at the same time).

The same principle underlies oscillations in a population of recurrently connected inhibitory neurons (Wang and Buzsáki, 1996; Brunel, 2000; Maex and Schutter, 2003). In such a network, each unit receives inhibitory input from a subpopulation belonging to the same network. When interneurons are tonically excited, they fire together and each unit experiences a sample of this collective activity as inhibitory input. The units then remain silent for the time this transient inhibition endures. When enough excitatory input is integrated and the firing threshold is reached, another burst of activity emerges and a new cycle begins.

2.1.2 Oscillatory regimes: from full to sparse synchrony

In the thought experiment described above, I implicitly assumed an homogeneous population of units; the fireflies shared the same sensitivity, responsiveness, etc. Moreover, units were ideally coupled to the population activity; the fireflies could see the light produced by all their peers. This means that all units receive exactly the same input and respond exactly in the same way. As a consequence, all units fire perfectly synchronized and the population behaves exactly like one big single unit (e.g., Fig. 2.2*C*). This network behavior corresponds to an idealized case of the so called 'fully synchronized' oscillations (Brunel and Hakim, 2008). Such an oscillatory regime has been observed in interneuronal networks when interneurons are driven by tonic currents that are homogeneously distributed across the population (Wang and Buzsáki 1996; Traub et al. 1996; see also Fig. 5.4*B*).

Things get more interesting when we add some stochasticity to the fireflies depicted in Figure 2.1. Suppose now that, in response to a dark environment, the units no longer respond deterministically but they turn on with a 50% chance. If we assemble a large population in a dark environment, roughly 50% of the population will glow. Now suppose that that the light produced by that fraction of the population is enough to bring the units above their thresholds and switch them off. Again, the population activity will oscillate but in a more 'interesting' fashion. At any given cycle, only a random subpopulation of units is active. If we look at the behavior of single units we would see that they display an irregular pattern of activity; they skip cycles randomly. Thus, the population activity emerges from units that fire irregularly but consistently to the collective rhythm. This network behavior closely resembles the so called 'sparsely synchronized' oscillations observed in interneuronal networks (Brunel and Wang, 2003; Maex and Schutter, 2003). Such a regime emerges when interneurons receive stochastic input that is uncorrelated across cells (e.g., Fig. 2.2*A*).

In summary, fully synchronized oscillations tend to emerge in conditions of 'low noise' whereas sparsely synchronized oscillations tend to emerge in conditions of 'high noise'.

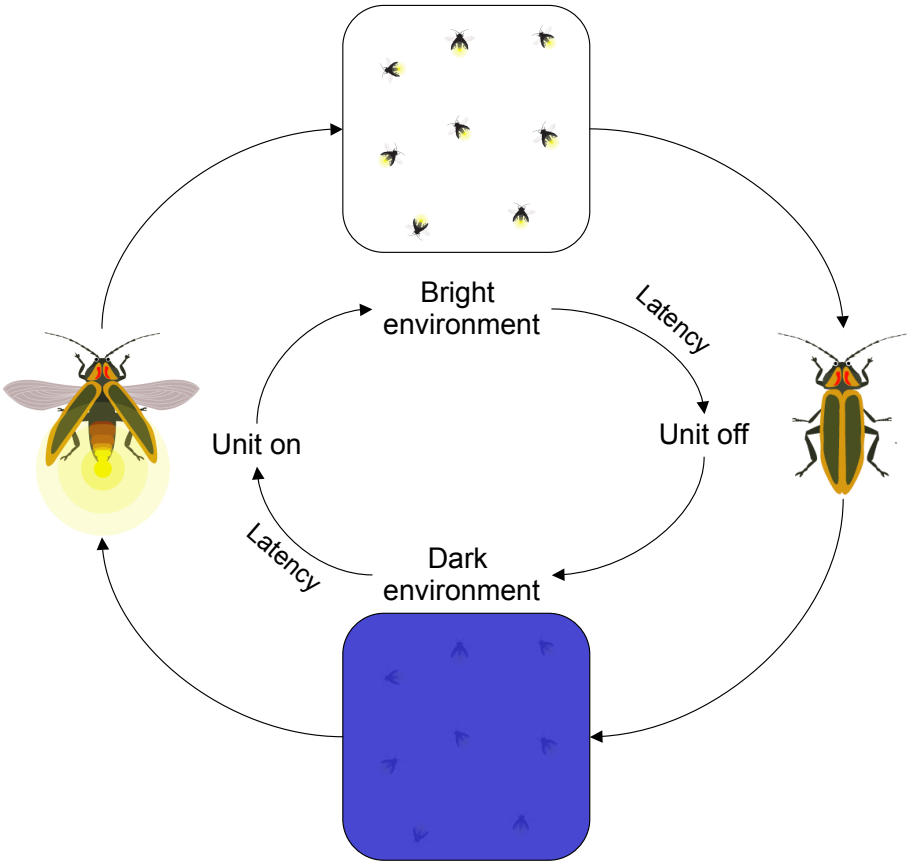

Fig. 2.1: Oscillations in a population of fireflies. Every unit expresses a simple response to the light conditions of the environment: glow in darkness (left) and switch off in the presence of light (right). The switch of behavior occurs with some latency. When a large population is assembled in a dark environment (blue box at bottom), the population generates enough light to produce a bright environment (top). In response to the bright environment, the population turns off and a new cycle begins (illustrations of fireflies were kindly provided by Brunel Wester).

2.2 Oscillations in a network of basket cells

In the inhibition-first model, ripple oscillations are coordinated by a network of recurrently connected interneurons, presumably parvalbumin-immunoreactive basket cells (PV^+BC) (Klausberger et al., 2003; Schlingloff et al., 2014; Katona et al., 2014). In support, *in vitro* studies showed that oscillations in the ripple band can be generated by optogenetically driving PV^+ interneurons in the absence of excitatory synaptic transmission (Schlingloff et al., 2014).

Here, I introduce a model of the putative PV^+BC network in CA1 and characterize its response to different levels of excitatory drive, both unmodulated (Figs. 2.2 and 2.3) and ripple-modulated (Fig. 2.4). The model consists of a population of 200 interneurons that are randomly interconnected via fast GABAergic synapses with a connection probability of 20%. Excitatory input is delivered by a driving population of 8,200 pyramids that are randomly connected to the interneuron network via fast AMPA-type synapses with a connection probability of 9.5%. Such connectivity implies that each interneuron receives ∼40 GABAergic and ∼780 AMPA-type synapses; for a motivation of this particular choice of numbers, see Methods at the end of the chapter.

2.2.1 Driving strength and oscillatory regime

I delivered persistent stimulation to the interneuron network by allowing each of the 8,200 pyramids in the driving population to fire randomly at a constant rate that was varied between 1.3 and 19.3 spikes/s. Because each interneuron has ∼780 AMPA-type synapses, the total input rates varied between 1,000 and 15,000 spikes/s. In the following, I show that in the steady-state response of the network, low and high input rates favor the emergence of sparsely and fully synchronized oscillations, respectively. Figure 2.2*A* shows the response of the network when a total input rate of 3,000 spikes/s was applied. A prominent and stable high-frequency oscillation was apparent in the population activity throughout the stimulation (Fig. 2.2*A*, top). Interestingly, oscillations in the population activity emerged from units that fired irregularly, as indicated by the rastergram (Fig. 2.2*A*, middle): only a random subset of units was recruited in any given cycle. The membrane potential of a typical interneuron in the network showed subthreshold oscillations that reflected the oscillatory population activity (Fig. 2.2*A*, bottom). Such oscillations of the membrane potential constrain the timing of the spiking response of interneurons by providing windows of opportunity at which they are more likely to fire. Random fluctuations, here due to Poissonian excitatory activity, occasionally bring the membrane potential above threshold. As a result, units skip cycles randomly, giving rise to a firing pattern that is irregular but in phase with the population activity. The prominence and coherence of network oscillations were further revealed in the spectrum of the population activity by a peak at ∼ 187 Hz (Fig. 2.2*B*, top, gray trace). In contrast, the distribution of firing rates in the population showed that units fired at a broad range of rates, and rates were lower than the frequency of the oscillatory population activity (Fig. 2.2*B*, bottom, gray trace; see also Bähner et al., 2011).

The behavior of the interneuron network at such a low input rate was consistent with the so called 'sparsely synchronized oscillations' (Brunel and Hakim, 2008). Such a regime emerges in conditions of high noise and is characterized by units that fire irregularly at rates lower than the frequency of the oscillations in the population activity (Brunel, 2000; Brunel and Wang, 2003; Maex and Schutter, 2003). In this regime, the frequency is determined by the delay of the recurrent interactions (transmission latency and rise time of IPSCs) and it

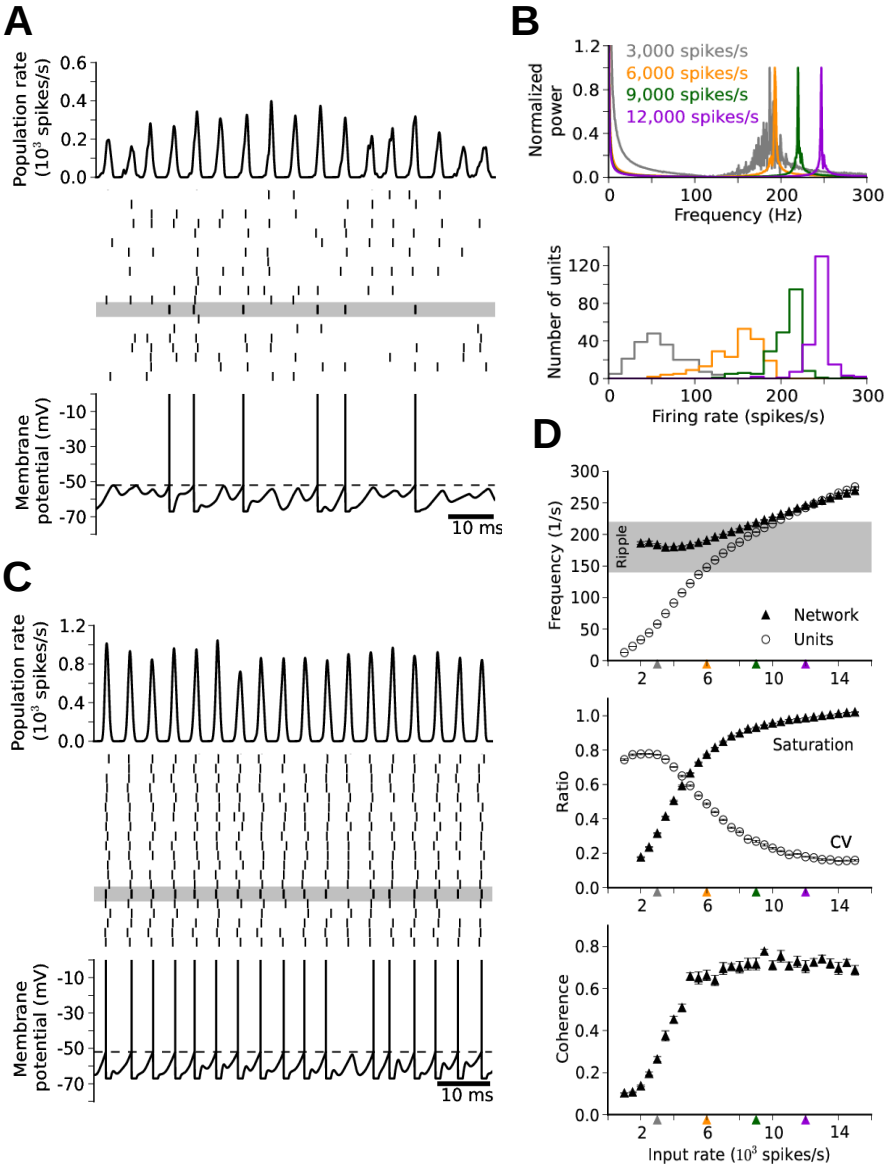

Fig. 2.2: Oscillations in a model of the CA1 basket cell network. ***A***, Network activity at an input rate of 3,000 spikes/s. Oscillations in the population rate (top) emerge from units that fire irregularly (middle: spike raster plot for 20 out of 200 units). Bottom: Membrane potential of a unit (spike times marked by horizontal gray bar in middle panel). ***B***, Power spectral density of population activity (top) and firing-rate histogram of units (bottom) at four levels of input rates (gray traces correspond to activity depicted in *A*). ***C***, Network activity at an input rate of 9,000 spikes/s (green traces in *B*). Oscillations in the population rate (top) emerge from units that fire regularly and rarely skip cycles of the population activity (middle). Bottom: Membrane potential of a unit (spike times marked by gray bar in middle panel). ***D***, Steady-state network response as a function of input strength (input levels depicted in *B* are indicated by colored triangles in the horizontal axis). Top: Network frequency (triangles) and mean firing rate of units (circles). The gray area demarcates the ripple band (140–220 Hz). Middle: The saturation (triangles) is the average fraction of units recruited in one cycle. Irregularity of firing is described by the average coefficient of variation (CV, circles) of the interspike interval of units. Bottom: Coherence of network oscillations.

is therefore largely independent of the level of excitation provided (Brunel and Wang, 2003).

Consistent with the sparsely synchronized regime, a doubling in the input strength from 3,000 spikes/s to 6,000 spikes/s shifted the firing-rate distribution towards higher values but the network frequency increased only by 3% (Fig. 2.2*B*, gray and orange traces). However, when the input strength was increased beyond 6,000 spikes/s, the network frequency markedly increased with input strength (Fig. 2.2*B*, top). This change of behavior was accompanied by an increasingly larger fraction of units firing at rates close to the network frequency (Fig. 2.2*B*, bottom). Such a change in the network response with increasing input rate suggested a change in the oscillatory regime.

Figure 2.2*C* shows the response of the network when a total input rate of 9,000 spikes/s was applied. A prominent high-frequency oscillation was apparent in the population activity (Fig. 2.2*C*, top). Units fired regularly and they rarely skipped cycles (Fig. 2.2*C*, middle and bottom): almost the entire population was recruited in any given cycle. Accordingly, units fired at mean rates close to the peak frequency of the oscillatory population activity (Fig. 2.2*B*, green traces), in stark contrast to the situation depicted in Figure 2.2*A*.

The behavior of the interneuron network at such a high input rate was consistent with the so called 'fully synchronized oscillations' (Brunel and Hakim, 2008). This mode of oscillation, characterized by units that fire regularly at rates close to the population frequency, was previously observed in interneuron network models expressing gamma oscillations (Wang and Buzsáki, 1996; Traub et al., 1996; Bartos et al., 2002).

Figure 2.2*D* summarizes the behavior of the network for the entire range of input rates tested. The network required a minimum input rate of $\sim$ 2,000 spikes/s for oscillations in the population activity to arise. At this input rate, the network frequency was $\sim$ 186 Hz. At input rates between $\sim$ 2,000 and $\sim$ 6,000 spikes/s, the network activity exhibited the typical traits of sparsely synchronized oscillations: The network frequency was stable but the firing rates of units increased monotonically with input strength, remaining below the network frequency (Fig. 2.2*D*, top). The irregularity of unit firing was apparent in the high ($\gtrsim 0.5$) coefficient of variation (CV) of interspike intervals (Fig. 2.2*D*, middle), which indicates a high-noise state of the network. As input strength increased towards and beyond 6,000 spikes/s, units skipped less and less cycles, their activity became gradually more regular (CV decreased), and the network saturation, which is defined as the fraction of the population recruited in any given cycle, further increased (Fig. 2.2*D*, middle). For an input rate $\gtrsim$ $9,000$ spikes/s, the network entered a state that resembled a fully synchronized regime. In this low-noise state, units expressed a low ($\lesssim 0.3$) CV (Fig. 2.2*D*, middle), the network frequency and the firing rate were similar, and both increased monotonically with input rate (Fig. 2.2*D*, top).

The coherence of network oscillations also marked the regime transition: it increased rapidly with input rate in the region corresponding to the high-noise state, and saturated where the low noise regime expressed (Fig. 2.2*D*, bottom).

In summary, the amount of excitatory drive can modulate the oscillatory state of a recurrent interneuron network. At low input rates, the network generates sparsely synchronized oscillations. Consistent with previous models expressing this type of oscillations, the network frequency is relatively insensitive to changes in input rate (Brunel and Wang, 2003; Maex and Schutter, 2003). With increasing input rates, the network frequency becomes gradually more sensitive to excitation as it transits toward a fully synchronized regime. In line with previous models exhibiting this type of oscillations, the network frequency increases monotonically with increasing excitatory drive (Wang and Buzsáki, 1996; Traub et al., 1996).

2.2.2 Mechanisms underlying regime transition

What are the mechanisms governing the network behavior at different input rates? To address this question, I studied the time course of membrane potentials across units during the oscillatory population activity. Figure 2.3*A* shows four cycles of the interneuron population activity (top) and the underlying distribution of membrane potentials (bottom) when a low input rate of 3,000 spikes/s was applied. The membrane potentials were always highly variable across cells due to the uncorrelated noisy input. The mean potential oscillated sinusoidally below the firing threshold. Spikes were generated during the ascending phases and around the peaks of this oscillating distribution. The process giving rise to the oscillatory population activity can be explained as follows: consider a trough of the oscillatory distribution shown in Figure 2.3*A* as the starting point of a cycle. At that point, all the units are below threshold and therefore the population is silent. The excitatory input charges the membranes of the interneurons, moving the distribution of membrane potentials toward more depolarized values (Fig. 2.3*A*, bottom). Eventually, the upper tail of the distribution reaches the threshold (Fig. 2.3*A*, horizontal dashed line) and the corresponding subset of units fire. Conduction and synaptic delays introduced by the recurrent connections allow the spiking activity to further build up before being fed back to the network in the form of inhibitory currents. The inhibitory currents induced by the population activity shift the distribution of membrane potentials to more hyperpolarized values, and thereby, the spiking activity is reduced and eventually silenced. At this phase, all the negative charge 'contained' in one cycle of the population activity has been delivered back to the network, and the membrane-potential distribution reaches a minimum. As inhibitory currents decay, the excitatory input re-charges the membranes. The distribution of membrane potentials is again depolarized and a new cycle begins.

The membrane potentials of units that participated in the population spike were set to the reset potential (-67 mV, dark horizontal stripes in Fig. 2.3*A*, bottom) for a short period of time (1 ms) to account for an afterhyperpolarization and a refractory period of interneurons in the model. Such a defined reset reduces the variability in the subpopulation that fired. However, the overall effect of the reset on the variability of the membrane-potential distribution is low because only about one quarter of the population fires in any given cycle.

How is the process described in Figure 2.3*A* affected when the mean excitatory input increases? Figure 2.3*B* shows the behavior of the population when the input rate was doubled to 6,000 spikes/s. The network frequency was hardly affected because the increase in excitation (due to a higher input rate) was counterbalanced by an increase in network (inhibitory) activity (compare Figs. 2.3*A* and *B*). More precisely, increasing the input rate enhances the mean excitatory current experienced by units in the network. Due to the stronger excitatory currents, the distribution of membrane potentials is depolarized faster (increase in the voltage-time derivative, compare Figs. 2.3*A* and *B*), the 'escape rate' at the firing threshold increases, and more units fire before this activity affects the network in the form of inhibitory currents. The more cells are recruited in any given cycle, the larger is the amount of negative charge delivered back to the network and the more the membrane potentials are shifted toward hyperpolarized values. Thus, a steeper ascending phase of the membrane-potential distribution due to a higher input rate is compensated for by a more hyperpolarized trough of the membrane potentials.

Such a dynamic compensation of changing input rates is possible only if the network saturation is low enough: Once a large fraction of the population is recruited at a cycle,

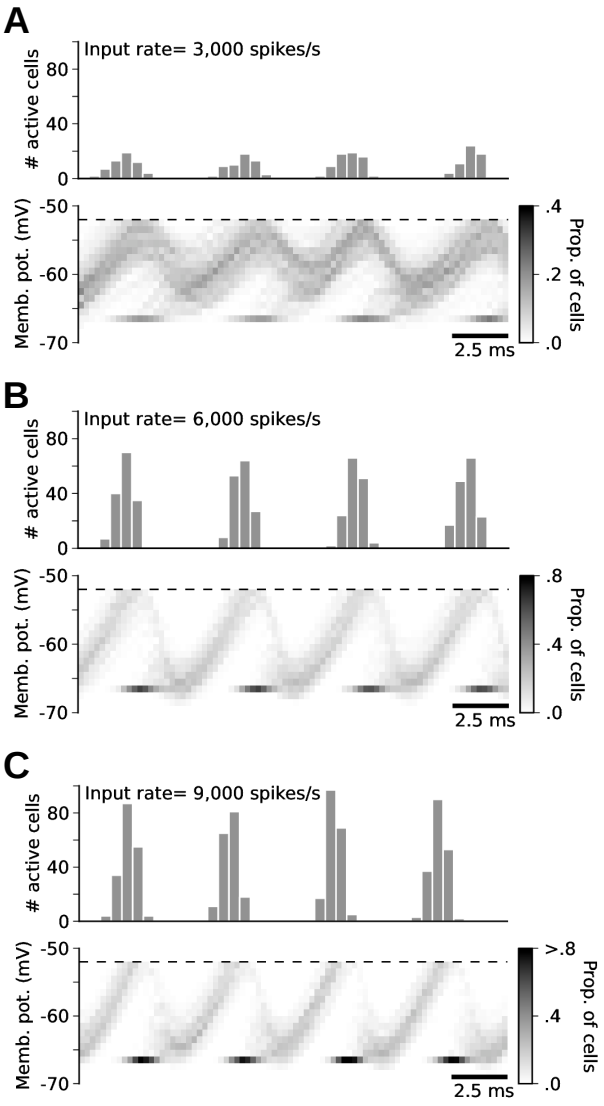

Fig. 2.3: Transition from sparse to full synchrony with increasing input rate. ***A***−***C***, Spike-time histogram (top, bin with 0.5 ms) and membrane-potential distribution (bottom) across the interneuron population during four oscillatory cycles. ***A***, At an input rate of 3000 spikes/s a small random subset of units is recruited in any given cycle (top). The population exhibits a wide distribution of oscillating membrane potentials (bottom) where most units remain subthreshold (i.e., below dashed line). The units that participated in the population spike concentrate at the reset potential during their refractory period (darker horizontal stripes at −67 mV) ***B***, At an input rate of 6000 spikes/s most units (∼75%) are recruited in any given cycle (top). The faster rise of the membrane potentials due to the increased excitation (with respect to *A*) is compensated for by a more hyperpolarized trough (bottom). The population exhibits a narrow distribution of oscillating membrane potentials. ***C***, At an input rate of 9000 spikes/s most units (∼90%) are recruited in any given cycle (top). The faster rise of the membrane potentials due to the increased excitation (with respect to *B*) can no longer be compensated for by a more hyperpolarized trough (bottom); the network is saturated.

further increases in excitatory input can no longer be compensated by a larger recruitment of interneurons. To illustrate this effect, consider the situation depicted in Figure 2.3*B* as an initial state. At an input rate of 6,000 spikes/s (Fig. 2.3*B*), the network already exhibited a high saturation as evidenced by the large fraction of the population that is recruited at any given cycle (∼0.8). When the input was increased from 6,000 spikes/s (Fig. 2.3*B*) to 9,000 spikes/s (Fig. 2.3*C*), the number of units recruited increased from ∼150 to ∼180. This means that the inhibition fed back to the network did not increase proportionally with the increase in excitatory input.

At high saturation, the negative charge fed back to the network in each cycle will remain largely the same, regardless of the input rate. Since the current-integration process departs from nearly the same initial voltage in every cycle, the faster up-shift of the membrane-potential distribution induced by a stronger excitatory drive shortens the period of the oscillation (Fig. 2.3*B* and *C*, bottom).

The saturated or 'low-noise' state observed at high input rates is characterized by a narrow distribution of membrane potentials (Fig. 2.3*B* and *C*, bottom). Such a narrow distribution allows the entire population (or at least a large proportion of it) to reach the threshold (dashed lines in Fig. 2.3) within a small fraction of a cycle (Fig. 2.3*C*, top). Thus, almost all units can fire before the delayed inhibition resulting from this activity is fed back to the network.

Right after such a population spike, the membrane-potential distribution accumulates at or near the reset potential (−67 mV, black horizontal stripes in Fig. 2.3*C*, bottom). At the end, and shortly after this collective reset, units receive massive inhibitory input coming from the spiking population. Due to the narrow population spike involving nearly the entire population there is also little variability of the inhibitory input across cells.

In summary, the high-noise state is characterized by a wide distribution of oscillating membrane potentials. A large fraction of units remain subthreshold and a small random subset of units fires in any given cycle. During such an 'unsaturated' or 'high-noise' state, increases in excitatory drive can be counterbalanced by an increase in the number of units recruited at any given cycle (Fig. 2.3*A*) and the network frequency is insensitive to the input rate. On the other hand, in the 'saturated' state, a large fraction of units is recruited in every cycle, which reduces the variability of membrane potentials across the population, and thereby the noise in the system. During this 'low-noise' state, changes in the excitatory drive result in changes in the network frequency.

2.2.3 Response to ripple-modulated excitatory activity

So far, previous theoretical studies and my own numerical simulations have shown that a network of interneurons can generate ripple oscillations provided that interneurons are excited with sufficiently strong unmodulated activity. Although these findings demonstrate that an interneuron network is capable of self-entrainment, they cannot rule out the co-existence of a putative excitatory pacemaker. In contrast to the inhibition-first model that I have studied so far, excitation-first models rely on different mechanisms to generate strongly modulated excitatory input to the interneurons. Modeling work by others argues that such a modulated excitatory input can be generated, for example, by a sequence of pyramidal cell assemblies (Memmesheimer, 2010) or by interactions via gap junctions in the pyramidal axon plexus (Traub and Bibbig, 2000). Under which conditions could such an oscillatory input entrain an interneuron network that is already capable of self-entrainment? Is it possible that high-frequency, ripple-modulated excitatory input can actually set the frequency of the

interneuronal network?

To address this question, I tested whether ripple-modulated oscillatory excitation can impose its frequency onto the recurrent network of CA1 basket cells. In numerical simulations similar to the ones shown in Figures 2.2 and 2.3, I varied not only the strength of the mean excitatory input but also added an oscillatory component to this input; in particular, I varied the modulation depth and the frequency of this oscillation (Fig. 2.4).

In excitation-first models, the signal that modulates interneuron activity stems from local excitatory afferents. Therefore, I included in the model a set of local afferents that were connected to the interneurons via strong and fast AMPA synapses emulating those found between pyramidal cells and PV^+BC in CA1 (Pawelzik et al., 2002) (Fig. 2.4*A*). I assumed that these local fibers fired according to an inhomogeneous Poisson process where the rate was modulated by a common rhythm with a modulation depth of 100%. In addition, the Schaffer collateral (SC) input was a homogeneous Poisson process, as described in the section 2.2.1. Thus, the total excitatory input provided to the interneurons was a combination of an unmodulated input from SC and oscillatory activity from local afferents (Fig. 2.4*B*, red traces). Because the relative strength of the two inputs is not well constrained by experiments, I varied the relative contributions of the SC and local afferents by adjusting the firing rates of the respective sets of fibers. The parameter 'modulation depth' describes the fraction of the total mean input conductance contributed by the local oscillator.

Since both inputs were delivered via synapses with different strengths (Fig. 2.4*A*, red traces) the respective firing rates were adjusted to provide a constant mean level of excitatory conductance irrespective of the modulation depth. Thereby, I could control the level of engagement of the interneuron network (see Fig. 2.2*D*) and ensure that the firing rates of interneurons were kept within the physiological values observed during SWR.

In the four examples of the oscillatory input in Figure 2.4*B* (red traces), the modulation frequency was 150 Hz, and the mean input was 15 nS. Black traces in Figure 2.4*B* show the network responses to such input (left) and their respective power spectra (right). In the absence of modulated activity (modulation depth = 0), the network oscillated at its natural frequency of ∼190 Hz (top trace). With a modulation depth 0.2, the network activity was not apparently altered: it preserved its natural frequency ∼190 Hz but the effect of the oscillatory input was revealed by a smaller peak at 150 Hz in the power spectrum.

With increasing modulation depth, the network activity was gradually entrained by the excitatory oscillation, as revealed by a gradually stronger peak at 150 Hz (Fig. 2.4*B*, middle traces). At a modulation depth $\geqslant 0.4$, the network frequency was dominated by the excitatory oscillator: most of the peaks in the population activity were locked to the modulated input. However, the network still expressed some intrinsic oscillatory activity. At strong modulation depths (> 0.6), the network was primarily driven by the local input, and the frequency of the population activity was governed by the external 150 Hz oscillation. Thus, excitation-first models can control the oscillation frequency of the recurrent interneuronal network for sufficiently strong oscillatory modulation.

How does the frequency of the local oscillator influence the entrainment? To address this question, I varied the frequency of the local oscillator while keeping the modulation depth constant. Figure 2.4*C* shows the power spectrum (gray scale) as a function of the modulation frequency for a modulation depth of 0.2. At modulation frequencies < 160 Hz, the power spectrum was dominated by the natural frequency of the network (here ∼190 Hz). There were, however, apparent minor peaks in the spectra revealing the oscillatory component introduced by the excitatory activity. Interestingly, the power of this minor peak increased

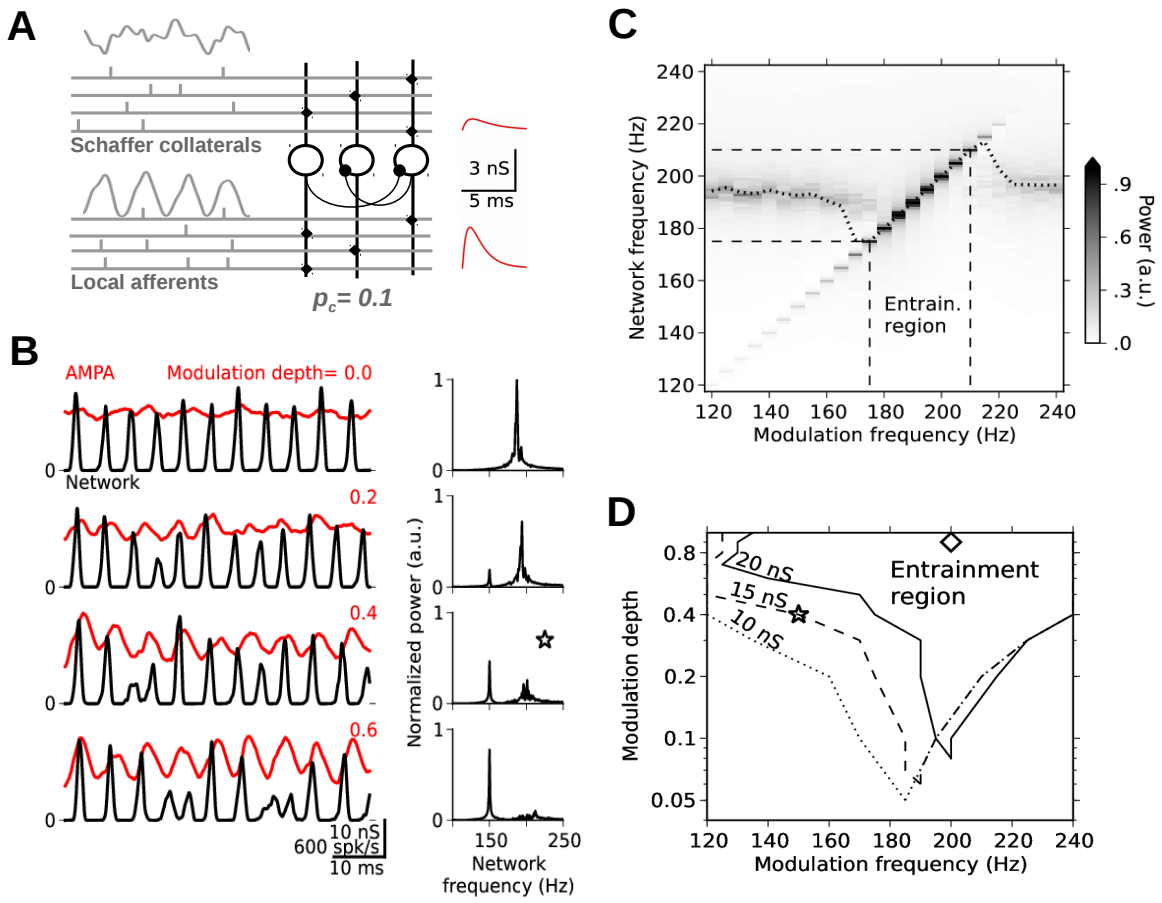

Fig. 2.4: Interneuron-network response to ripple-modulated excitatory input. ***A***, Schematic of input structure: Each interneuron (circle: soma, vertical lines: dendrites) is driven by two sets of excitatory fibers (gray horizontal lines). Schaffer collaterals (SC) fire randomly whereas local afferents provide ripple-modulated activity. Local fibers are connected to the interneurons via stronger and faster synapses compared to SC (EPSGs: red traces). ***B***, Total excitatory conductance (red traces) and network response (black traces) when local activity is modulated at 150 Hz. Modulation depths are varied by controlling the relative contributions of the two sets of fibers shown in A. With increased modulation depth, normalized power spectra of network activity (right) show a gradual replacement of the intrinsic network-oscillation frequency (∼190 Hz at modulation depth=0, top) by the 150 Hz modulation (top to bottom). ***C***, Average spectra of network activity (grayscale) and average peak frequency (dotted line) as a function of modulation frequency (averages across 10 simulations, frequency step: 5 Hz) for fixed modulation depth (0.2). If the modulation frequency is close enough to the intrinsic network frequency, the 150 Hz modulation dominates. This entrainment region is demarcated by dashed lines. ***D***, Arnold tongues for three different levels of mean input (10 nS, dotted; 15 nS, dashed; 20 nS, solid). Entrainment regions expand with increasing modulation depth, and they contract and shift with increasing input level: At modulation depth 0.4 and modulation frequency 150 Hz, the excitatory input sets the frequency of the network only for input levels $\leqslant$ 15 nS (star; Traub and Bibbig 2000). If the network is almost exclusively driven by local ripple-modulated activity (modulation depth$>$ 0.7), an excitatory oscillator can entrain the network in the entire ripple range, for example, at a modulation depth 0.9 and a frequency 200 Hz (diamond; Memmesheimer 2010).

gradually as the modulating frequency approached the natural frequency of the network. At modulation frequencies between ∼170 and ∼215 Hz, the excitatory oscillator was able to fully 'capture' the interneuronal oscillator, entraining its frequency. At modulating frequencies > 220 Hz, the natural frequency of the interneuron network dominated again, and the minor peaks stemming from the modulating activity nearly vanished. Thus, excitation-first models can control the oscillation frequency of a recurrent interneuron network if the input frequency is close enough to the natural frequency of the interneuronal network.

The spectra in Figure 2.4*C* allowed me to identify an entrainment region around the intrinsic network frequency in which the excitatory pacemaker could set the frequency of the interneuron network. I note that in the average spectrogram the more stable peak contributed by the external oscillator is overrepresented in detriment of the more variable intrinsic component. Therefore, I used the average peak frequency (dotted line in Fig. 2.4*C*) to determine the entrainment region (delimited by dashed lines in Fig. 2.4*C*).

I finally quantified how both parameters describing the excitatory input, i.e. modulation depth and frequency together, controlled the entrainment of the interneuronal network. The dashed line in Figure 2.4*D* demarcates the entrainment region (above the line) when a mean excitatory input of 15 nS was provided (as in Fig. 2.4*A*–*C*). The width of the frequency region dominated by the excitatory oscillator expanded with increasing modulation depth, displaying the typical 'Arnold tongue' profile exhibited by self-sustained oscillators under a periodic force (Arnold, 1961). In the present case, these Arnold tongues demarcated the boundary between the region where the frequency was set by the excitatory oscillator (above the line) and the region dominated by the natural frequency of the interneuron network (below the line). At a modulation depth of 0.1, the excitatory oscillator could set the network frequency within only a narrow band (∼10 Hz) around its natural frequency. At a modulation depth of 0.2, this band expanded to cover nearly 40% of the ripple band (175–210 Hz) and at modulations higher than 0.4, the excitatory oscillator could set the network frequency for the entire ripple band (140–220 Hz).

As I have shown in section 2.2.1, the interneuron network requires a minimum level of excitation to self-entrain (Fig. 2.2*D*). Once such an input level is provided, enough units are recruited to establish the effective coupling between the population activity and individual units that is required for network oscillations to ensue (see also Brunel and Wang 2003). With increasing excitation, such coupling becomes stronger as more cells are involved in any given cycle. Would this stronger involvement of the interneurons make the interneuron network less susceptible to external entrainment? To test this, I observed the dependence of the entrainment region on the input level. The three Arnold tongues depicted in Figure 2.4*D* were obtained at mean input levels of 10 nS (dotted), 15 nS (dashed), and 20 nS (solid); at which interneurons displayed mean firing rates of 73, 114 and 147 spikes/s, respectively. With increasing mean input, the Arnold tongues were shifted towards higher frequencies due to the dependence of the natural frequency on the level of excitatory input (see Fig. 2.2*D*). Interestingly, the Arnold tongues also became narrower with increasing mean input. Thus, the region dominated by the external oscillator also depended on the mean excitatory input provided to the interneuron network; the stronger the mean excitatory input to the interneuron network, the more robust its intrinsic frequency becomes.

Let us provide examples to illustrate some implications of these findings. Suppose the interneuron network is driven by an input generated by the axon plexus, as proposed by Traub and Bibbig (2000). In this case, the mean input is 10 nS with a frequency of 150 Hz and a modulation depth of 0.4 (star in Fig. 2.4*D*, estimated from Traub and Bibbig (2000), their

figure 3A). Under those conditions, the network frequency is set by the excitatory pacemaker at 150 Hz because the input parameters are within the entrainment region. Moreover, at such a level of mean excitatory input, the axon plexus could set the frequency in the entire ripple range. However, if the mean input were to be increased to 20 nS (e.g., due to stronger SC input), the frequency would be set by the interneuron network. At this higher level of mean input, the axon plexus can entrain the network frequency only for modulation frequencies > 180 Hz (i.e., closer to the intrinsic interneuron network frequency). In Memmesheimer's model, on the other hand, interneurons are driven almost exclusively by ripple modulated excitatory activity; the random, unmodulated activity they receive is very weak in comparison (Memmesheimer, 2010). At an estimated modulation depth of 0.9 (diamond in Fig. 2.4*D*, estimated from Memmesheimer (2010), *SI-C* and Fig. *S5*), the interneuron network is not capable of setting the frequency at the mean levels of excitatory input we tested.

In summary, ripple-modulated excitatory activity can entrain an interneuron network oscillator within a band around the natural frequency of the latter. The width of this band depends on the mean excitatory input and its modulation depth. With increasing modulation depth of the excitatory input the band expands. Conversely, increasing mean excitatory activity favors the dominance of the interneuron network.

2.3 Discussion

Here I characterized the behavior of a model of the CA1 basket cell network to different levels of excitatory synaptic activity, both unmodulated (Figs. 2.2 and 2.3) and ripple-modulated (Fig. 2.4).

With increasing mean input rate, the network transited from a sparsely synchronized towards a fully synchronized regime (Fig. 2.2*D*). The firing rate of interneurons increased monotonically with the mean excitatory input delivered. Sparsely synchronized oscillations emerged when a minimum firing rate was reached, which corresponds to the minimum activity required to establish an effective coupling between the population and single units (Brunel and Wang, 2003). As the excitatory input was further increased, interneurons could vary their firing rates without altering the network frequency. However, as the mean firing rate of interneurons approached the network frequency, the network transited towards a fully synchronous regime where frequency was also dependent on the excitatory input.

At higher firing rates of interneurons the network became also less susceptible to be entrained by a coexisting excitatory pacemaker (Fig. 2.4*D*). With increasing mean excitation delivered to interneurons, ripple-modulated excitatory input required stronger modulation depths to be able to control the frequency within the ripple band.

2.3.1 Interneuronal activity during ripple oscillations

The behavior of perisomatic targeting interneurons during ripples seems to be consistent with the model presented here. For example, studies *in vivo* have shown that PV^+BC fire strongly locked to the extracellular ripple at rates lower than the ripple frequency (Lapray et al., 2012; Varga et al., 2012). Moreover, some typical traces reported in the literature show that interneurons tend to randomly skip ripple cycles both *in vivo* and *in vitro* (Fig. 2.5). Interestingly, these example traces show an interesting relation between the ripple amplitude and the firing rate of the simultaneously recorded interneuron: Weaker extracellular ripples

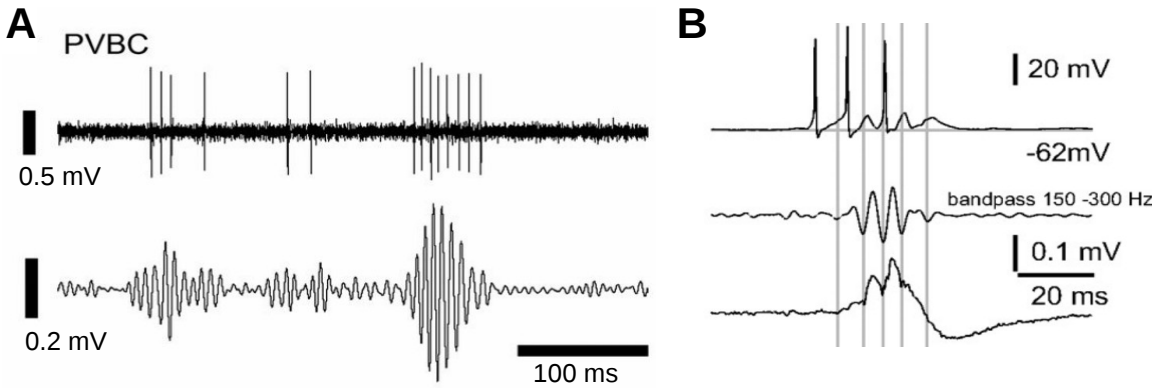

Fig. 2.5: Spiking of perisomatic targeting interneurons during ripple oscillations. ***A***, Parvalbumin-positive basket cell spiking (top) during ripple oscillations (bottom) in the awake mouse (Varga et al. 2012). Higher firing rates appear associated with stronger ripples. ***B***, Current clamp recording of basket cell (top) during ripples (middle) *in vitro*; SWR shown at the bottom (Bähner et al. 2011). Cell firing skips cycles of the ripple-locked subthreshold oscillation (top).

appear accompanied by fewer spikes than their stronger counterparts (Fig. 2.5*A*, see also Ylinen et al. 1995). In light of the findings presented in Figure 2.2, this might reflect the fact that during stronger network activity it is more likely to find interneurons firing at higher rates (Fig 2.2). If we consider that the LFP ripple recorded in *stratum pyramidale* mostly reflects perisomatic inhibitory currents on pyramids, we can interpret the ripple amplitude as a proxy for the putative interneuronal network activity. Thus, stronger ripples in the *stratum pyramidale* would be associated to higher mean firing rate of interneurons, and would therefore reflect a stronger mean excitation to the interneuronal network.

2.3.2 Coexistence of excitatory and inhibitory pacemakers

If we allow the coexistence of excitatory and inhibitory pacemakers, the present results suggest that weaker ripples would be more susceptible to be entrained by modulated excitatory activity. As shown here, an excitatory pacemaker requires lower modulation depths to entrain an interneuronal network receiving low mean excitation (Fig. 2.4*D*). If we consider that the ripple amplitude reflects the mean level of excitatory input to interneurons, as discussed above, it follows that low-amplitude ripples would be more likely entrained by a putative excitatory pacemaker.

2.4 Methods

2.4.1 Model inhibitory neurons

Each interneuron is described by a single-compartment, leaky integrate-and-fire model that resembles the behavior of a fast-spiking basket cell in CA1. The dynamics of the subthreshold membrane potential V_m obeys

$$C_m \frac{\mathrm{d}V_m}{\mathrm{dt}} = g_{\mathrm{leak}}(E_{\mathrm{rest}} - V_m) + I_{\mathrm{syn}} + I_{\mathrm{app}}. \tag{2.1}$$

The leak (resting) membrane potential is $E_{\text{rest}} = -65$ mV. The capacitance $C_{\text{m}} = 100$ pF and the leak conductance $g_{\text{leak}} = 10$ nS yield a membrane time constant of 10 ms (Buhl et al., 1996). The symbols I_{syn} and I_{app} denote the synaptic and injected (applied) currents, respectively. When V_m reaches the threshold voltage $V_{\text{thres}} = -52$ mV, the unit emits a spike. After spiking, V_{m} is reset to the potential $V_{\text{reset}} = -67$ mV and the cell remains refractory for 1 ms.

In spite of its simplicity, the leaky integrate-and-fire model is sufficient to capture basic properties of fast-spiking basket cells such as the absence of spike-frequency adaptation and fast afterhyperpolarization potentials. I empirically measured the current-frequency curve of the interneuron model by varying the value of I_{app} between 0 and 1.0 nA in the absence of synaptic currents. With the selected parameters we obtained a current-frequency curve with a slope of 380 Hz/nA (measured at $I_{\text{app}} = 0.6$ nA) and a rheobase of 0.13 nA. The observed spiking patterns and the current-frequency curve are consistent with hippocampal PV^+ fast-spiking basket cells recorded *in vitro* (Pawelzik et al., 2002; Ferguson et al., 2013) and are also consistent with more sophisticated models of fast-spiking basket cells (Wang and Buzsáki, 1996; Ferguson et al., 2013).

2.4.2 Model synapses

The total synaptic current I_{syn} is described according to a conductance-based model

$$I_{\text{syn}} = g_{\text{e}}(E_{\text{e}} - V_{\text{m}}) + g_{\text{i}}(E_{\text{i}} - V_{\text{m}}) \tag{2.2}$$

where g_{e} and g_{i} are the instantaneous excitatory and inhibitory conductances, respectively resulting from the presynaptic activity. The reversal potential E_{i} of inhibition (*i.e*, chloride) was set to -75 mV, in accordance with reported values (Buhl et al., 1995) and previous models (Wang and Buzsáki, 1996; Bartos et al., 2002). The reversal potential E_{e} of excitatory synapses was set to 0 mV. The time course of a single postsynaptic potential is described by a normalized dual exponential

$$g(t) = g^{\text{peak}} s \left\{ \exp\left[-(t-\tau_{\text{l}})/\tau_{\text{d}}\right] - \exp\left[-(t-\tau_{\text{l}})/\tau_{\text{r}}\right] \right\} \tag{2.3}$$

for $t \geq \tau_{\text{l}}$ and $g(t) = 0$ otherwise. The scaling factor s was set such that $g(t)$ reaches the maximum value g^{peak}, and τ_{r} and τ_{d} are the rise and decay time constants, respectively, of the postsynaptic potential. There is a latency of $\tau_{\text{l}} = 1$ ms between a presynaptic spike and the start of the postsynaptic potential.

Two types of synapses were used: fast GABAergic and AMPA-type synapses. For AMPA-type synapses, I used $\tau_r = 0.5$ ms, $\tau_{\text{d}} = 2$ ms, and $g^{\text{peak}} = 0.8$ nS (Taxidis et al., 2012). The values for GABAergic synapses were tuned according to (Bartos et al., 2002): $\tau_{\text{r}} = 0.45$ ms, $\tau_{\text{d}} = 1.2$ ms, and $g^{\text{peak}} = 5$ nS.

2.4.3 Network model of inhibitory neurons

SWRs can be observed in the isolated CA1 area of ventral hippocampal slices (Maier et al., 2003; Nimmrich et al., 2005; Maier et al., 2011). I therefore constrained the model according to the PV^+BC network in such a small volume of tissue.

Network size. To set the number of interneurons in the network, I obtained two consistent estimates for the number of PV^+BCs. The first estimate is based on the volume of the

stratum pyramidale in an hippocampal slice and the density of PV^+BCs in this region. The typical thickness of an hippocampal slice (0.4 mm) and the dimensions of the CA1 *stratum pyramidale* in ventral hippocampus (0.13 mm × 1.1 mm) (Dougherty et al., 2012) yields a volume of 0.057 mm^3. The density of PV^+ cells in the *stratum pyramidale* was estimated to be $5.4 \cdot 10^3$ cells/mm^3 (Aika et al., 1994). Considering that 60% of PV^+ cells in CA1 are basket cells (Bezaire and Soltesz, 2013), I obtained 185 PV^+BCs contained in a slice.

A second estimate for the number of interneurons was obtained by scaling the total number of 5,530 PV^+BCs in the CA1 area (Bezaire and Soltesz, 2013) by the fraction of the volume of a 400-μm slice. If we approximate the geometry of the hippocampus to a cylinder and consider its septotemporal extension to be ∼10 mm (Patel et al., 2012), a 400-μm slice represents 4% of the total volume. This fraction yields 221 PV^+BCs in a slice. Roughly consistent with both estimates, our simulated network consisted of 200 interneurons.

Connectivity. To estimate the connectivity in the network, I considered that a single PV^+BC can contact on average 64 other PV^+ cells (Sik et al., 1995). Given that 60% of those PV^+ cells are basket cells (Bezaire and Soltesz, 2013), then a PV^+BC contacts on average 38 other cells of the same type. This number corresponds to a connectivity of 20.5% for 185 cells and 17% for 221 cells. In the simluations, I used 20% connectivity.

To keep the model as simple as possible, I assumed that pairs of PV^+BCs were connected with equal probability. In consequence, there was no spatial structure in the connectivity, in contrast to previous models (Wang and Buzsáki, 1996; Bartos et al., 2002; Taxidis et al., 2012).

2.4.4 Excitatory input to the inhibitory network model

Interneurons in CA1 receive excitatory input from CA3 pyramidal cells via the Schaffer collateral pathway (Takács et al., 2012). Here I explain how I constrained the number of Schaffer collateral fibers and the number of excitatory synapses onto interneurons in the model.

CA3 input fibers. The total number of pyramidal cells in CA3 was estimated as 204,700 (Bezaire and Soltesz, 2013). Scaling this number with the ratio 0.04 of the volumes of slice and hippocampus yields 8,200 CA3 pyramidal cells.

Excitatory synapses. In the intact hippocampus each interneuron receives 7,952–17,476 synapses from Schaffer collaterals (Bezaire and Soltesz, 2013). Such collaterals stem from pyramidal cells located within the proximal 2/3 of the septotemporal extension of CA3 (Li et al., 1994). If we consider that each of those synapses corresponds to a pyramidal cell located within such an extension (∼ 6.7 mm) and that the thickness of a typical hippocampal slice preserves 6% of that extension (0.4 mm / 6.7 mm), I expect that roughly 6% of the total number of excitatory synapses can be driven by the CA3 pyramidal cells remaining in a slice. From this estimate I obtained 480–1,050 input synapses per interneuron. For the simulations I set the number of Schaffer collateral synapses to 780.

Connectivity. Considering an intermediate number of 780 synapses per interneuron and the number of CA3 pyramids in an hippocampal slice, I estimated a connection probability of $p_{\text{share}} = 0.095$ as the ratio between these two quantities. This number also describes the

average shared input across interneurons and therefore quantifies the correlations introduced by the connectivity. The estimated number of synapses (780) and the number of interneurons (200) in the network yield a total 156,000 input synapses from the Schaffer collaterals. This number of synapses is much larger than the estimated number of 8,200 CA3 pyramidal neurons in the slice. Therefore, a typical CA3 pyramidal cell must provide input to many different interneurons. Indeed, a single Schaffer collateral fiber from CA3 can establish *en passant* excitatory synapses with many interneurons in CA1. Consequently, different PV^+BCs share some of its excitatory drive.

Driving activity. I assumed that the driving CA3 pyramidal cells were statistically independent spiking units that can be described by homogeneous or inhomogeneous Poisson processes. Every driving unit fired according to a homogeneous Poisson process with a constant rate. In this condition, the total Poisson rate delivered to each inhibitory cell in the network corresponds to the number of synapses per interneuron (here: 780) multiplied by the rate of the driving units. The rate of the driving units was varied in a wide range between 1.28 and 19.23 spikes/s. The input strength of the network is then given as the total rate per cell (range: 1,000–15,000 spikes/s), which can be interpreted as the number of excitatory synaptic events experienced by a single interneuron per unit time.

2.4.5 Numerical simulations

Simulations consisted in 1 s of simulated time (time step = 10μs). For each numerical simulation, a new instance of the model was created, *i.e.* the network and the external input connectivity were randomly rewired. All simulations, data analysis, and visualization of results were performed in Python (www.python.org). The network model was implemented using the spiking network simulator "Brian" (Goodman and Brette, 2009).

2.4.6 Analysis of the network activity

Power spectra of the network activity were computed from the Fourier transform of the autocorrelogram of the collective activity. The network frequency was obtained from the peak of the power spectrum. The network saturation was defined as the average number of inhibitory units recruited in a network oscillation cycle. Since in simulations units rarely fire more than once in each cycle, we obtained an approximation of the saturation from the average number of spikes generated by the population in one cycle. Unit firing rates were estimated from the number of spikes generated during the time of a simulation ($\sim$ 1 s). Regularity of unit firing was measured by the coefficient of variation (CV) of the interspike interval. The coherence of the oscillation was derived from the power spectrum as the square root of the ratio between the power of the peak and the power at zero frequency (Kempter et al., 1998).

3 Transient oscillations

The transient hippocampal oscillations that appear during sleep and awake immobility express frequencies spanning from fast-gamma (90–140 Hz) to ripples (140–220 Hz). Spontaneous oscillations recorded in vitro are restricted to the ripple band. Both ripple and fast gamma episodes display higher frequencies during the first half of the event, followed by a monotonic deceleration during the second half. Here I show in silico that a transiently excited interneuron network exhibits such a frequency signature, but frequencies are limited to the ripple band. However, when the interneurons are driven by the local pyramids to which they project, the frequency signature is expressed only in the fast-gamma band. In such a feedback-loop network, the oscillation frequency strongly depends on the excitatory input delivered, and oscillations can be evoked predominantly in the fast gamma range and lower ripple band. In contrast, when interneurons are directly driven, frequency is less sensitive to input drive, and oscillations are constrained to the ripple band. In conclusion, oscillations evoked by depolarization of local pyramids provide a better description of transient events in the fast-gamma range. On the other hand, oscillations in the ripple range, particularly those evoked in vitro, are better described by a scenario in which the interneuron network dominates. Considering the excitatory projections to CA1 and the differential connectivity between interneurons and pyramidal cells located in the deep and supperficial layers of the stratum pyramidale, I propose two putative excitatory pathways that favor the expression of either ripples or fast-gamma.

3.1 Transient oscillations in the CA1 network

Studies performed on rats *in vivo* have shown that the transient oscillations emerging in CA1 during slow wave sleep and awake immobility express a wide range of frequencies spanning from ∼80 to ∼200 Hz. (Csicsvari et al., 1999a; Sullivan et al., 2011) (Fig. 3.1*A*). The frequency distribution of such episodes exhibit a bimodality that allow us to distinguish a fast gamma band (90-140 Hz) and a ripple band (140-220 Hz) (Fig. 3.1*B*).

An early hypothesis suggested that ripples emerge in CA1 whereas fast gamma is inherited from CA3 (Csicsvari et al., 1999a). This view was later challenged by Sullivan et al. (2011) who showed that both fast gamma and ripple episodes exhibit low (<0.2) coherence between CA3 and CA1, indicating that transient events in both bands might be generated *de novo* in CA1.

Although physiologically distinct, both event types exhibit remarkable similarities. They are associated with sharp-wave sinks in the *stratum radiatum*, which reflect the depolarization of the apical dendrites of CA1 pyramids due to the excitatory input stemming from CA3. Interestingly, larger-amplitude events appear associated with frequencies in the ripple range whereas lower-amplitude events contain oscillations in the fast gamma range (Csicsvari et al., 1999a; Sullivan et al., 2011; Stark et al., 2014).

Another remarkable similarity among these transient oscillations is that they exhibit a higher frequency during the first half of the episode, followed by a monotonic deceleration

during the second half (Fig. 3.1*C*). Such a peculiar time course of the instantaneous frequency during single events has been widely reported in the literature (Ponomarenko et al., 2004; Nguyen et al., 2009; Stark et al., 2014; Hulse et al., 2016) and has been termed 'intra-ripple frequency accomodation' (IFA). The mechanisms generating such a phenomenon have not been studied so far.

In spite of the similarities, several studies have shown that ripple and fast-gamma events can be dissociated (Bragin et al., 1999; Csicsvari et al., 2000; Nakashiba et al., 2009). One fact that might be pointing at different substrates underlying ripples and fast-gamma is that *in vitro* transient events display frequencies that are limited to the ripple band, both in rat and mice (Maier et al., 2003, 2011; Behrens et al., 2005; Papatheodoropoulos et al., 2007; Koniaris et al., 2011). For example, in Maier et al. (2011), transient events recorded in head fixed awake mice displayed an average frequency of 136 Hz (range: 127 to 147 Hz). However, slices obtained from the same type of mice displayed spontaneous events with an average frequency of 194 Hz (range: 160 to 240 Hz). The process by which fast gamma is selectively disrupted *in vitro* is not clear.

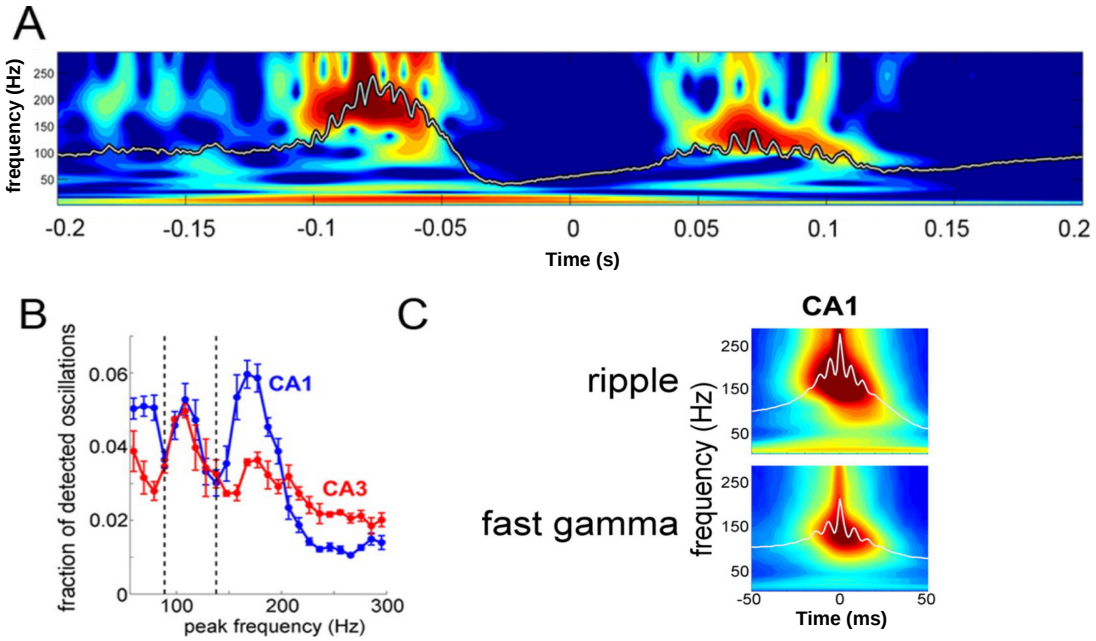

Fig. 3.1: Ripples and fast gamma oscillations. ***A***, Example CSD traces (white) of ripple and fast gamma oscillations from the CA1 stratum pyramidale in a sleeping rat, overlaid on their respective wavelet spectrograms. ***B***, Distribution of the peak spectral frequency (calculated via FFT) of oscillatory high-frequency episodes detected in the CA1 and CA3 pyramidal layers (mean ± SEM; n = 9 animals). Dashed lines represent minima at 90 Hz separating gamma and fast gamma oscillations, and at 140 Hz separating fast gamma (90–140 Hz) and ripple (>140 Hz) oscillations in CA1. ***C***, Dynamic of oscillatory episodes in CA1, illustrated by averaged wavelet spectrograms triggered by ripple peaks and fast gamma oscillation peaks, respectively (Sullivan et al., 2011; reproduced with permission from Society for Neuroscience).

Previous *in silico* models have shown that the high frequencies that can be evoked in recurrent interneuronal networks (such as those described in the previous chapter) can be

slowed down in the presence of reciprocal connections between pyramids and interneurons (Brunel and Wang, 2003; Brunel and Hakim, 2008). In light of those results, it has been suggested that oscillations in the ripple band are predominantly paced by interneuronal interactions, whereas fast gamma generation requires the recruitment of the pyramidal-interneuron (P–I) loop (Brunel and Wang, 2003; Buzsáki, 2015). The aforementioned studies, however, were limited to the steady-state response of the network, and did not explore the time course of the frequency within transiently evoked events.

In the present chapter I focus on the frequency dynamics of transient events evoked in two basic CA1 networks motifs. First, I focus on the instantaneous frequency displayed by a transiently excited interneuron network in isolation. I then describe how this dynamics is affected by the inclusion of the P–I loop in addition to the recurrent interneuronal network. I also show how these two network motifs express oscillations in different frequency ranges.

3.2 Interneuronal network response to transient stimulation

In the previous chapter I have characterized the response of an interneuron network to persistent stimulation, which limited the analysis to the steady-state response of the network frequency.

Here, I focus on the response of the interneuron network when driven by a transient excitatory input reminiscent of the Schaffer collateral activity during SWRs (Fig. 3.2*A*). The analysis will be focused on the frequency dynamics during the time course of the stimulation.

To drive the network, an excitatory burst was generated by allowing 1,400 pyramids ($\sim$ 17% of the population of CA3 pyramidal cells in a slice) to fire once at a random time drawn from a normal distribution with standard deviation $\sigma = 7$ ms. In this way, I generated activity that resembled that of pyramidal cells in CA3 during a SWR event (Hájos et al., 2013). The driving population was randomly connected to the interneuron network with probability $p_{\text{share}} = 0.095$, which yields 133 synapses per interneuron, as suggested by the estimated CA3-CA1 connectivity (for details, see Methods at the end of this chapter). To provide the baseline excitatory activity observed between SWRs (Schlingloff et al., 2014), additional 6,800 driving units fired randomly at a rate $\sim$ 1.85 spikes/s. Using the same connectivity $p_{\text{share}} = 0.095$, every interneuron experienced a mean background input rate of 1,200 spikes/s. Since I aimed at understanding the generation of ripple oscillations in a CA1 interneuron network in the absence of an external pacemaker, I neglected any rhythmic excitatory activity in the input from CA3 or the CA1 local network (Maier et al., 2011).

3.2.1 Intra-ripple frequency dynamics

For transient stimulation (Fig. 3.2*B*, middle, gray trace), the interneuron network generated a few cycles of oscillatory activity in the ripple-frequency range (Fig. 3.2*B*, middle, black trace). Interestingly, the frequency during the first half of the transient response ($t < 0$) was apparently higher than during the second half ($t \geq 0$). To quantify the time course of the instantaneous network frequency in more detail, I calculated the wavelet spectrogram of the output rate of the network (Fig. 3.2*B*, top). From this spectrogram, I obtained the frequency of maximum power as a function of time (white line in Fig. 3.2*B*). The time course of this instantaneous frequency revealed that during the first half of the event the ripple-frequency exhibited a peak that was followed by a monotonic decrease during the second half. Such a signature in the instantaneous frequency is consistent with IFA (Ponomarenko et al., 2004;

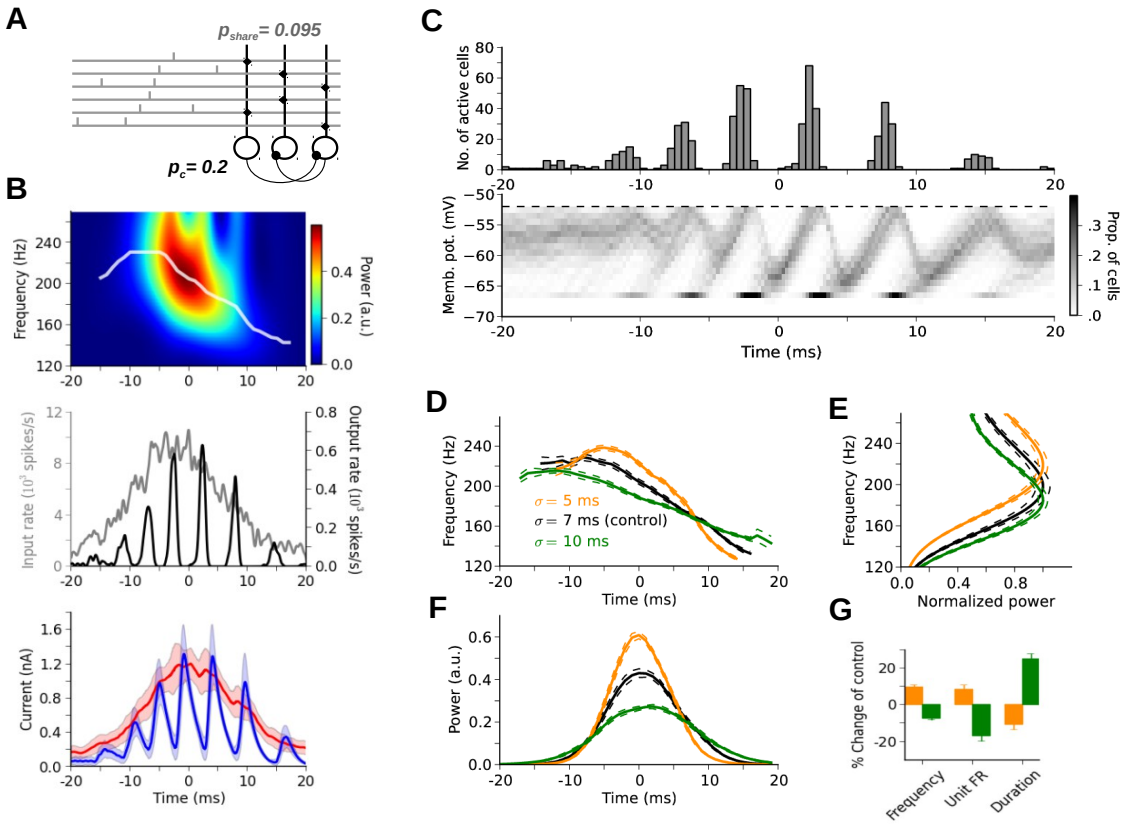

Fig. 3.2: Network response to transient stimulation. ***A***, Interneurons are randomly interconnected with probability p_c= 0.2. The driving population is randomly connected to the interneuron network with probability $p_{\text{share}} = 0.095$ (black circles). Excitatory fibers (gray lines, only 6 shown) from the bursting subpopulation (1400 units) fire once with a normally distributed timing. The remaining 6,800 fibers (not shown) fire randomly and provide a total background rate of 1,200 spikes/s to each interneuron. ***B***, Top: Wavelet-spectrogram and instantaneous peak frequency (white trace) of the transient response (black trace in middle). The transient response exhibits intraripple frequency accommodation (IFA). Middle: Overlay of the total input activity (gray trace, input rate) and response of the interneuronal network (black trace, output rate). The network responds with a modulated oscillation whose envelope lags the input burst. Bottom: Mean synaptic currents across the population generated by the excitatory input (red) and the inhibitory recurrent response (blue). On the ascending phase of the input, inhibitory peaks remain slightly below the ongoing excitatory current. The opposite occurs during the descending phase. ***C***, Spike-time histogram (top) and time course of membrane-potential distribution (bottom). During an initial stage ($t \lesssim -5$ ms), a wider distribution of membrane potentials show subthreshold oscillations that increase in amplitude, denoting an unsaturated (high noise) state. This initial stage is followed by a saturated (low noise) state ($t \gtrsim 0$ ms). ***D***, Average IFA signatures obtained at different burst widths σ. The black trace corresponds to the control value $\sigma = 7$ ms used also in *B* and *C*. Broader input bursts ($\sigma = 10$ ms, green) evoke shallower IFA signatures whereas narrower input bursts ($\sigma = 5$ ms, orange) evoke sharper IFA signatures. ***E***, Average power spectra obtained for the same burst widths as in *D*. Broader input bursts evoke slower ripples. ***F***, Average time course of power obtained for the same burst widths as in *D*. Broader input bursts evoke longer lasting but weaker transient responses. ***G***, Changes in frequency, firing rate (FR), and duration with respect to the control value $\sigma = 7$ ms. Each average trace was obtained from 20 simulations.

Nguyen et al., 2009; Sullivan et al., 2011).

To get insight into the mechanism behind IFA, I analyzed the network response in relation to the input rate (gray trace in Fig. 3.2*B*, middle) in more detail. The network synchronized within milliseconds after the beginning of the input burst. The amplitudes of the successive peaks of the network activity rose and decayed, following the input activity with some delay. Thus, the network response conformed a modulated oscillation with an envelope that lagged the input burst by a few milliseconds. Figure 3.2*B*, bottom, shows the population-averaged excitatory current (red trace) and inhibitory current (blue trace) that resulted from the activity of the driving units and the response of the network, respectively. During the first half of the event ($t < 0$), the excitatory current increased and the sequence of increasing inhibitory peaks remained slightly below the ongoing excitatory current. Conversely, during the second half of the event ($t \geq 0$), the excitatory currents decreased, but the sequence of decreasing inhibitory peaks were slightly above the ongoing excitatory current. Thus, the delayed response of the network with respect to the input burst generated a time course of synaptic activity that was initially dominated by excitation and later by synchronized inhibition. Note that the time axis was centered ($t = 0$) at the peak of the mean excitatory current because this enables a comparison with the *in vitro* experiments described later.

3.2.2 Mechanisms of intra-ripple frequency accommodation

Why is the instantaneous frequency asymmetric with respect to the symmetric ascending and descending phases of the excitatory drive? I wondered whether this hysteresis-like behavior could be related to the observed mismatch between excitation and inhibition during the time course of a single SWR-like event. In our model, excitation is the main source of noise to the system. On the other hand, the synchronized inhibition provided by the network in response to the excitatory drive tends to suppress noise in the system (as demonstrated in Figs. 2.2 and 2.3). It could be argued that the network is in a high-noise state at the beginning of the stimulation, when the network starts to synchronize and excitation dominates. During the stimulation, the network gradually moves toward a state of low noise, where the network is highly synchronized and inhibition is more prominent. We have shown in Figure 2.2*D* that the network frequency in high- and low-noise states responds differentially to changes in excitatory drive. Accordingly, the initial, sparsely synchronized state favors higher and more steady network frequencies whereas in the later, fully synchronized state the network frequency depends on the strength of the excitatory drive.

To track the evolution of the state of the network during the transient stimulation, I observed the time course of the membrane-potential distribution underlying the network activity (Fig. 3.2*C*). At an initial stage, before the onset of the network oscillations, the population exhibited a wide distribution of membrane potentials that hovered below the threshold (Fig. 3.2*C*, bottom, $t \lesssim -15$ ms). Previous modeling studies showed that in such a condition, the onset of the oscillation occurs at a frequency that is largely determined by the latency and rise time of GABAergic synaptic transmission (Brunel and Wang, 2003). During the ascending phase of the excitatory activity (-12 ms $\lesssim t \lesssim -5$ ms), the network exhibited such sparsely synchronized oscillations: the periodic peaks in the population activity (Fig. 3.2*C*, top) were associated with a wide distribution of membrane potentials (Fig. 3.2*C*, bottom) . At this time interval, the increase in excitatory drive was counterbalanced by the increase in network, *i.e.* inhibitory, activity. This compensation was also reflected in the increasing amplitude of the membrane potential oscillations, i.e., membrane potentials gradually reached more hyperpolarized values. Up to $t \lesssim -5$ ms, the behavior of the network was

consistent with a high-noise state. As the excitatory input reached its maximum, the network activity became more synchronous, and the membrane-potential distribution became narrower. Once a large fraction of the population was recruited in one cycle ($0 \lesssim t \lesssim 10$ ms), the amplitude of the membrane-potential oscillations saturated. Units began to integrate the input departing from nearly the same membrane potential, i.e., close to the reset potential. Thereby, the inter-peak interval depended on the magnitude of the excitatory input, which is a signature of the saturated regime (see also Fig. 2.3).

To conclude, IFA can be explained by interactions within the interneuron network. Its delayed response to the excitatory input burst generates a time course of synaptic currents that is initially dominated by coarse excitation and later by the synchronized inhibition. This timing of excitation and inhibition initially favors the emergence of a high-noise, sparsely synchronized state characterized by a high oscillation frequency, and later favors a low-noise, fully synchronized state in which the network frequency is sensitive to the decreasing input drive.

3.2.3 Input burst width affects frequency dynamics

The proposed mechanism governing IFA predicts that the prominence of the effect can be reduced by providing a transient excitatory stimulus that develops more slowly and has a lower maximum amplitude. An input that grows and decays with shallower slopes may reduce the mismatch of the instantaneous magnitude of the excitatory input current and the delayed network activity that generates inhibitory currents (Fig. 3.2*B*, middle); and a lower maximum amplitude of excitation may reduce the achieved level of saturation.

To test this prediction, I analyzed the response of the interneuron network to input bursts with different widths. The burst width was specified by the standard deviation σ of the distribution from which the spike times of the driving population were drawn. Narrower distributions give rise to input rates that develop faster and exhibit higher peak values. Since every unit in the driving population fires once during the burst, the burst width affects only the rate at which spikes are delivered to the network; the total number of input spikes (∼1,400) generated during a single burst remains unchanged.

Figure 3.2*D* shows the average IFA signatures obtained at three different values of input burst widths ($\sigma = 5, 7$, and 10 ms). Consistent with an initial high-noise state, the onset frequency remained nearly the same for the three conditions. Broader input bursts (larger σ) stretched the IFA signature in time, resulting in frequency traces that started to decay earlier and slower. Figures 3.2*E* and 3.2*F* show the normalized power spectra and the time courses of power in the ripple band for the three analyzed conditions, respectively. Broader and lower-amplitude input bursts generated responses with lower maximum frequencies (Fig. 3*E*, $\sigma = 5$ ms: 219.6 ± 1.3 Hz for $n = 20$ simulations; $\sigma = 7$ ms: 200.1 ± 1.6 Hz; $\sigma = 10$ ms: 185.5 ± 1.1 Hz) and longer durations (Fig. 3*F*, $\sigma = 5$ ms: 25.3 ± 0.4 ms; $\sigma = 7$ ms: 28.4 ± 0.6 ms; $\sigma = 10$ ms: 35.4 ± 0.5 ms). The mean firing rate decreased with broader input bursts ($\sigma = 5$ ms: 135.4 ± 1.5 spikes/s; $\sigma = 7$ ms: 124.7 ± 2.0 spikes/s; $\sigma = 10$ ms: 103.8 ± 1.5 spikes/s; Fig. 3*G*).

To conclude, for the case of an isolated interneuron network, the temporal structure of the transient excitatory drive modulates the IFA shape and, in particular, also the peak frequency of ripple events.

3.3 Oscillations in a model of the CA1 network

In the previous section, I have shown that the time course of excitation plays a pivotal role in the development of IFA. However, I only considered the case of an isolated interneuron network that is driven by a 'foreign' (CA3) population of pyramids. In such scenario, interneurons cannot provide inhibitory feedback to the pyramidal cell population that is driving them. How would the frequency dynamics be affected when interneurons are driven by the local pyramids to which they project? Would IFA be disrupted in such a closed loop scenario? To address these questions, I extended the interneuron network model by including pyramidal cells. The pyramids were modeled as point integrate-and-fire units which parameters were adjusted according to Bähner et al. (2011). In this new model, the 200 units in the interneuron network were reciprocally interconnected with a population of 12,000 CA1 pyramids. Pyramids were randomly connected to the interneurons with a probability $p_c = 0.1$ via fast AMPA-type synapses (Pawelzik et al., 2002). The interneurons, in turn, were connected back to the pyramids with probability $p_c = 0.3$ (Pawelzik et al., 2002) via fast and strong GABA-type synapses (Bartos et al., 2002). Pyramids were also reciprocally and sparsely interconnected with probability $p_c = 0.01$ via AMPA-type synapses (for details, see Methods at the end of this chapter).

3.3.1 Induced high-frequency oscillations: From *in vivo* to *in silico*

To analyze the response of the closed-loop network upon depolarization of local pyramidal cells, I implemented an *in-silico* version of the experiment described in Stark et al. (2014) (Fig. 3.3). In this experiment, fast oscillations (>80 Hz) were evoked by optogenetic depolarization of a small group (80–100) of pyramidal cells in CA1 (Fig. 3.3*A*). When pyramids were excited by a waveform mimicking the SWR envelope, oscillations emerged during the entire time course of the stimulation, predominantly in the fast gamma range (Fig. 3.3*B* and *D*). Interestingly, such induced high-frequency oscillations (iHFO) shared some features with their spontaneous counterparts: They exhibited IFA and their frequency increased with the intensity of light applied to the pyramids (Fig. 3.3*C* and *D*). Thus, iHFOs provide a model of hippocampal transient oscillations that is amenable to *in silico* implementation: It requires considerably less parameters (e.g. connectivity from CA3 to CA1 does not need to be specified) and allows direct control of the input conductances for easier comparison with experimental results.

To emulate iHFO in the closed-loop model (Fig. 3.4*A*), pyramids were equipped with excitatory conductances aimed at mimicking channelrhodopsins (ChR). Such conductances could be externally driven, independently from the AMPA-type synapses mediating the network connectivity (for details, see Methods at the end of the chapter).

3.3.2 Interneuron network under indirect drive

In line with Stark et al. (2014), I hypothesize that iHFO are generated due to the recruitment of the interneuron network by the activity induced on the local group of depolarized pyramidal cells. Thus, iHFOs correspond to the extreme scenario where interneurons are exclusively driven by local afferents provided by pyramids in CA1. In this limiting case, interneurons can exert inhibitory control on the very population that is driving them. Consistently, I neglected any form of direct excitation (i.e. stemming from CA3) onto interneurons. Since

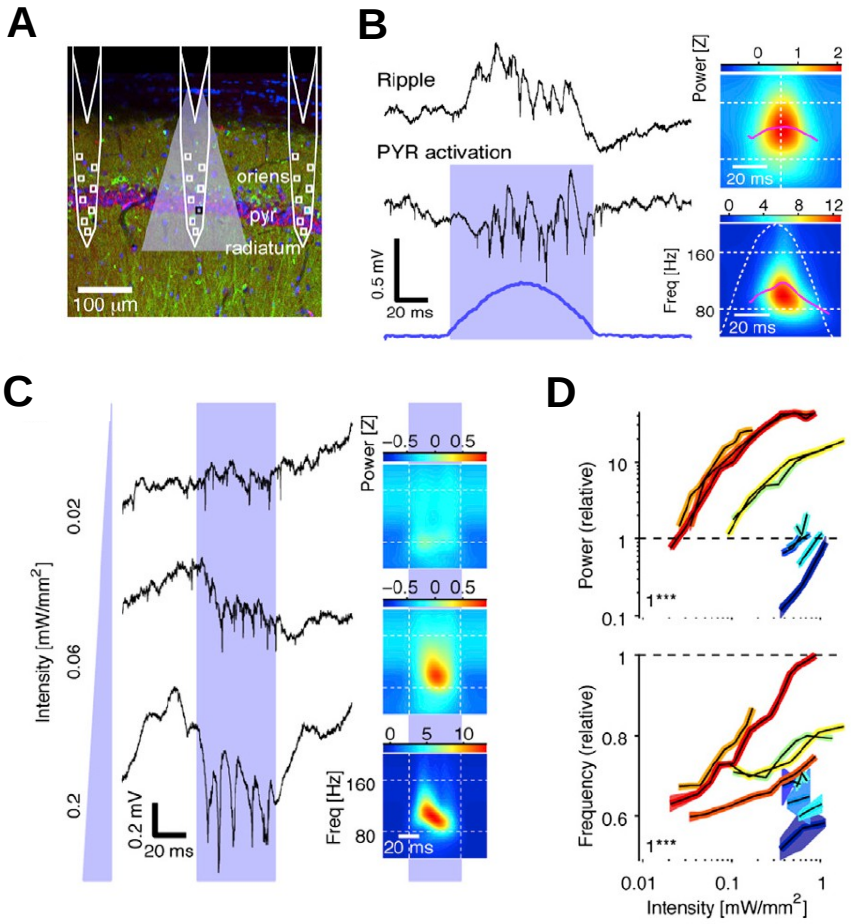

Fig. 3.3: Local activation of pyramidal cells induces high-frequency oscillations (HFOs). ***A***, Schematic of three diode-probe shanks overlaid on a confocal image of ChR2 expression in CA1 pyramidal cells. ***B***, HFOs induced in a freely moving mouse (0.14 mW/mm2). Right: time-frequency decomposition (n = 367 spontaneous or n = 20 induced events). ***C***, Left: traces during individual pulses (50 ms), plotted versus light intensity at the middle of the CA1 pyramidal layer. Right: time-frequency decomposition (n = 20 induced events). Weaker light only induces spiking, whereas oscillations of increasing amplitude and frequency are induced with stronger light. ***D***, Power and frequency (scaled by the properties of the same-site spontaneous ripples; bands: mean ±SEM, n = 10 experiments in four freely moving mice) increase with light intensity (Stark et al., 2014; reproduced with permission from Elsevier).

the input to the interneurons is indirectly provided via depolarization of pyramids, I will refer to this condition as 'indirect drive'.

To evoke iHFO in the model, a random subpopulation of 100 pyramids was depolarized by driving their tonic excitatory conductances with Gaussian intensity profiles ($\sigma = 13$ ms). The peak conductances applied to each cell were normally distributed across the population with constant variability ($CV = 0.5$; see Methods at the end of the chapter). The mean amplitude of this distribution was varied to provide different levels of input to the pyramids (Fig. 3.4*A*, solid and dashed green traces:mean ± std, respectively).

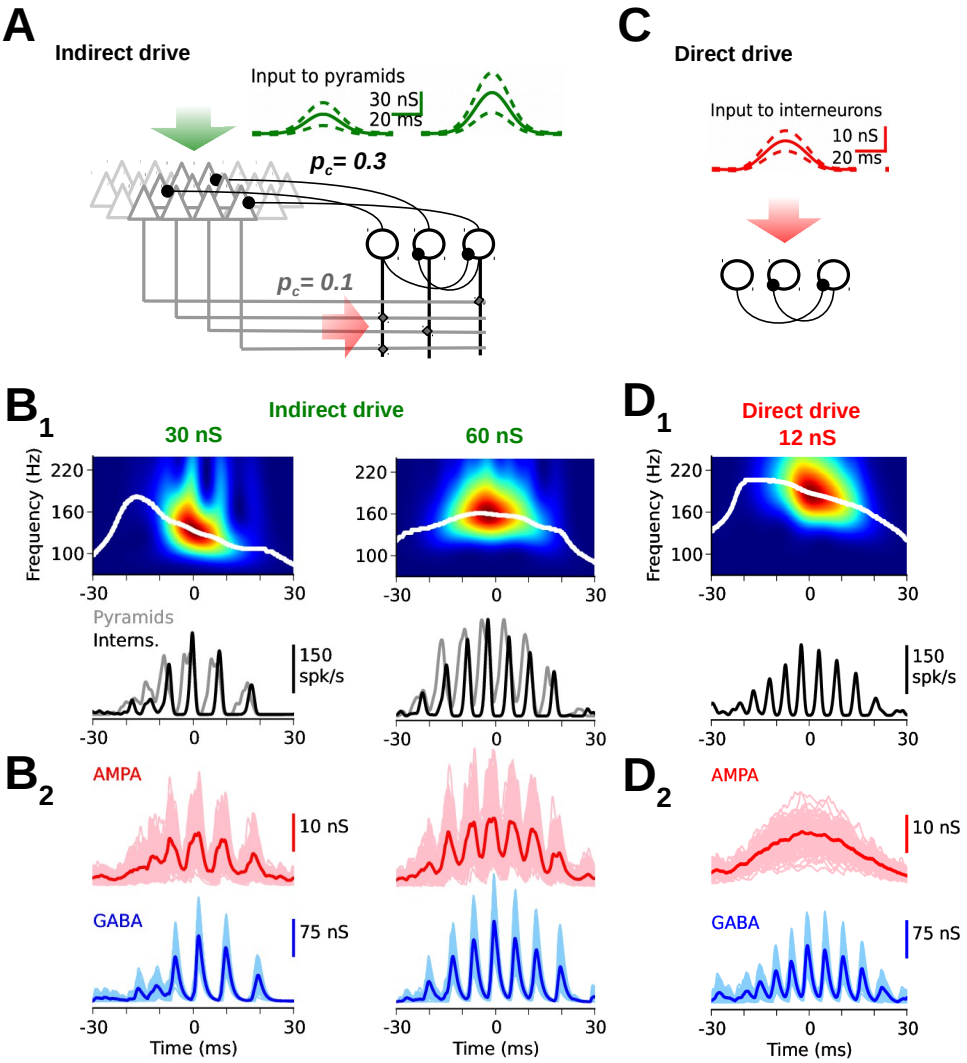

Fig. 3.4: Induced oscillations under two driving conditions. ***A***, A population of pyramids (gray triangles, 12,000 units) is reciprocally interconnected with an interneuron network (black circles, 200 units; connection probabilities p_c: pyr→int = 0.1, int→pyr = 0.3, pyr→pyr = 0.01). During indirect drive, a subpopulation of 100 pyramids is excited with Gaussian bursts (green traces, σ = 13 ms). Burst amplitudes were normally distributed across neurons (green trace: mean, dashed: ± std). Average amplitude was varied across simulations to provide different levels of input. ***B***, Network response to indirect drive for the two input levels depicted in A (green traces, left and right, respectively). *B1, top:* Wavelet-spectrogram and instantaneous peak frequency (white trace) of the interneuron population activity (black trace below). At low input (30 nS, left), the transient response exhibits intraripple frequency accommodation (IFA) at ∼130 Hz. At high input (60 nS, right), the frequency follows excitation at ∼155 Hz. *Bottom:* Overlay of the pyramidal population (gray trace) and interneuronal population (black trace) activities. Pyramids lead interneurons. *B2*, Synaptic conductances across the interneuron population. ***C***, The isolated interneuron network (black circles) is directly driven with normally distributed Gaussian bursts (red traces, σ = 14 ms, average peak= 11.7 nS). Burst profiles and variability were adjusted to resemble the excitatory input shown in *B2* (right, red trace) but devoid of the oscillatory component. ***D***, Same as *B* when the interneuron network is directly excited with the input depicted in *C*. The network response displays the stereotypical IFA shape at ∼186 Hz. The directly driven interneuronal network requires comparably lower excitation to generate oscillations in the ripple band.

Figure 3.4B shows the response of the network at the two levels of input to the pyramids depicted in Figure 3.4A (left and right, respectively). Both pyramids and interneurons displayed a transient oscillation in their population activities, with pyramids leading interneurons (Fig. 3.4B_1, gray and black traces, respectively). Consistently, interneurons experienced strongly modulated excitatory and inhibitory inputs (Fig. 3.4B_2, red and blue traces, respectively). At low input (30 nS, left), the transient response exhibited intraripple frequency accommodation (IFA) at ∼130 Hz (Fig. 3.4B_1, top left). When input to pyramids was increased to 60 nS (right), the frequency of the oscillation increased from 130 to 155 Hz but the instantaneous frequency lost the stereotypical IFA shape (Fig. 3.4B_1, top right).

With increasing input level, the interneuron network responded not only with a higher network frequency but also with stronger activity (Fig. 3.4B_1, black traces), resembling a state of high saturation. As a consequence, the network seemed to achieve a level of high saturation already at the beginning of the event, as evidenced by the instantaneous frequency, which followed the time course of the excitatory input (Fig. 3.4B_1, top right).

3.3.3 Interneuron network under direct drive

In the previous subsection I showed that during the indirect drive condition, interneurons experienced strongly modulated excitatory activity stemming from the entrained population of pyramids (Fig. 3.4B_2, red traces). I wondered how the isolated interneuron network would respond if it was directly driven by the same level of excitatory input but devoid of oscillatory modulation. To do that, I equipped the interneurons with the same ChR-mimicking conductances used to depolarize pyramids and directly drove them with Gaussian bursts (Fig.3.4C, as in Schlingloff et al., 2014). During this direct-drive condition, the Gaussian bursts were tuned to resemble a low pass version (<30 Hz) of the excitatory conductances depicted in Figure 3.4B_2 (right, red traces). The amplitudes were normally distributed across the population of interneurons with the same variability exhibited by the filtered AMPA traces obtained from the indirect drive condition (for details, see Methods at the end of the chapter).

The slow (<30 Hz) component of the excitatory conductances depicted in Figure 3.4B_2 (right, red traces) exhibited an average peak of 11.7 nS (σ = 14 ms) and a variability of CV = 0.28. When such activity was directly delivered to the interneurons, the network activity displayed oscillations at a frequency of 186 Hz (Fig. 3.4D_1, top). When compared to the indirect-drive condition (Fig. 3.4B_1, right) it was apparent that the interneuronal network activity was considerably lower (black trace in Fig. 3.4D_1). This lower unit activity during the direct-drive condition might be indicative of a lower state of saturation of the network, which might also explain the rescue of the IFA signature in the direct-drive condition (Fig. 3.2D_1, top).

3.3.4 Network response under indirect *vs* direct drive

The phenomenology described in Figure 3.4 suggests that the network frequency exhibits different responses to excitatory input under the indirect-drive versus the direct-drive conditions. To characterize this differential response in a systematic way, I first focused on the network frequency in response to a wide range of input levels that were delivered under both conditions (Fig. 3.5A).

For the indirect-drive condition, I applied a range of peak conductances to the pyramids spanning from 10 to 75 nS. Such range of input resulted in peak input conductances to

the interneurons spanning from 3.5 to 17 nS. For easier comparison with the direct-drive condition, I plotted the network frequency of each event as a function of the average peak of the filtered (<30 Hz) excitatory input experienced by interneurons (Fig. 3.5*A*, triangles). Within the range of inputs tested, network frequency increased linearly with excitatory input to interneurons, covering almost the entire fast gamma range and part of the ripple band (range: 93 to 172 Hz).

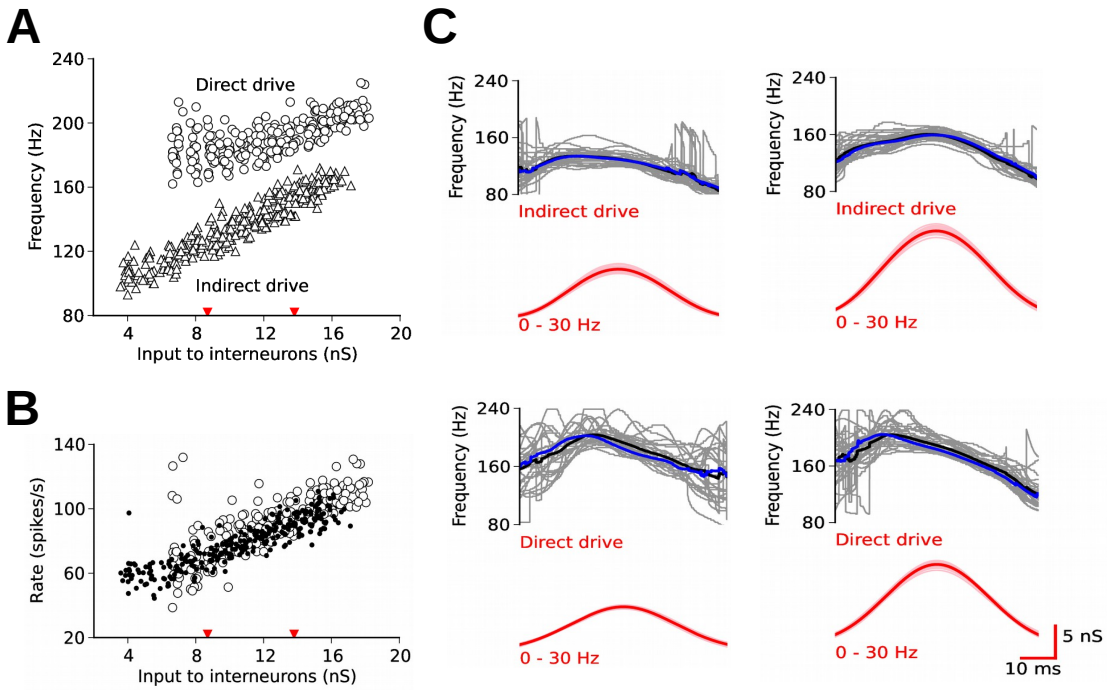

Fig. 3.5: Network frequency response for indirect versus direct drive of interneurons. ***A***, Network frequency as a function of the peak input conductance to interneurons (conductance includes ~2 nS baseline). For indirect drive (triangles, 280 simulations), frequency increased linearly with peak input, covering the fast gamma range (90-140 Hz) and part of the lower ripple band. For direct drive (circles, 240 simulations), frequency was more stable and limited to the ripple band (140-220 Hz). ***B***, Firing rate of interneurons as a function of the peak input to interneurons. Units expressed similar firing rates in both direct (open circles, range: 39 to 132 spikes/s) and indirect (black dots, range: 44 to 111 spikes/s) conditions. ***C***, Instantaneous frequency of single events (gray traces, 30 simulations) and corresponding low-pass filtered excitatory input to interneurons (red traces) for indirect (top) and direct (bottom) drive conditions at the input levels indicated in *A* and *B* (red inverted triangles, left and right, respectively). Red and black solid lines correspond to conductance peak-triggered averages. Blue solid lines are power peak-triggered averages. During the indirect drive condition, IFA signature is disrupted at high input levels.

For the direct-drive condition, I tested a range of peak conductances spanning from 6.5 nS (the minimum required to evoke oscillations under this condition) to 18 nS. Oscillations evoked in the direct-drive condition exhibited frequencies constrained to the ripple band (range: 162 to 225 Hz, circles in Fig. 3.5*A*). Frequencies were also only weakly sensitive to the peak excitatory input delivered (see also Fig. 2.2*D*).

The mean firing rates of interneurons evoked in the two conditions were remarkably similar (Fig. 3.5*B*). Within the range of inputs tested, interneurons expressed firing rates

around the value exhibited by PV^+BC during SWR in awake mice (∼75 spikes/s; Varga et al., 2012).

These results indicate that, within the range of inputs tested, the network operated at a higher saturation level in the indirect-drive condition. If we consider the ratios of unit firing rate to their corresponding network frequencies for that condition (dots and triangles in Fig. 3.5*B* and *A*, respectively), we can estimate a saturation of ∼60% for the entire range tested. Consistent with such level of saturation, the interneuron network frequency increases with excitatory input (see also Fig. 2.2*D*).

In the direct-drive condition, on the other hand, network frequencies were higher with respect to the unit firing rates (circles in Fig. 3.5*A* and *B*, respectively), yielding saturation levels ranging from 30 to 50%. Consistently, network frequency became gradually more sensitive to input at higher input levels (see also Fig. 2.2*D*).

3.3.5 Frequency dynamics under indirect versus direct drive

So far, I have focused on the overall frequency of single events in relation to the average firing rate of interneurons. I have shown that different frequency-ranges are expressed depending on the driving condition and the peak excitation provided. Now I switch the focus to the instantaneous frequency within single events and analyze how IFA is expressed at two different levels of excitation under both the indirect and direct-drive conditions (Fig. 3.5*C*).

For the indirect-drive condition, I tested the same levels of input used in Figure 3.4*B*. Such levels (red triangles in Fig. 3.5*A* and *B*) evoked frequencies in the fast gamma (∼120 Hz) and lower ripple (∼150 Hz) bands, respectively . At the low input level, the instantaneous frequency of single events displayed a shallow IFA (gray traces in Fig. 3.5*C*, top-left), similar to that observed in awake mice (Hulse et al., 2016). The frequency peak of the the average instantaneous frequency (black trace) occurred 12.3 ms before the peak of excitation (red trace). At the high input level, however, the IFA signature was disrupted (gray traces in Fig. 3.5*C*, top-right): The frequency exhibited a peak only 2.4 ms before the time of maximum excitation.

The alteration of IFA signatures at higher input levels can be explained by the observed levels of network saturation (see also Fig. 2.2*D*). In the case of low input, the smaller excursion of the excitatory drive still allowed the development of an initially less saturated state that was followed by sharper synchrony (e.g., Fig. 3.4*B*, black trace on left; see also Fig. 3.2*C*). At higher input levels, on the other hand, the network operated in a highly saturated state throughout the entire event (e.g., Fig. 3.4*B*, black trace on right). As a consequence, the instantaneous network frequency tended to follow the time course of the excitatory drive disrupting the stereotypical IFA signature.

When the same input levels were directly applied to the interneurons, both instantaneous frequency traces displayed the IFA signature (Fig. 3.5*C*, bottom). For low and high input, the average instantaneous frequency traces exhibited peaks at 8.3 ms and 13.2 ms before the excitation peak, respectively.

3.4 Discussion

In this chapter I analyzed and compared the transient responses of two basic network motifs in CA1: First, a directly excited interneuron network where interneurons cannot provide inhibitory feedback to the pyramids driving them (Figs. 3.2*A* and 3.4*C*). Second, a closed loop

of pyramidal and interneuron networks (both recurrently connected) in which interneurons were driven by depolarization of local pyramids (Fig. 3.4*A* and*B*). In both cases, I explored a range of excitation levels that evoked firing rates of interneurons within the physiological range observed *in vivo* (Varga et al., 2012; Lapray et al., 2012; Katona et al., 2014).

The directly driven interneuron network generated responses with frequencies constrained to the ripple range (Figs. 3.2*E* and 3.5*A*). The responses also displayed a prominent IFA signature that remained at all input levels tested (Figs. 3.2*D*, 3.4*D*, and 3.5*C*).

In contrast, when the network was driven by local depolarization of pyramids, the responses exhibited frequencies predominantly in the fast-gamma range and the lower part of the ripple band (Fig. 3.5*A*). Interestingly, the responses displayed IFA signatures only in the fast-gamma band (Figs. 3.4*B* and 3.5*C*).

3.4.1 Fast-gamma and ripples are mediated by different network motifs

The two scenarios I analyzed here have been presented in the literature as alternative models for transient hippocampal oscillations (Fig. 3.6*A*). Stark et al. (2014) argued that the indirect-drive condition provides a better description of both fast-gamma and ripple events *in vivo*. This view is at odds with the present results: Here I showed that in the indirect-drive condition, transient oscillations can indeed be evoked in the ripple range, provided pyramids were sufficiently depolarized (Fig. 3.5*A*). However, the higher saturation of the indirectly driven interneuronal network disrupted the IFA signature in the ripple range (Fig. 3.5*C*, top right). If we now consider the fact that both ripple and fast gamma events exhibit IFA (Fig. 3.1*C*), it is unlikely that both types of oscillations are solely mediated by indirect drive of interneurons, as suggested by Stark et al. (2014).

In conclusion, the results presented here support the idea that transient oscillations in the ripple (140–220 Hz) and fast-gamma (90–140 Hz) ranges are mediated by different network motifs. Oscillations in the ripple range are better described by a situation in which the interneuronal network provides little or no inhibitory feedback to the population of pyramids driving the interneurons (as in Fig. 3.6*A*, left). Oscillations in the fast-gamma range, on the other hand, are better described by a closed-loop scenario in which the interneuronal network can provide strong inhibitory feedback to the pyramids driving the interneurons (as in Fig. 3.6*A*, right).

In the following, I discuss the connectivity substrates within CA1 that could favor either the direct drive or indirect drive of the PV^+BC interneuronal network.

3.4.2 Hippocampal substrates supporting fast-gamma and ripples

Differences in the local connectivity between pyramidal cell and PV^+BC suggest that both motifs depicted in Figure 3.6*A* could be present in CA1. Such connectivity pattern allow us to identify putative excitatory pathways in the projections to CA1 that would favor the emergence of either fast gamma or ripples (Fig. 3.6*B*).

Network motifs in CA1. When testing the indirect-drive condition, I adopted a scheme of connectivity between pyramids and interneurons that was strongly dominated by feedback inhibition (Fig. 3.4*A*); both connection probabilities and synaptic strengths of the inhibitory projections to local pyramids were three times stronger than those used to connect local pyramids to interneurons (for details, see Methods at the end of the chapter). In CA1, however, two subgroups of pyramidal cells are differentially interconnected with PV^+BC

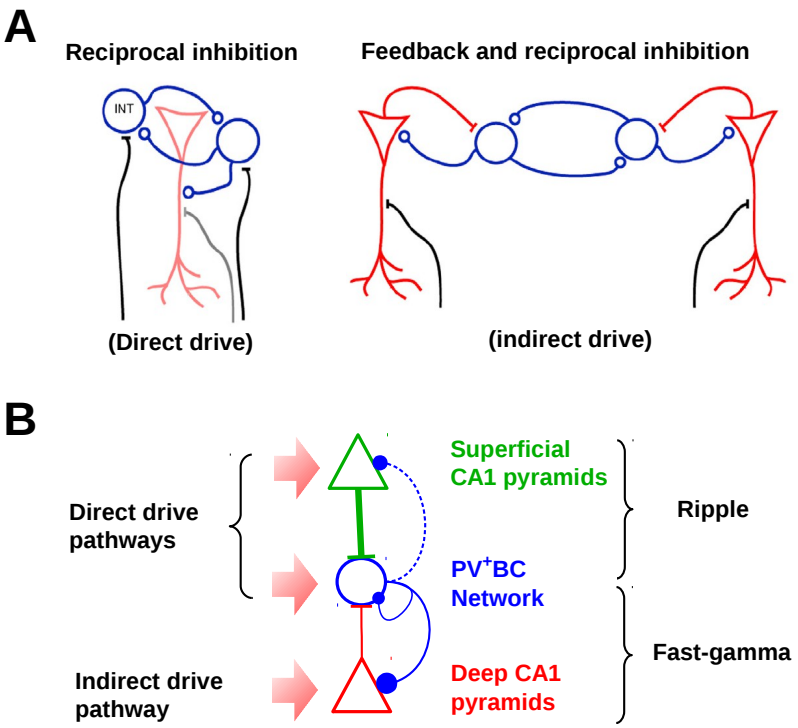

Fig. 3.6: Network models for transient oscillations in CA1. ***A***, Two alternative models as suggested by Stark et al. (2014). The corresponding driving conditions tested here are shown in parenthesis (bottom). *Left*: Oscillations are generated by reciprocal inhibition, and pyramids (possibly receiving external input; gray) are paced by the interneuronal network. *Right*: Pyramidal cells receive tonic external input (black). Activated pyramids provide excitation to the reciprocally connected inhibitory network which, in turn, paces the excited pyramidal cells and generate the LFP ripple (Stark et al., 2014; reproduced with permission from Elsevier). ***B***, Model proposed here. Differential connectivity between pyramids (triangles) and PV^+BCs (circles) in CA1 suggest different excitatory pathways that could favor direct or indirect drive of interneurons. Superficial pyramids (green) provide three times more projections (straight lines) to PV^+BCs than those in the deep layers (red). Deep pyramids receive three times stronger PV^+BCs mediated inhibition than their superficial counterparts. Red arrows indicate putative pathways that would favor the emergence of ripple or fast-gamma oscillations in CA1.

(Lee et al., 2014; Fig. 3.6*B*; see also section 1.4.3). Pyramidal cells located in the deep layers of *str. pyramidale* (i.e., closer to *str. oriens*) are interconnected with PV^+BCs in a scheme that is dominated by feedback inhibition (as in the indirect drive condition here). Conversely, pyramidal cells located in the superficial layer of *str. pyramidale* (i.e., closer to *str. radiatum*), project heavily on PV^+BC and receive comparably little inhibition from them (a scheme more reminiscent of the direct-drive condition).

Putative excitatory pathways to interneurons. In general, excitatory projections to CA1 can target both pyramids and interneurons (Amaral and Witter, 1989; Wouterlood et al., 1990; Takács et al., 2012). If we now consider the local connectivity discussed above, one could distinguish two excitatory pathways driving the PV^+BC network (arrows in Fig. 3.6*B*): (1) an indirect pathway mediated by pyramids in the deep layers (bottom arrow; see also Fig. 3.4*A*), and (2) a direct pathway mediated by superficial pyramids (top arrow) and by direct projections to interneurons (middle arrow; see also Fig. 3.2*A*).

The possibility of superficial pyramids mediating a direct excitatory pathway will depend on whether they can be effectively driven by the excitatory afferents without strong involvement of feedforward and feedback inhibition. A study that investigated the differential intracellular dynamics of superficial and deep pyramidal cells during SWRs *in vivo* provides some light on this issue with respect to the projections from the CA3 area (Valero et al., 2015). They showed that superficial pyramids exhibit a systematic net depolarization at the SW peak recorded in the *stratum radiatum*. Interestingly, the amplitudes of those depolarizations were strongly correlated with the SW sink in the radiatum, suggesting an intracellular dynamics dominated by Schaffer collateral input. Furthermore, stimulation of CA3 and pharmacological interventions confirmed that the intracellular responses of superficial pyramids were dominated by feedforward excitation. Taken together, these results open the possibility of superficial pyramidal cells mediating a direct excitatory pathway to interneurons (top arrow in Fig. 3.6).

In summary, considering the excitatory projections to CA1 pyramids and the differential connectivity between pyramids and interneurons in CA1, I hypothesize the existence of two putative excitatory pathways that would favor ripples and fast gamma, respectively (Fig. 3.6*B*, top and bottom arrows). The Schaffer collateral afferents to interneurons would constitute an additional direct pathway that would favor the expression of ripple oscillations in CA1 (Fig. 3.6*B*, middle arrow).

3.4.3 Mechanisms governing pathway dominance

The bimodal frequency distribution exhibited by transient oscillations in CA1 (Fig.3.1*B*) suggests the operation of some mechanism in the network that favors the expression of either fast-gamma or ripples. In light of the model depicted in Figure 3.6*B*, it could be hypothesized that the expression of fast-gamma or ripples will be determined by the excitatory pathway to interneurons that is favored in any given event (red arrows). Which factors would determine the predominance of one or the other pathway? Here I briefly discuss two possibilities, (1) local inhibitory interactions within CA1, and (2) specificity of CA3 afferents to superficial and deep pyramids.

Local network balance. The simple scheme depicted in Figure 3.6*B* resembles a winner-take-all network tilted in favor of the expression of ripples. The strong bias of the feedback

inhibition towards the deep pyramids suggests that the recruitment of any of the direct pathways would shunt the simultaneous recruitment of the indirect pathway. It follows that the expression of ripple oscillations would inhibit the expression of fast-gamma. Conversely, the weaker projections from deep pyramids to interneurons, and from interneurons to superficial pyramids, makes it difficult for the indirect pathway to hinder the recruitment of the direct pathway. Moreover, as shown here, the recruitment of the indirect pathway requires considerably stronger drive because the excitatory input needs to overcome the feedback inhibition for oscillations to ensue. Thus, the expression of fast gamma would require not only strong depolarization of deep pyramids but also a weak recruitment of any of the direct pathways to interneurons.

Specificity of excitatory afferents. As discussed above, the relative contribution of the excitatory input to deep pyramids with respect to superficial pyramids can modulate the predominance of one pathway over the other. If we allow the possibility that the excitatory afferents of deep and superficial pyramids emerge preferentially from different regions, then the origin of the excitatory input could determine the expression of ripples or fast gamma. For example, it has been suggested that CA3 pyramids located at different septotemporal or proximodistal hippocampal levels might preferentially project to deep or superficial CA1 pyramids (for an extensive discussion on this possibility, please refer to Slomianka et al., 2011). Other projections to CA1 such as those from the entorhinal cortex arriving via the temporoammonic pathway (Amaral and Witter, 1989) or from the nucleus reuniens of the thalamus (Wouterlood et al., 1990) could also preferentially target either deep or superficial pyramids and therefore favor the expression of fast gamma or ripples (see Outlook for further predictions in this direction).

3.4.4 Disruption of fast gamma *in vitro*

Why is fast-gamma selectively disrupted *in vitro*? As discussed above, the expression of oscillations in the fast-gamma range might require strong depolarization of deep pyramids; for oscillations to ensue, the excitatory input needs to overcome not only the strong feedback inhibition but also the feedforward inhibition that might be triggered by concomitant activation of the direct pathways. Delivering such a strong drive to deep pyramids might require a large convergence of afferents that only the *in vivo* conditions can provide.

In the intact hippocampus, CA1 pyramids receive input stemming from a large fraction of the hippocampal and entorhinal septotemporal extension (Ishizuka et al., 1990; Li et al., 1994; Naber et al., 2001). This means that, in addition to the extrahippocampal inputs, an important fraction of the afferents to CA1 pyramids would be compromised during the slicing process. The remaining afferents might be insufficient to recruit the indirect pathways but sufficient to drive the more excitable direct pathways, granting the expression of oscillations in the ripple band only.

3.4.5 Sharp-wave ripples in CA1 mini-slices

SWRs can also be observed in the isolated CA1 area (Maier et al., 2003, 2011). Could the model depicted in Figure 3.6 generate SWRs in the absence of excitatory input? Here, I have studied the response of the putative interneuronal network to different forms of externally applied excitatory bursts. Although the generation of such bursts themselves is out of the scope of the present study, I speculate that the activity of reciprocally connected superficial

pyramids could also self organize into transient bursts (de la Prida et al., 2006). Thus, a putative network of superficial pyramids would serve as an excitable network that directly drives the PV^+BC network, evoking transient oscillations in the ripple band. The plausibility of such scenario is a matter of further theoretical research.

In conclusion, the present results support the idea that oscillations evoked by depolarization of local pyramids provide a better description of transient events in the fast-gamma range. On the other hand, oscillations in the ripple range, particularly those evoked *in vitro*, are better described by a scenario in which the interneuron-network dominates.

3.5 Methods

Here I describe in more detail the extension of the interneuronal network model introduced in the previous chapter.

3.5.1 Extension of the network

Pyramidal neurons. Each pyramid is described by a single-compartment, leaky integrate-and-fire model (eq. 2.1). The leak (resting) membrane potential was $E_{\text{rest}} = -67$ mV. The capacitance $C_{\text{m}} = 275$ pF and the leak conductance $g_{\text{leak}} = 25$ nS yield a membrane time constant of 11 ms. The firing threshold was $V_{\text{thres}} = -50$ mV. After spiking, V_{m} is reset to the potential $V_{\text{reset}} = -60$ mV and the cell remains refractory for 2 ms. All values were adjusted according to Bähner et al. (2011).

Model synapses. The total synaptic current I_{syn} is described according to a conductance-based model

$$I_{\text{syn}} = (g_{\text{e}} + g_{\text{chr}})(E_{\text{e}} - V_{\text{m}}) + g_{\text{i}}(E_{\text{i}} - V_{\text{m}}) \tag{3.1}$$

where g_{e} and g_{i} are the instantaneous excitatory and inhibitory conductances, respectively resulting from the presynaptic activity. g_{chr} corresponds to an excitatory conductance that could be externally driven, aimed at mimmicking channelrhodopsins. The reversal potential E_{i} of inhibition (chloride) was set to -68 mV (Bähner et al., 2011; Maier et al., 2003). The reversal potential E_{e} of excitatory synapses was set to 0 mV.

The time course of a single postsynaptic potential is described by a normalized dual exponential (eq. 2.3). Pyramids were equipped with both GABAergic and AMPA-type synapses. For AMPA-type synapses, I used $\tau_r = 0.5$ ms, $\tau_{\text{d}} = 1.8$ ms, and $g^{\text{peak}} = 0.9$ nS (Maier et al., 2011). The values for GABAergic synapses were tuned according to (Bartos et al., 2002): $\tau_{\text{r}} = 0.4$ ms, $\tau_{\text{d}} = 2$ ms, and $g^{\text{peak}} = 9$ nS.

Interneurons were also equipped with AMPA-type synapses and channelrhodopsin-like synapses (for the direct- drive condition only). For AMPA-type synapses on interneurons, I used $\tau_r = 0.5$ ms, $\tau_{\text{d}} = 1.2$ ms, and $g^{\text{peak}} = 3.0$ nS (Pawelzik et al., 2002). GABA-type synapses on interneurons had $\tau_r = 0.45$ ms, $\tau_{\text{d}} = 1.2$ ms, and $g^{\text{peak}} = 5.0$ nS, as described in the previous chapter.

CA1 Network. An estimate for the number of pyramids was obtained by scaling the total number of 311,500 pyramids in CA1 (Bezaire and Soltesz, 2013) by the fraction of the volume of a 400-μm slice. If we approximate the geometry of the hippocampus to a cylinder and consider its septotemporal extension to be $\sim$10 mm (Patel et al., 2012), a 400-μm slice

represents 4% of the total volume. This fraction yields 12,460 pyramids in a slice. The number of pyramids was set to 12,000.

Pyramids were randomly connected to the interneurons with a probability $p_c = 0.1$ (Pawelzik et al., 2002). The interneurons, in turn, were connected back to the pyramids with probability $p_c = 0.3$ (Pawelzik et al., 2002). Pyramids were also reciprocally and sparsely interconnected with probability $p_c = 0.01$ (Deuchars and Thomson, 1996).

3.5.2 Transient stimulation

CA3 burst. To emulate CA3 projections to the interneuron network, a driving population of pyramids was randomly connected to the interneurons as described in the previous chapter. To simulate excitatory input during SWRs (Fig. 3.2), the interneuron network was excited with a transient burst of activity in the presence of an ongoing background. It is known that a small fraction of the pyramidal cells in CA3 ($\sim 17\%$) fires once during a single SWR event (Hájos et al., 2013). Accordingly, in my simulations, 1,400 out of 8,200 units of the driving population participated in the SWR. Each driving unit in this bursting subpopulation fires once at a time drawn from a normal distribution with a standard deviation of 5, 7, or 10 ms. The remaining driving units fire randomly at a rate of 1.85 spikes/s. The entire driving population was connected to the interneuron network with $p_{\text{share}} = 0.095$. Thus, for each interneuron, 133 synapses provided a strong transient input burst and the remaining synapses provided a weak Poissonian background activity at a total rate of 1,200 spikes/s.

Indirect drive (stimulation on local pyramids). For the indirect drive condition, a random subpopulation of 100 local pyramids was depolarized by driving their tonic excitatory conductances with Gaussian intensity profiles ($\sigma = 13$ ms). The amplitudes of such profiles were normally distributed across the population with a variability described by the ratio between the standard deviation and the mean of the normal distribution (i.e., by its coefficient of variation, CV). The variability was kept constant at $CV = 0.5$ across simulations, only the mean amplitude of this distribution was varied to provide different levels of input to the pyramids.

Direct drive (stimulation on interneurons). Interneurons were depolarized by driving their tonic excitatory conductances with Gaussian intensity profiles, as was done with pyramids. Such intensity profiles were adjusted according to the excitatory activity measured on interneurons during the indirect-drive condition. For every average level of input applied to the pyramids during indirect-drive, the resulting excitatory conductances measured at the interneurons were low-pass filtered (<30 Hz) to generate a sample of 200 reference conductance traces (one for each interneuron). From that sample, an average trace and its standard deviation was measured. The average trace and variability obtained were then used to adjust the Gaussian intensity profiles that were delivered directly to the interneurons via their tonic excitatory conductances.

3.5.3 Analysis of network activity

For simulations performed under transient stimulation, I calculated the wavelet spectrogram of the corresponding transient response (for example Fig. 3.2*B*, top). To obtain this spectrogram, the population spiking activity was first smoothed with a Gaussian kernel ($\sigma = 0.2$ ms),

i.e. each spike was replaced by a Gaussian, and then convolved with Gabor wavelets covering the band 120–270 Hz in steps of 1 Hz.

To reveal the time course of the instantaneous frequency of single ripple events, I located the maximum activation at every time step in the spectrogram (Fig. 3.2*D*). Likewise, the time course of the power was calculated by averaging the wavelet spectrogram across frequencies for every time step (Fig. 3.2*F*). The duration of a transient response was calculated as the length of the time interval during which the power exceeded 4 standard deviations above the baseline mean, which corresponds to the power generated by the response of the network to the background input activity. The power spectrum was calculated by averaging the wavelet spectrogram across time for each frequency (Fig. 3.2*E*). The leading frequency was obtained from the peak of the power spectrum. The unit firing rate was calculated by dividing the number of spikes the interneurons generated during an event by the duration of the transient response.

4 Frequency dynamics during spontaneous events *in vitro*

Oscillations evoked in transiently excited interneuron networks in silico exhibit intra-ripple frequency accommodation (IFA). Depending on whether interneurons are driven directly, or by depolarization of the local pyramids to which they project, IFA is expressed in the ripple (140–220 Hz) or fast-gamma (90–140 Hz) bands, respectively. Regardless of the driving pathway, the model predicts that the IFA signature displays a peak during the ascending phase of the excitatory drive. Here, I use data from whole-cell recordings during spontaneous events in vitro to characterize the instantaneous frequency of the CA1 inhibitory output in relation to its excitatory input. I show that (1) inhibition displays a prominent IFA signature, predominantly within the ripple range (140–220 Hz), and (2) that IFA exhibits a peak during the ascending phase of the excitatory drive, as predicted by the in silico model. These results support the idea that the frequency dynamics during spontaneous oscillations in vitro is well described by a directly driven interneuronal network.[1]

4.1 Frequency dynamics *in silico*

In the previous chapter, I resorted to an *in silico* model to show that an interneuronal network that is driven by a burst of excitatory activity can exhibit intra-ripple frequency accommodation (IFA) in its transient response (Fig. 3.5*C*, bottom). When the interneuronal network is directly driven, the frequency of such responses is constrained to the ripple band (140–220 Hz). On the other hand, when interneurons are driven by the local pyramids to which they project, the IFA signature can only be observed in the fast-gamma (90–140 Hz) band (Fig. 3.5*C*, top).

Regardless of the way the interneurons are driven, the *in silico* model predicts a peculiar relationship between the time courses of the instantaneous frequency and the transient excitatory input to interneurons: the network frequency exhibits a peak during the ascending phase of the excitatory drive (Fig. 3.2*B*, top, and Fig. 3.4*D*).

Here, I characterize the instantaneous frequency of the inhibitory output of the CA1 network during spontaneous events recorded *in vitro*. In particular, I aim at testing whether IFA can be readily observed under *in vitro* conditions and whether its predicted relationship with the time course of excitation is met.

4.2 Probing the CA1 network *in vitro*

To test the predictions of the *in silico* model, we resorted to a previously established *in vitro* model of hippocampal SWRs in CA1 (Maier et al., 2009). In this preparation, we

[1] The research presented in this chapter was performed in collaboration with Nikolaus Maier, Dietmar Schmitz and Richard Kempter. I developed the analysis tools, performed the analysis of the experimental data and participated in the design of the experiments. The data was recorded by Nikolaus Maier.

aimed at tracking the instantaneous frequency of the putative interneuronal network activity while simultaneously observing the time course of the excitatory input to CA1 during SWR events. In other words, we were specifically interested in the fine temporal 'ripple' structure of inhibition and the slower temporal 'sharp wave' structure of excitation. This information can be extracted from whole-cell recording of pyramidal cells in voltage-clamp mode. However, inhibitory and excitatory currents cannot be measured simultaneously in a single cell. Hence, we performed simultaneous patch-clamp recordings from two neighboring pyramidal cells within area CA1 (for details, see Methods at the end of this chapter). By isolating excitatory synaptic activity in one cell and inhibitory synaptic activity in another, we could extract the relevant information to test the model prediction.

The described approach rests on the assumption that the currents in two different pyramidal cells are correlated. This assumption is supported by the structure of the projections: pyramidal cells receive input from a large sample of converging inhibitory (mostly local collaterals) and excitatory (mostly Schaffer collaterals) fibers (Takács et al., 2012). Therefore, the synaptic current measured in a single cell can provide information about the overall activity of the respective converging population. To test this assumption, we first voltage-clamped pairs of pyramidal cells at the same holding potential and assessed the temporal relationship between the measured currents. Clamping both cells at the reversal potential of inhibition reveals excitatory currents. On the other hand, clamping both cells at the reversal potential of excitation reveals inhibitory currents. We first investigated these two cases in detail and checked whether inputs were indeed correlated.

4.2.1 Phase-alignment of inhibitory ripples in pairs of pyramidal cells

Can the inhibitory current measured in one CA1 pyramidal cell provide information about the inhibitory current in another pyramidal cell? We reasoned that if a pair of pyramids receives input from two inhibitory subpopulations that are entrained by a common rhythm (i.e., a ripple), the ripple-locked compound IPSCs (cIPSCs) recorded in the two cells should be temporally aligned or, equivalently, their ripple components should be phase-locked with a phase difference close to 0. Therefore, we analyzed the phase relationship between inhibitory ripples (Fig. 4.1).

To isolate inhibitory currents, two simultaneously recorded cells were clamped at the reversal potential of excitation. In both cells, we observed cIPSCs that co-occurred with the extracellularly recorded SWRs (Fig. 4.1*A*) and exhibited a temporal structure consistent with a rhythmic inhibitory input (Fig. 4.1*A*, bottom). For every SWR event, two inhibitory ripples were obtained from band-pass filtered currents (120–300 Hz). We then calculated the Hilbert transform of the two ripples and obtained their envelopes (Fig. 4.1*B*, top) and instantaneous phase angles. The instantaneous phase shift between the two ripple oscillations was obtained by subtracting the angles yielded by their respective Hilbert transforms (Fig. 4.1*B*, bottom). Then the phase shift of a single SWR event was calculated as the circular mean of the instantaneous phase shift in the time interval where both ripple envelopes exceeded three standard deviations of the baseline (Fig. 4.1*B*, gray box); and the quality of phase locking was described by the vector strength of the instantaneous phase shift during this overlap. The phase shift, which is an angle, and the vector strength, which is a number between 0 and 1, were determined for all SWR events recorded in a cell pair (Fig. 4.1*C*, gray circles). From all these phase vectors obtained in a simultaneous recording, we calculated an average phase vector (Fig. 4.1*C*, black circle). Inhibitory ripples were strongly phase locked at low phase-shift angles in all simultaneous recordings analyzed (Fig. 4.1*D*). For the seven recordings

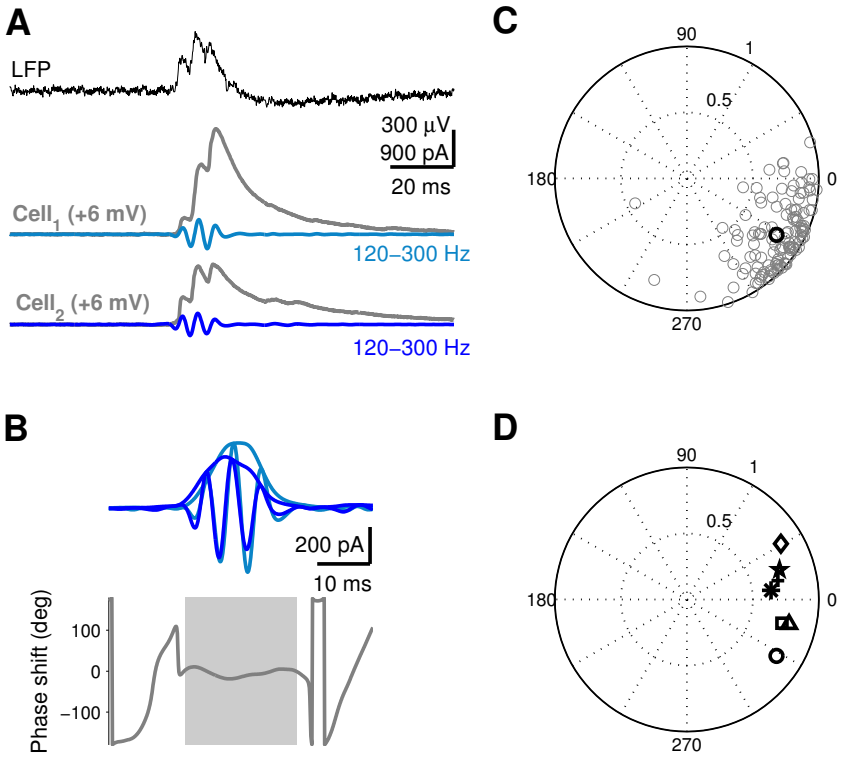

Fig. 4.1: Inhibitory currents are phase-locked in pairs of CA1 pyramidal cells during SWRs *in vitro*. ***A***, To isolate inhibitory currents, two cells were clamped at +6 mV. Top trace (black): extracellular SWR. Bottom traces: simultaneously recorded inhibitory currents (grey) and band-pass filtered versions (as indicated, blue). ***B***, Magnification and overlay of the two filtered currents and their envelopes as derived from the Hilbert transform (top). The instantaneous phase shift (bottom, gray trace) between the two ripple oscillations was obtained by subtracting the angles yielded by their respective Hilbert transforms. The average phase shift (−4 degrees) and the quality of phase locking (vector strength 0.99) was estimated from the time span where both envelopes exceed 3 std of baseline (gray box). ***C***, Average phase shifts and vector strengths of inhibitory currents for 124 SWR events (grey circles) recorded in one cell pair. The black circle indicates the average phase vector (phase shift: −32 degrees, vector strength: 0.81) across events. ***D***, Average phase vectors for 7 cell pairs (symbols).

analyzed, the average vector strength was 0.76 ± 0.03 (range: from 0.63 to 0.82) and the average phase shift was 2 ± 8 deg (range: from -32 to $+31$ deg). The range of phase-shifts observed corresponds to time lags lower than 0.5 ms for a ripple frequency of 200 Hz. These results indicate that the inhibitory current measured in one pyramidal cell can be used to assess the phase of the putative interneuron network activity and therefore its instantaneous frequency.

4.2.2 Alignment of excitatory sharp-waves in pairs of pyramidal cells

In a second set of experiments, we aimed at testing whether the time course of the excitatory current recorded in one pyramidal cell is a reliable predictor of the overall time course of excitatory input to the network. We reasoned that if a pyramidal cell receives input from a large sample of Schaffer collateral fibers, we should be able to use the excitatory current recorded in any pyramid to track the time course of the excitatory burst. We specifically tested whether the slow component of excitation is aligned in pairs of pyramidal cells (Fig. 4.2).

To isolate excitatory currents, two simultaneously recorded cells were clamped at the reversal potential of inhibition. In both cells, we observed ripple-locked compound EPSCs (cEPSCs) that co-occurred with the extracellularly recorded SWRs (Fig. 4.2*A*) (Maier et al., 2011). To keep track of the coarse excitatory input, we focused on the low-frequency components of the measured currents. For every SWR, we obtained a low-pass filtered version (0–50 Hz) of the co-occurring SWR-locked cEPSCs. The rectified version of such a slow current describes the time course of the excitatory input that we refer to as 'excitatory sharp wave' (eSW, Fig. 4.2*B*, top). To be able to precisely characterize the time course of an eSW, we calculated its first derivative. This allowed us to reduce the eSW to a single cycle in which a positive part marks the ascending phase of the eSW, the zero crossing demarcates the peak, and the subsequent negative part marks the descending phase (Fig. **??***B*, middle). The relative timing of the two simultaneously recorded eSWs can be described by their cross-correlation. The lag of the peak of the cross-correlation quantifies the time lag between the signals, and the peak value determines the amount of correlation (Fig. 4.2*B*, bottom). Figure 4.2*C* shows the peak correlations and the time lags of eSWs obtained for all the events recorded in one pair of cells (gray dots). From all the events in one recording, we calculated the average time lag and the average correlation coefficient (black circle). Figure 4.2*D* shows the average time lag and the average correlation values in seven cell pairs. In all of these recordings, high values of correlation coefficients (range: 0.66 to 0.92) and low time lags (range: -2.9 to $+1.4$ ms) were observed. High correlation values between pairs of cells imply that the time course of excitation recorded in one cell is a reliable predictor of the excitatory input experienced by other cells in the network. From these results we concluded that it is possible to use the excitatory synaptic input into a single pyramid to assess the phase of the excitatory burst driving the CA1 network.

4.3 Intra-ripple frequency accommodation and its relation to the time course of excitation.

Having confirmed our main assumptions on the correlation of SWR-associated currents in pairs of pyramids, we could use one pyramidal cell (of a pair) to probe the output of the inhibitory CA1 network while simultaneously using another pyramidal cell to probe the ex-

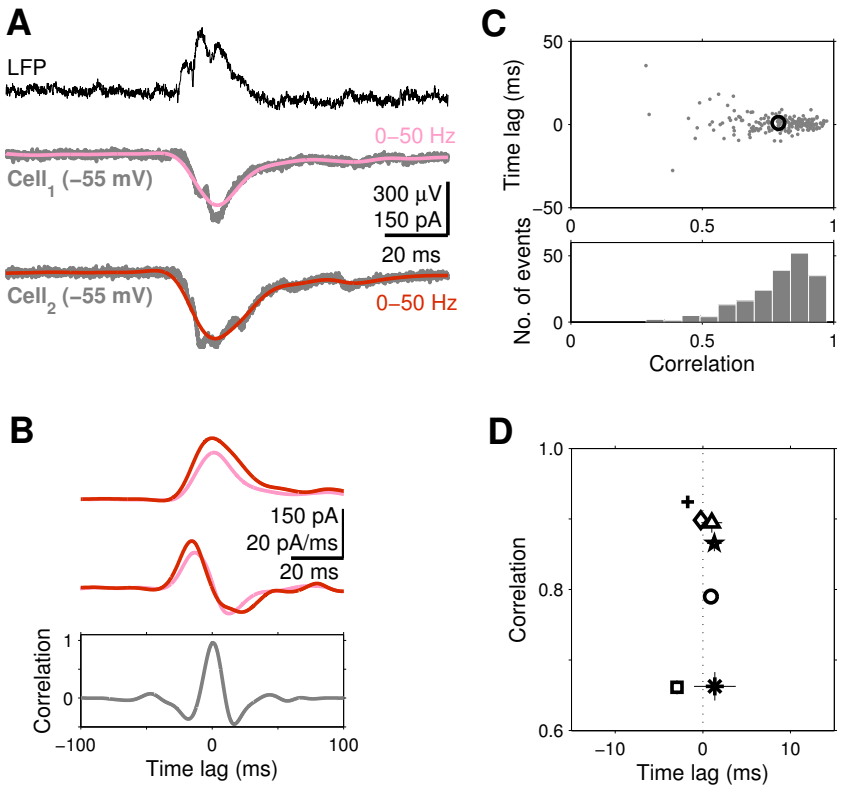

Fig. 4.2: Excitatory currents are temporally aligned in pairs of CA1 pyramidal cells during SWRs *in vitro*. ***A***, To isolate excitatory currents, two cells were clamped at −55 mV. Top trace (black): extracellular SWR. Bottom traces: simultaneously recorded excitatory currents (grey) and low-pass filtered versions (as indicated, red). ***B***, Overlay of the two filtered and rectified currents (top), their temporal derivatives (middle), and the crosscorrelation of the derivatives (bottom). The maximum of the crosscorrelation (0.97) indicates the strength of the correlation, and the time of this peak (0.7 ms) denotes the time lag of the two excitations for a particular SWR. ***C***, Time lags as a function of the maximum correlation (top, grey dots) and histogram of maximum correlations (bottom) for 191 events (grey dots) recorded in one cell pair. The black circle indicates the average correlation (0.79 ± 0.01) and the average time lag (0.9 ± 0.5 ms) across events. ***D***, Average time lag versus average correlation for 7 cell pairs. The grand average time lag (across cell pairs) was -0.04 ± 0.54 ms (range: from −2.9 to 1.4 ms).

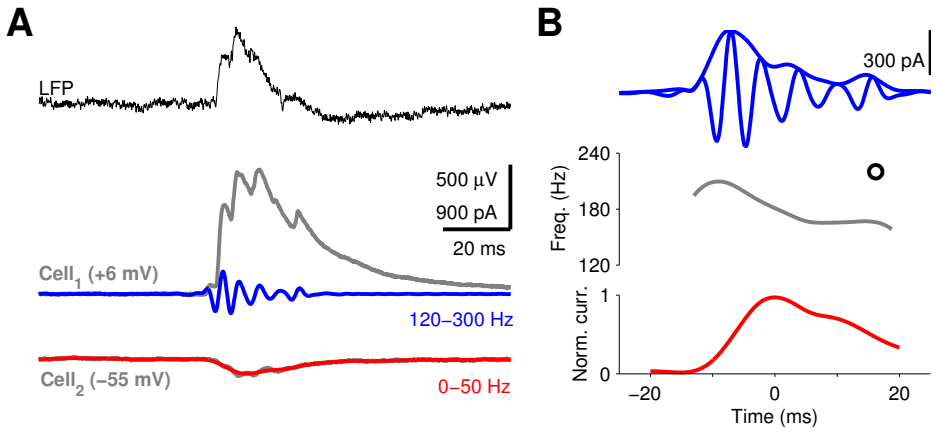

Fig. 4.3: Instantaneous frequency of inhibition and its relation to the time course of excitation in CA1 pyramidal cells *in vitro*. ***A***, During a SWR in the LFP (top), the inhibitory current was recorded in cell 1 (middle) while the excitatory current was simultaneously recorded in cell 2 (bottom). ***B***, Illustration of the analysis of a single event. From the inhibitory ripple current obtained from cell 1 (top), the instantaneous frequency (middle) was calculated from its wavelet spectrogram. The frequency trace (middle) is plotted only for the time interval where the envelope of the ripple oscillation exceeds 3 std of the baseline (here from −6 to +20 ms). The simultaneously recorded, low-pass filtered signal that represents excitation (bottom) has a peak at a time at which the instantaneous frequency is decreasing. Here, the time is set relative to the peak of the excitatory input current.

citatory input to CA1. For every SWR recorded in the LFP, the inhibitory current was recorded in one cell by holding its membrane potential at the reversal potential of excitation. Simultaneously, the excitatory current was recorded in another cell by holding it at the reversal potential of inhibition (Fig. 4.3*A*). An inhibitory ripple and a coarse excitation were obtained from the band-pass (120–300 Hz) and low-pass (0–50 Hz) filtered versions of the respective currents. From the inhibitory ripple current obtained in one cell, the instantaneous frequency was calculated using the wavelet-spectrogram (Fig. 4.3*B*, top and middle). From the rectified coarse excitation we obtained an eSW. By combining the instantaneous frequency with the eSW (Fig. 4.3*B*, bottom), we were able to describe the temporal relationship between the instantaneous frequency of inhibition and the time course of excitatory input onto CA1 during a single SWR (Fig. 4.3*B*, middle and bottom).

The data was collected in a configuration-switching fashion: After having recorded some data under one configuration of holding potentials (i.e., cell 1 at +6 mV and cell 2 at −55 mV), the holding potentials were switched (i.e., cell 1 at −55 mV and cell 2 at +6 mV). This approach allowed us to control for any bias that might be introduced by the particular cells used.

Figure 4.4*A* shows the instantaneous ripple frequencies obtained from inhibitory currents and its relation with the time course of excitatory currents. We confirmed the prediction of the model in 6 out of 7 pairs: the instantaneous frequency peaked during the ascending phase of excitation and started to decay before the peak of excitation was reached. To characterize the typical time at which the frequency peaked with respect to the maximum excitation, we measured this interval in all 1972 recorded events across cells and conditions (Fig. 4.4*B*), obtaining an average delay of -6.2 ± 0.2 ms. We also obtained average times of the frequency peak for all events recorded in each cell pair (Fig. 4.4*C*). Pairs displayed

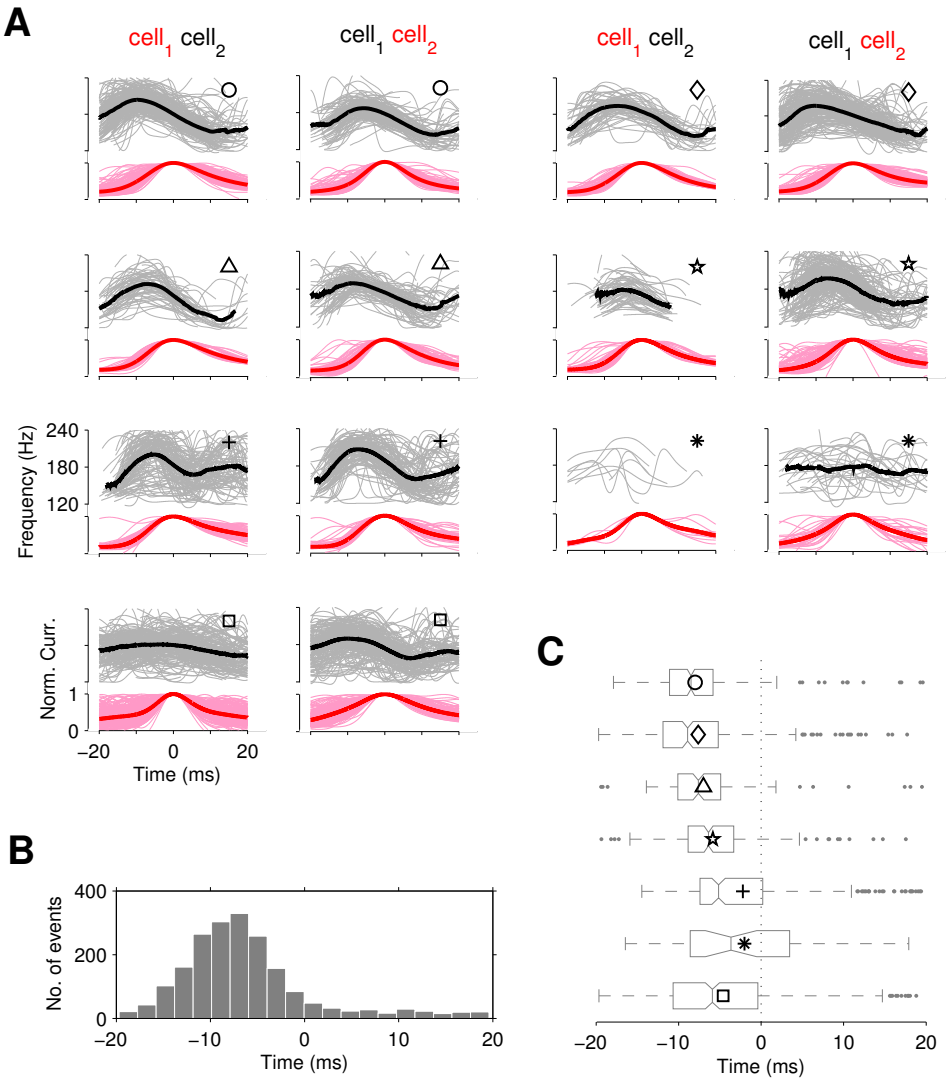

Fig. 4.4: Intraripple frequency accommodation and its relation to the time course of excitation in CA1 pyramidal cells *in vitro*. ***A***, Instantaneous ripple frequencies and time courses of excitatory currents for 7 cell pairs (symbols at top right corners matched to Fig. 9). For all cell pairs, we recorded in two conditions by switching the holding potentials (+6 and −55 mV) of the two cells. Each subplot shows an overlay of instantaneous frequencies (grey) and normalized excitations (pink) for all SWR events recorded in one recording condition for a cell pair. The average instantaneous frequency (black traces) is calculated only at times where at least 10 traces overlap. Average excitatory currents are shown in red. In 6 (out of 7) cell pairs, the average instantaneous ripple frequency has a peak before the mean excitation reaches its maximum. ***B***, Time of frequency peak for 1972 events recorded from 7 pairs. On average, the instantaneous ripple frequency has a peak 6.2±0.2 ms before the mean excitation reaches its maximum. ***C***, Time of frequency peak for all events recorded in each cell pair. Symbols mark the mean and identify the cell pair. Average time across cells pairs: -5.3 ± 0.9 ms (range: from −8.0 to −2.0 ms). In 6 (out of 7) cell pairs, at least 75% of events exhibit a frequency peak before excitation reaches its maximum.

times of frequency peaks ranging from −8.0 to −2.0 ms. The average peak-time across cell pairs was -5.3 ± 0.9 ms.

In the present section, I have shown that the instantaneous frequency of the inhibitory-network activity, as recorded in pyramidal cells, exhibited a peak during the ascending phase of the excitatory input. Such a finding would confirm the prediction of the *in silico* model only if the excitation recorded on pyramids can reliably estimate the time course of the excitatory input to interneurons with milisecond precision. In particular, the timing of the excitatory peak is critical. Here I discuss and provide evidence to discard a possible worst-case scenario that could introduce a large mismatch between the peaks of excitation recorded in pyramids and that experienced by interneurons.

So far, I assumed that most of the excitatory input recorded on pyramids corresponded to Schaffer collateral activity. However, the ripple component that can be observed in the excitatory currents (see gray traces in Fig. 4.2*A*) reveals the presence of entrained pyramidal cell activity, presumably of local origin (Maier et al., 2011). Another *in vitro* study that was performed in the same preparation used here revealed that such local activity of pyramids appears rather late during the SWR event (Bähner et al., 2011); the discharge probability profiles of pyramids and perisomatic targeting interneurons show that pyramids fire nearly 8 ms delayed with respect to interneurons.

Now, suppose that the interneurons are predominantly driven by Schaffer collateral activity and suppose that the excitatory input we measured on pyramids correspond to purely local, ripple-entrained pyramidal cell activity. In such a worst-case scenario, the peak of the excitatory input measured would occur considerable later than the actual peak experienced by interneurons. If the peak measured in pyramids is delayed with respect to the actual peak experienced by interneurons, the IFA traces and distributions depicted in Figure 4.4 would be shifted to later times with respect to excitation. A ∼6 ms shift would render the instantaneous frequency rather following the excitatory input, which could dramatically alter the conclusions.

To asses the likelihood of such a scenario I focused on the timing of excitation with respect to inhibition obtained from the same data used in Figures 4.3 and 4.4. I reasoned that if the measured excitation appears delayed with respect to inhibition, it might be indicative of a rather local origin of the excitatory input. Conversely, if the measured excitation leads inhibition, it might be indicative of excitation being the driving force of the interneuronal output.

To characterize the delay of excitation with respect to inhibition, I measured the peak time of the excitatory sharp-wave (eSW, red trace in Fig. 4.3*A*) with respect to the inhibitory sharp-wave (iSW). The iSW corresponded to the low-pass version (0–50 Hz) of the simultaneously recorded inhibitory current (gray trace in Fig. 4.3*A*, iSW not shown). Across all events measured in both holding potential configurations, excitation peak appeared on average 1.5 ± 0.2 ms before inhibition. Such a timing is consistent with a monosynaptic excitatory input followed by a disynaptic inhibitory response.

To summarize, *in vitro* experiments confirmed the model prediction that during SWRs the inhibitory oscillation frequency exhibits its peak during the ascending phase of the coarse excitatory input driving the putative interneuronal network.

4.4 Discussion

Here, I used data obtained from dual whole-cell on pyramidal cells to simultaneously probe the excitatory and inhibitory activities in the CA1 network during spontaneous SWR *in vitro*. Such data allowed me to characterize the instantaneous frequency of the CA1 inhibitory output in relation to its excitatory input. I showed that (1) oscillations in the inhibitory activity recorded in CA1 pyramids exhibit IFA within the ripple range, and (2) that the instantaneous frequency of such inhibition exhibits a peak during the ascending phase of the simultaneously recorded excitatory activity.

In light of the *in silico* model described in the previous chapter, the present results support the idea that the frequency dynamics during SWRs *in vitro* is better described by a directly driven interneuronal network (as in Fig. 3.6*A*, left). The *in silico* model predicted that in a closed loop scenario with strong involvement of pyramids (as in Fig. 3.6*A*, right) IFA could only be observed in the fast gamma-range but not at the high frequencies typically expressed *in vitro*. On the other hand, a directly driven interneuronal network could exhibit IFA only in the ripple range, as in the present results (Fig. 4.4*A*).

The idea of a directly driven interneuronal network is also consistent with the fact that SWRs *in vitro* are dominated by inhibition (Maier et al., 2003, 2011; Bähner et al., 2011). Events observed *in vitro* are not only characterized by frequencies limited to the ripple range (140–220 Hz) but also by extremely low firing rates of pyramids (e.g. 0.038 spikes/s; Bähner et al., 2011). From the perspective of the inhibition-first model, the strong rhythmic perisomatic inhibition allows only a very sparse but precisely timed firing of pyramidal cells. Such rhythmic excitatory activity is revealed as a ripple component in the excitation to pyramids (Maier et al., 2011) (see gray traces in Fig. 4.2).

Although precisely timed, the sparse activity of local pyramids observed *in vitro* might be insufficient to effectively close the loop between pyramids and interneurons. In contrast, *in vivo* pyramidal firing rates reach 40 spikes/s (English et al., 2014; Hulse et al., 2016). Such a strong involvement of pyramids evidences the recruitment of the pyramidal-interneuron loop, which favor oscillations in the fast-gamma band (Brunel and Wang, 2003; Brunel and Hakim, 2008).

In conclusion, the frequency dynamics of SWRs *in vitro* is better described by a directly driven interneuronal network, in which the closed-loop with pyramidal cells is not effectively recruited.

4.5 Methods

4.5.1 Slice preparation and electrophysiology *in vitro*

Experimental procedures were similar to those described previously (Maier et al., 2009). Horizontal slices (400 μm) were prepared from ventral to mid-hippocampus of C57Bl/6 mice 3 to 4 weeks old, and slices were maintained in an interface chamber superfused with oxygenated artificial cerebrospinal fluid (ACSF) at $\sim$35°C. ACSF contained (in mM): 119 NaC, 2.5 KCl, 1.3 MgSO4, 2.5 CaCl2, 10 glucose, 1.0 NaH2PO4, 26 NaHCO3. Osmolarity of ACSF was routinely checked to range between 290–310 mosmol/l. Slices were incubated for 1–4 hours before being transferred to a submerged chamber for recordings at 31–32°C. Extracellular LFPs from the CA1 field were recorded with ACSF-filled borosilicate glass electrodes of 0.2 to 0.3 MΩ resistances. Within a distance of approximately 160 μm from the LFP electrode (range: 37 to 157 μm), simultaneous whole-cell recordings were performed

from two pyramidal cells. Borosilicate glass electrodes (2–5 MΩ) were filled with Cs-based intracellular solution that contained (in mM): 120 gluconic acid, 10 KCI, 2.0 $MgSO_4$, 3.0 MgATP, 1.0 NaGTP, 5.0 EGTA, 10 Hepes, and 2–3 mg/ml biocytin; pH was adjusted to 7.4 with CsOH. Signals were amplified 1000x, low-pass filtered at 0.7 or 2 kHz and 4 or 8 kHz (LFP and intracellular signals), sampled at 16 bit resolution (National Instruments, Austin, TX), and digitized at 10 or 20 kHz. Data were recorded in Igor Pro (WaveMetrics, Lake Oswego, OR) using a Multiclamp 700A amplifier (Axon Instruments, Foster City, CA). Series resistance (R_S) was monitored continuously throughout experiments; cells were rejected if R_S exceeded 20 MΩ or varied $> 30\%$ during recordings or between cells recorded in parallel. No R_S compensation was used. Voltages were not corrected for liquid junction potentials.

4.5.2 Data analysis

To obtain the instantaneous frequency of inhibition, I calculated the wavelet spectrogram of the band-pass filtered (120–300 Hz) cIPSC. To generate the spectrogram, the inhibitory ripple was convolved with Gabor wavelets covering the band 120–270 Hz in steps of 1 Hz. To reveal the time course of the instantaneous frequency of single ripple events, I located the maximum activation at every time step in the spectrogram (as in Fig. 3.2*B*, white trace). The frequency trace obtained was considered only for the time interval where the envelope of the inhibitory ripple exceeded 3 *std* of the baseline.

5 Effect of GABA modulators on inhibitory networks

Experiments in vitro have shown that ripple frequency is insensitive to drugs that induce a large increase in the amplitude and/or the decay time constant of fast GABAergic transmission. Such a frequency-resistance to modulation of inhibition has been interpreted as evidence against an interneuronal pacemaker for ripple oscillations. Here, I tested the validity of such an argument by simulating the effects of GABA modulators on an interneuronal network model under different driving conditions. First, I used a transiently excited interneuronal network as a model for SWRs in vitro. In that condition, drugs had a strong effect on ripple duration and interneuronal activity but the ripple frequency remained largely unaffected. Similar effects on interneuronal activity and ripple frequency were also observed when the interneurons were driven by persistent, uncorrelated spiking activity. However, when interneurons were driven by homogeneously distributed tonic conductances, the network frequency became sensitive to GABA modulators. emergence of frequency-sensitive oscillations. In conclusion, frequency-sensitivity to GABA modulation is not an intrinsic property of interneuronal network oscillations; it depends on the noise conditions set by the excitatory drive to interneurons.

5.1 Interneuron-network gamma versus ripples *in vitro*

The frequency of SWRs *in vitro* is remarkably resistant to drugs that alter the time constant and peak conductance of GABAergic synaptic transmission (Papatheodoropoulos et al., 2007; Koniaris et al., 2011; Viereckel et al., 2013). Such frequency resistance to GABA modulators has been used as an argument against a ripple-pacemaker relying exclusively on inhibition (Viereckel et al., 2013).

This argument against an interneuronal ripple-pacemaker is motivated by the fact that other forms of interneuronal network oscillations that can be evoked *in vitro* are frequency-sensitive to the same drugs to which ripples are frequency-resistant. For example, in CA1, activation of metabotropic glutamate receptors evokes oscillations in the gamma range (30–90 Hz) that are completely abolished by $GABA_A$ antagonists but prevail in the presence of blockers of fast glutamatergic transmission (Whittington et al., 1995). The frequency of such interneuron network gamma (ING) is highly sensitive to drugs that alter the peak conductance and the decay time constant of $GABA_A$-mediated postsynaptic events (Whittington et al., 1995; Traub et al., 1996). The frequency of ripples, on the other hand, is resistant to the same drugs that have been shown to exert a large effect on ING frequency (Papatheodoropoulos et al., 2007; Koniaris et al., 2011).

Barbiturates, which can lengthen the duration of IPSCs in a concentration-dependent manner, induce qualitatively different effects on the frequencies of ING and ripples. For example, thiopental, in a concentration range of 2–20 μM, can reduce ING frequency down to <50% of its control value (Whittington et al., 1996; Traub et al., 1996). In contrast,

ripple-frequency remains unaltered at concentrations as high as 100 μM; only duration and multiunit activity were reduced with increasing concentration of the drug (Papatheodoropoulos et al., 2007).

Drugs that modulate the amplitude of IPSCs also induce different effects on the two types of oscillations. For example, diazepam, in a concentration range of 0.05 to 0.5 μM, can induce up to a ∼50% reduction in ING frequency, in a concentration-dependent manner (Traub et al., 1996). On the other hand, ripples under benzodiazepine-agonists (diazepam: 0.5–10 μM; zolpidem: 0.1–10 μM) showed only a slight (∼8%) reduction in frequency, with no clear dependence on drug concentration (Koniaris et al., 2011).

Furthermore, the GABA uptake blocker NNC-711, which can induce a large increase in both peak conductance (∼50%) and decay time constant (∼100%), does not seem to affect ripple frequency (Viereckel et al., 2013).

Is it possible that ripples are frequency-resistant to GABAergic modulators and still be paced by an interneuronal network? If this is the case, why is ING, and not ripples, frequency-sensitive to GABAergic modulators? To address these questions, I first tested the effect of the aforementioned drugs in an *in silico* model of SWRs *in vitro*. I show that the drug-response of the model is qualitatively consistent with the results observed *in vitro*. I then show that the conditions of input drive on interneurons used in ING models favor the emergence of frequency-sensitive oscillations in the interneuronal network, which could explain why ING-frequency and ripple-frequency respond differentially to the same drugs.

5.2 The effect of GABA modulators on ripples *in silico*

In the previous chapters, I have provided evidence that SWRs *in vitro* can be well described by a transiently excited interneuronal network. In such a scenario, the network frequency is entirely determined by interactions between interneurons; the sparse activity of pyramids does not play a role in setting the frequency. Consistent with this hypothesis, I will use the response of a transiently excited interneuronal network as a model of SWRs *in vitro* (Fig. 3.2). The model consists of a network of recurrently connected fast-spiking basket-cells driven by Schaffer collateral activity resembling that of CA3 pyramids during SWRs (Fig. 3.2*A*; for details, see sections 2.4 and 3.5.2).

Here, I used the transient response depicted in Figure 3.2 (black traces) as a control condition. The action of a drug was simulated by modifying the peak conductance g_{peak} and the decay time constant τ_D of inhibitory conductances in the model. The transient responses after the simulated application of different drugs are described by the orange traces in Figures 5.1–5.3.

It is important to keep in mind that the effect of the drug is not limited to the synapses between PV^+BCs but also affect the currents generating the LFP. This is of particular importance when comparing experimental results with those obtained *in silico*. In experiments, ripple oscillations are often measured in the *stratum pyramidale* where the LFP is mostly contributed by perisomatic GABAergic synapses onto pyramidal cells. This implies that, in addition to the effect exerted on the interneuron network activity, the drug may also affect the amplitude of the ripple measured in the extracellular field. To capture qualitative changes in the ripple amplitude that might stem from this 'double effect', I used the band-pass filtered (120–300 Hz) inhibitory currents generated by the interneurons in the model as an approximation of the LFP in the ripple band (for details, see Methods at the end of the chapter). Single examples of simulated extracellular ripples before and after application of

the drug are shown as black and orange traces, respectively (Figs. 5.1*F* and 5.2–5.3*E*).

In the following, I simulate the effect of three GABA modulators (NNC-711, thiopental and zolpidem) that have been used to challenge ripples *in vitro*.

5.2.1 GABA uptake blocker NNC-711

The effect of the GABA uptake-blocker NNC-711 was simulated by increasing the decay time constant τ_D of the $GABA_A$ conductance by 100%, and the peak conductance g_{peak} by 50% (Fig. 5.1*B*, inset), as reported by Viereckel et al. (2013). During the simulated application of the drug, the overall shape of the wavelet spectrogram of single events displayed features of SWRs (Fig. 5.1*A*, top); the network activity, however, was quite low (Fig. 5.1*A*, middle; cf. much higher rates in Fig. 3.2*B*). Remarkably, the network frequency was not affected by the drug, and the intra-ripple frequency accommodation (IFA) signature exhibited only a slightly shallower slope when compared to the control condition (Fig. 5.1*B*); the peak frequency of the average power spectrum remained unaltered (Fig. 5.1*C*; control: 200.1 ± 1.6 Hz; NNC-711: 199.9 ± 3.1 Hz), as in experiments (Viereckel et al., 2013).

As a consequence of the reduction in network activity induced by the drug, prominent oscillations were expressed during a shorter time span around the peak of the excitatory activity (Fig. 5.1*A*, middle). This effect was further revealed in the average time course of the power as a much smaller, shorter-lasting peak (Fig. 5.1*D*). Because the simulated effect of NNC-711 increased inhibitory coupling without affecting the excitatory input, the minimum net current required by the network to synchronize was reached only during a shorter time span around the maximum excitation at $t = 0$. As a consequence, the network synchronized later and lost synchrony earlier, and thereby, the duration of the transient response was reduced by $\sim 30\%$ (Fig. 5.1*E*; control: 28.4 ± 0.6 ms; NNC-711: 19.1 ± 0.6 ms). Consistent with the reduction in power, the unit firing rate decreased by 60% in the drug condition (Fig. 5.1*E*; control: 124.7 ± 2.0 spikes/ s; NNC-711: 50.0 ± 0.7 spikes/s).

Interestingly, during the simulated application of NNC-711, the amplitudes of the peaks of the inhibitory currents roughly matched the excitatory currents (Fig. 5.1*A*, bottom), as in the control condition (Fig. 3.2*B*, bottom). The balance of currents remained unaltered because the increase in the inhibitory conductances induced by the drug (Fig. 5.1*B*, inset) was counterbalanced by a reduction in the population activity (Fig. 5.1*A*, middle). As a consequence, the LFP-ripple amplitude was only mildly reduced by NNC-711 (Fig. 5.1*F*).

5.2.2 Thiopental

Another drug that has been used to challenge ripples is the general anesthetic thiopental (Whittington et al., 1996; Dickinson et al., 2002). For ripples *in vitro*, bath application of the drug in a concentration of 50 μM reduced multiunit activity by $\sim$44% and ripple-duration by $\sim$20% without affecting ripple frequency (Papatheodoropoulos et al., 2007).

I simulated the effect of 50 μM thiopental by increasing τ_D of the GABAergic conductance by 80% (Whittington et al., 1996) and keeping g_{peak} unaltered (Fig. 5.2*A*, inset). The network frequency was slightly reduced only during the first half of the ripple (Fig. 5.2*A*) but the peak frequency in the average power spectrum remained unaltered (Fig. 5.2*B*; control: 200.1 ± 1.6 Hz, thiopental: 200.9 ± 2.5 Hz). The power and the duration of the transient response was reduced (Fig. 5.2*C*; control: 28.4 ± 0.6 ms, thiopental: 22.9 ± 1.1 ms). Consistent with the reduction in power of network activity, the unit firing rate was reduced by 40% (Fig. 5.2*D*; control: 124.7 ± 2 spikes/s, thiopental: 73.4 ± 1.3 spikes/s). The LFP ripple

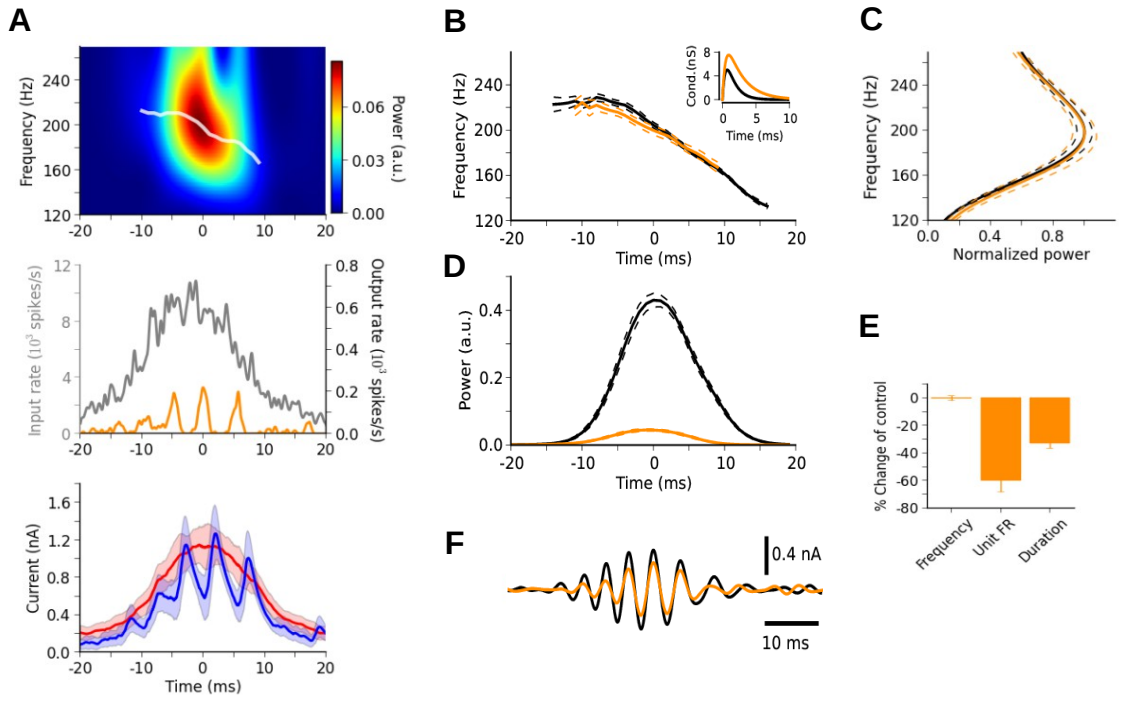

Fig. 5.1: Simulation of the effect of an increased conductance and decay time constant of GABAergic synaptic transmission, e.g. by the GABA-uptake blocker NNC-711, on the transient response of the interneuron network. ***A***, Top: Wavelet spectrogram and instantaneous peak frequency (white trace) of the transient response under the effect of the drug (orange trace in middle). Middle: Overlay of the driving activity (gray trace, input rate) and response of the interneuronal network during exposure to the drug (orange, output rate). Bottom: Mean synaptic currents (red: excitatory, blue: inhibitory) across the population during a single event. ***B***, Average IFA signatures obtained for control (black, identical to Fig. 3.2*D*) and under the effect of the drug (orange). The inset shows the simulated action of the drug on the conductance. ***C***, Normalized average power spectra of network activity for control (black) and under NNC-711 (orange). ***D***, Average time course of ripple power of network activity for control (black) and during exposure to the drug (orange). ***E***, Changes in frequency, firing rate (FR), and duration with respect to control values. ***F***, Examples of simulated ripple extracellular potentials obtained from the mean inhibitory currents shown in *A* (see Methods at the end of the chapter). Each average trace was obtained from 20 simulations.

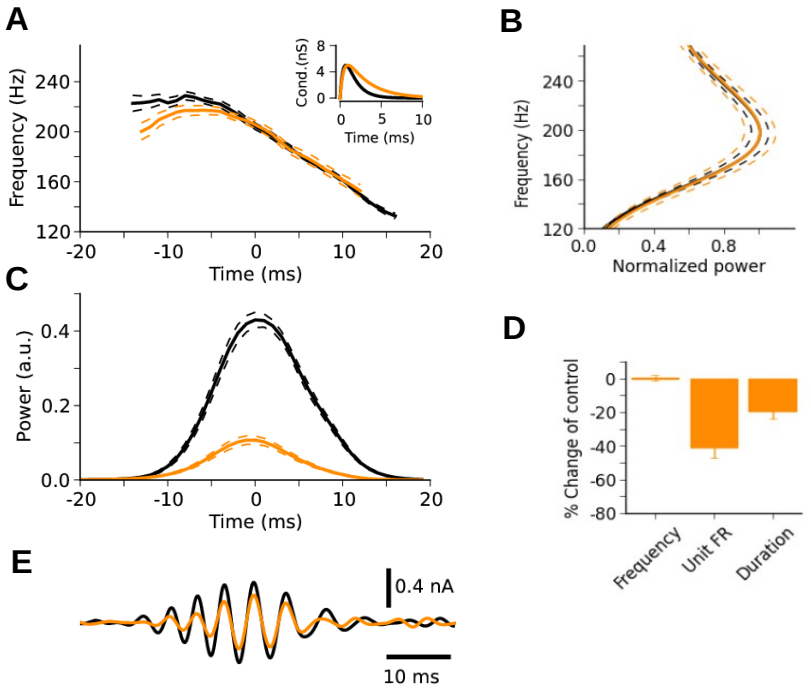

Fig. 5.2: Simulation of the effect of an increased GABA decay time constant, e.g. as induced by thiopental, on the transient response of the interneuron network. ***A***, Average IFA signatures obtained for control (black, identical to Fig. 3.2*D*) and under the effect of the drug (orange). The inset shows the action of the drug on the conductance. ***B***, Normalized average power spectra of network activity for control (black) and during exposure to the drug (orange). ***C***, Average time course of ripple power of network activity for control (black) and during exposure to the drug (orange). ***D***, Changes in frequency, firing rate (FR), and duration with respect to control values. ***E***, Examples of simulated ripple extracellular potentials obtained from the mean inhibitory currents shown in *A* (see Methods at the end of the chapter). Each average trace was obtained from 20 simulations.

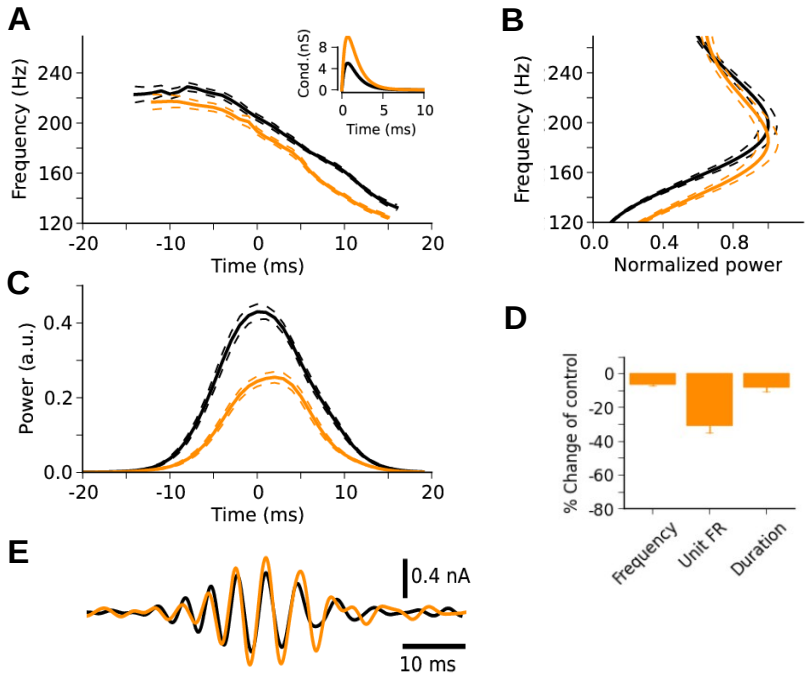

Fig. 5.3: Simulation of the effect of an increased GABA peak conductance, e.g. as induced by zolpidem, on the transient response of the interneuron network. ***A***, Average IFA signatures obtained for control (black, identical to Fig. 3.2*D*) and during exposure to the drug (orange). The inset shows the action of the drug on the conductance. ***B***, Normalized average power spectra of network activity for control (black) and during exposure to the drug (orange). ***C***, Average time course of ripple power of network activity for control (black) and during exposure to the drug (orange). ***D***, Changes in frequency, firing rate (FR), and duration with respect to control values. ***E***, Examples of simulated ripple extracellular potentials obtained from the mean inhibitory currents shown in *A* (see Methods at the end of the chapter). Each average trace was obtained from 20 simulations.

amplitude was also reduced (Fig. 5.2*E*). These results are consistent with the reported effects of thiopental on ripples *in vitro* (Papatheodoropoulos et al., 2007) .

5.2.3 Zolpidem

Benzodiazepines have also been used to probe SWRs *in vitro*. Drugs such as diazepam or zolpidem can increase the IPSP amplitude (Whittington et al. 1996; Pawelzik et al. 1999; Thomson et al. 2000; but see Zarnowska et al. 2009). Here I aimed at illustrating the effect of an idealized drug that selectively increases g_{peak} by 100% without affecting τ_D (Fig. 5.3*A*, inset).

During the simulated application of such a g_{peak} enhancer, the IFA signature was shifted to lower frequencies with no apparent change in the overall shape (Fig. 5.3*A*). The peak frequency in the average power spectrum was decreased by 6% (Fig. 5.3*B, D*; control: 200.1 ± 1.6 Hz, diazepam/zolpidem: 188.0 ± 1.8 Hz). The increase of g_{peak} also decreased the power and the duration of the transient response (Fig. 5.3*C, D*; control: 28.4 ± 0.6 ms, diazepam/zolpidem: 26.2 ± 0.6 ms). The unit firing rate was reduced by 30% (Fig. 5.3*D*; control: 124.7 ± 2 spikes/s; diazepam/zolpidem: 86.6 ± 1.7 spikes/s). Interestingly, the reduc-

tion in unit activity was overcompensated by the increase in the GABAergic conductance, giving rise to an increase in the LFP-ripple amplitude (Fig. 5.3*E*). Such an increase in the amplitude was reported for ripples *in vitro* under zolpidem but not for diazepam (Koniaris et al., 2011).

In summary, the effect of simulated GABA modulators on the transient response of the interneuron network model was qualitatively consistent with effects reported in several experimental studies. Notably, increases in the GABAergic transmission are counterbalanced by a reduction in the network (i.e., unit) activity. The model can explain why drugs that induce an increase in decay time constant of GABAergig synaptic transmission can reduce ripple duration and interneuron firing rates without affecting ripple frequency.

To further generalize my results, I now return to the case of persistent stimulation of an interneuron network.

5.3 The role of noise in frequency sensitivity

In stark contrast to ripples, pharmacologically evoked oscillations in the gamma band that rely exclusively on inhibition are frequency sensitive to GABA modulators (Whittington et al., 1995, 1996; Traub et al., 1996; Fisahn et al., 2004). In agreement, *in silico* models of such interneuron-network gamma (ING) exhibited oscillations which frequency was sensitive to manipulation of GABA parameters (Wang and Buzsáki, 1996; Traub et al., 1996; Bartos et al., 2002). How can interneuron networks generate oscillations that are frequency insensitive (as in the present model) and also frequency sensitive (as in ING models)?

One commonality to ING models is that interneurons are driven by tonic currents that are distributed across cells with low ($CV = 3\%$) variability (Traub et al., 1996; Wang and Buzsáki, 1996). Such a tonic driving input is intended to mimic the steady currents induced by activation of metabotropic channels during pharmacologically evoked ING. Would such a tonic drive generate frequency sensitive oscillations in our model?

To examine this question and connect it to previous results, I compared the response of the network to GABA modulators under two different driving conditions: spiking drive (as during persistent stimulation; see Fig. 2.2) and tonic drive (as in ING models). The results are summarized in Figure 5.4.

I first tested the effect of the GABA-uptake blocker NNC-711 (inset in Fig. 5.4*A*, middle) during persistent stimulation at a rate of 5,500 spikes/s (Fig. 5.4*A*, see also Fig. 2.2). In the control condition, the network oscillated at a frequency of 185 Hz (Fig. 5.4*A*, black trace in middle) and units fired at an average rate of 138 spikes/s (range: from 70 to 179 spikes/s)(Fig. 5.4*A*, black trace, bottom). Under the drug, the frequency of the oscillation in the population exhibited only a slight 4% increase (Fig 5.4*A*, orange trace on top). In contrast, the distribution of firing rates across units was shifted to much lower values (Fig 5.4*A*, orange trace on bottom). Interestingly, the effect of the drug closely resembled that of a decrease in the excitatory drive (see Fig. 2.2*B* and *D*).

I then stimulated the same network by driving the interneurons with tonic excitatory conductances that were normally distributed across the population (Fig. 5.4*B*, top). The mean value of the excitatory conductance used (17.4 nS) was equivalent to the value induced by the spiking stimulation at 5,500 spikes/s. The standard deviation of the conductances was set to 3% of the mean, in accordance with previous ING models (Traub et al., 1996; Wang and Buzsáki, 1996). In the control condition, the network oscillated at 168 Hz (Fig. 5.4*B*, black trace in middle) and all units fired at 168 spikes/s (Fig. 5.4*B*, black trace in bottom),

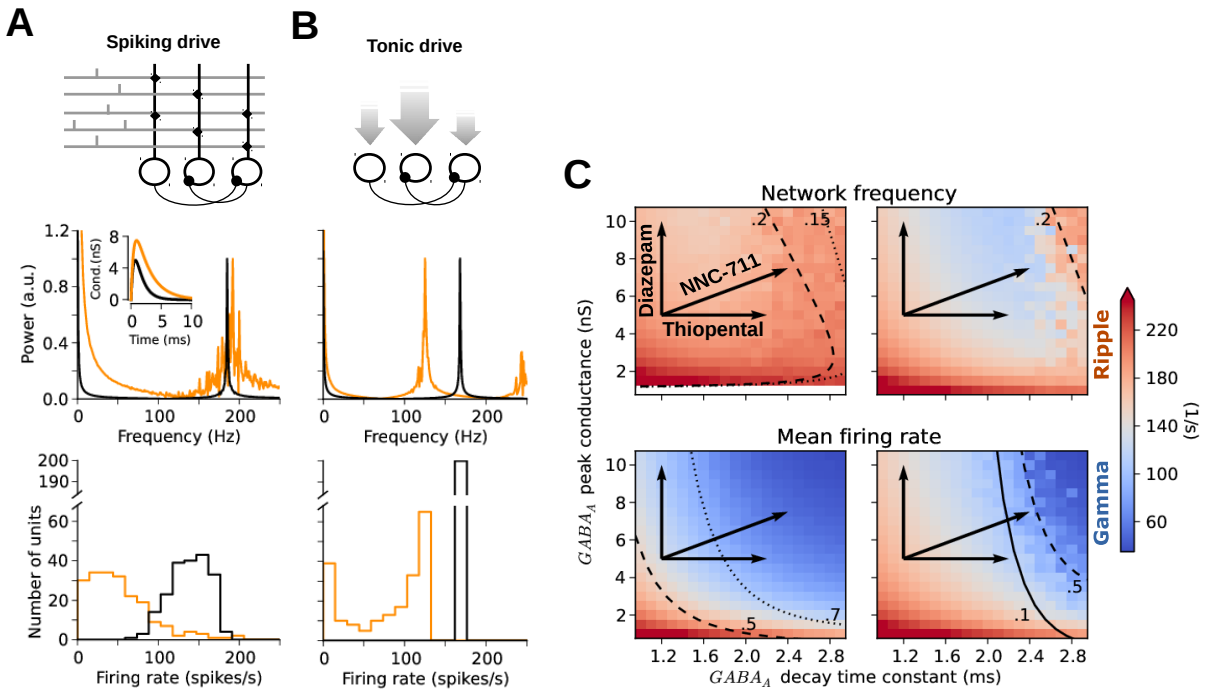

Fig. 5.4: Differential effect of $GABA_A$ parameters on network response for spiking and tonic drives. ***A***, Network driven by uncorrelated spiking activity (top). Normalized power spectral densities (middle) and firing-rate histograms (bottom) for the control condition (black) and for the simulated application of the GABA-uptake blocker NNC-711 (orange). Under the effect of the drug on the postsynaptic conductance (inset), the network peak frequency is almost unaffected but the distribution of firing rates is shifted to lower values. ***B***, Network driven by tonic drive (top). Tonic conductances (gray arrows) were distributed across the population with low variability ($CV = 0.03$). Under the action of the drug (inset in A), both the peak frequency and the firing rates are shifted to lower values. ***C***, Dependence of network peak frequency (top) and mean firing rate (bottom) on $GABA_A$ decay-time constant and peak conductance for spiking drive (left column) and tonic drive (right column). Black arrows describe the changes in $GABA_A$ parameters induced by different drugs. For spiking drive (left), the peak frequency remains relatively insensitive to changes in $GABA_A$ kinetics whereas the mean firing rate is strongly affected. For tonic drive (right), both peak frequency and mean firing rate are rather sensitive to $GABA_A$ parameters. Solid, dashed and dotted lines outline different levels of coherence (top) and CV of firing rate (bottom).

consistent with a fully synchronized ('low noise') regime.

When NNC-711 was applied under the tonic-drive condition, the network-oscillation frequency markedly decreased from 168 Hz to 125 Hz (Fig. 5.4*B*, orange trace in middle). Also the peak of the firing-rate distribution decreased, matching the network-oscillation frequency (Fig. 5.4*B*, orange trace in bottom). It is noteworthy that the distribution of firing rates was not only shifted but also smeared out to lower values (bimodal distribution in Fig. 5.4*B*, bottom). Although a large fraction of units fired at a rate close to the network frequency, the remaining of the distribution revealed units that skipped cycles. The subpopulation expressing low firing rates ($\lesssim$50 spikes/s) spiked irregularly but consistently with the population oscillations (not shown). Thus, the simulated application of NNC-711 under tonic drive not only decreased the network frequency but also allowed the emergence of a sparsely synchronized subpopulation in the network.

How do other drugs that alter GABAergic synaptic transmission affect the network oscillations under the two input conditions? As already explained above (Figs. 5.1–5.3), barbiturates such as thiopental increase preferentially the decay time constant τ_D of the synaptic current (Whittington et al., 1996; Dickinson et al., 2002) whereas benzodiazepines such as diazepam increase the peak conductance g_{peak} without affecting kinetics (Whittington et al., 1996; Pawelzik et al., 1999; but see Zarnowska et al., 2009). To outline the predictions of the *in silico* model regarding the effects of GABA modulators in general, I measured the network frequency and the mean unit firing rate at different combinations of g_{peak} and τ_D under the two driving conditions depicted in Figure 5.4*A* and *B* (top). Figure 5.4*C* shows the network peak frequency (top row) and the mean firing rate across units (bottom row) as a function of g_{peak} (range: 1– 10 nS) and τ_D (range: 1–3 ms). Such a representation of the parameter space allows us to visualize the effect of a drug as a displacement vector that starts at the control value $\tau_D = 1.2$ ms and $g_{\text{peak}} = 5.0$ nS and points at the new values induced by the drug (black arrows in Fig. 5.4*C*).

During the spiking-drive condition (Fig. 5.4*C*, left column), the network frequency remained in the ripple band for a wide range of values of g_{peak} and τ_D. This indicates that drugs affecting the two parameters would induce only minor changes in the network frequency. Remarkably, however, the same drug could induce variable changes depending on the initial condition (i.e., control) in the parameter space. For example, a drug that increases τ_D from 1.2 to 2.2 ms (e.g. thiopental) would result in a small or no change in the network frequency if $g_{\text{peak}} = 5$ nS in the control condition. In contrast, the same change in τ_D would induce a slight increase in the network frequency if $g_{\text{peak}} = 8$ nS in the control condition. The mean firing rate, on the other hand, was much more sensitive and ranged from below 60 to above 220 spikes/s in the simulated parameter space (Fig. 5.4*C*, bottom left). Firing rates strongly decreased with both increasing g_{peak} and increasing τ_D.

During the tonic-drive condition, on the other hand, both the network frequency and the mean firing rate were highly sensitive to changes in g_{peak} and τ_D (Fig. 5.4*C*, right column). The gradient of network frequencies in the observed parameter space showed that frequency and firing rate were inversely related to both g_{peak} and τ_D. This means that drugs inducing an increase in any of these parameters would result in a decrease in both network frequency and firing rate. This trend is consistent with experimental results in the context of induced gamma oscillations *in vitro* (Whittington et al., 1995, 1996; Traub et al., 1996; Fisahn et al., 2004).

Interestingly, close to the highest values of τ_D and g_{peak} tested (upper right corner in color plots) in the tonic-drive condition (Fig. 5.4*C*, right column), high network frequencies

emerged from units firing at low rates. This suggests that changes in τ_D and g_{peak} of GABAergig synaptic transmission can also affect the oscillatory regime. To figure out the expression of different regimes in the observed parameter space, I measured the average CV of unit activity (black contour lines in Fig. 5.4*C*, bottom). In both conditions of driving input, increasing τ_D and/or g_{peak} increased the CV, which means that units fired more irregularly. The transition from full to sparse synchrony may be indicated by CV = 0.5. For spiking drive, a sparsely synchronized regime was observed in most of the shown parameter space (Fig. 5.4*C*, bottom left). For tonic drive, on the other hand, full synchrony expressed in a large area around the control values. Indeed, the region where very low CVs were expressed (CV = 0.1 marked by solid line in Fig. 5.4*C*, bottom right) corresponds to the region where the network frequency closely matched the mean firing rate. It is noteworthy that the CV within this region is considerably lower than the lowest level that could be achieved during the persistent-drive condition at very high rates (see Fig. 2.2*D*, middle). For large values of τ_D and g_{peak}, however, the network expressed sparsely synchronized oscillations; the region characterized by high CVs (CV = 0.5 marked by dashed line in Fig. 5.4*C*, bottom) corresponds to the region where the network frequency and the mean firing rate differ. The mechanisms that enable such a transition are subject of future theoretical research that is beyond the scope of the present study.

In summary, the noise provided by spiking excitatory stimulation favors the emergence of oscillations whose frequency is insensitive to GABA modulators. On the other hand, the conditions of low noise provided by the tonic excitation with low neuron-to-neuron variability, typically used in ING models, favor the emergence of oscillations whose frequency is sensitive to GABA modulators. In conclusion, the fact that ripple oscillations are frequency-insensitive to GABA modulators cannot rule out an interneuronal pacemaker.

5.4 Discussion

In the present chapter, I tested the effect of three example drugs in an *in silico* model of SWRs. Consistent with the effects reported *in vitro* (Papatheodoropoulos et al., 2007; Koniaris et al., 2011; Viereckel et al., 2013), drugs simulated *in silico* affected mainly ripple duration and interneuronal activity but the ripple frequency remained largely unaffected (Figs. 5.1–5.3). To generalize these results, I also tested several combinations of peak conductances and decay time constants when the interneuronal network was driven with uncorrelated spiking activity (Figs. 5.4*A* and *C*, left). Consistent with previous theoretical studies (Brunel and Wang, 2003), the spiking condition favored a 'high noise' state in which frequency is largely independent of peak and decay time constant of GABAergic transmission. In contrast, when interneurons are driven by tonic inputs that are distributed in the population with low variability, the network is mostly in a 'low noise' state in which the network frequency is sensitive to peak and decay time constant of GABAergic transmission (Figs. 5.4*B* and *C*, right).

Here, I studied an idealized case in which the simulated drugs affected only the inhibitory interactions between interneurons (PV^+BC). Moreover, I assumed that the drug had an analogous effect on the perisomatic GABAergic currents generating the extracellular field in the *stratum pyramidale*. These assumptions carry some limitations that I will discuss in light of previous experimental results and the present study.

5.4.1 Effects of GABA modulators on excitatory input

The model did not account for the additional effects a drug might introduce in the excitatory input to interneurons. In chapter 3, I showed that in the transient stimulation condition, the strength and shape of the excitatory input has an influence on the ripple duration, power and frequency (Fig. 3.2*D*–*G*). In the present chapter, to focus on the response of the interneuron network to different drugs, I kept the parameters describing the excitatory input constant. However, during bath application *in vitro*, drugs modifying GABAergic synapses between interneurons can also modify the excitatory input. Therefore, part of the observed effects in CA1 might be due to the action of the drug on the strength and shape of the excitatory burst in CA3. In this respect, thiopental offered an 'easy' case for the model used here. At the simulated concentration (50 μM), thiopental does not affect the field EPSPs recorded in the *stratum radiatum* (Papatheodoropoulos et al., 2007). This might indicate that the excitatory input from CA3 is not significantly altered by the drug, which might be the reason why the effect of thiopental on ripples could be closely reproduced by the model.

5.4.2 Effects of GABA modulators on the extracellular field

The ripple observed in the *stratum pyramidale* of CA1 is mostly contributed by perisomatic GABAergic currents, which reflect the collective activity of basket cells. Consistently, when testing drugs, experimental studies typically use the field and/or inhibitory currents recorded in pyramidal cells as a read out to track the changes in the interneuronal network activity (Whittington et al., 1996; Traub et al., 1996; Papatheodoropoulos et al., 2007; Koniaris et al., 2011; Viereckel et al., 2013). It is therefore important to bear in mind that, when a drug is applied, its action is not limited to the synapses between PV^+BC; it can also, at the same time, affect the synapses mediating the field generation and thereby alter the read out amplitude.

To illustrate the consequences of this 'double effect', I showed how such action of the drug on the readout can dampen an otherwise large reduction in the network activity (as in Figs. 5.1*D* and *F*; and Figs. 5.2*C* and *E*) or even show an increase in amplitude in the presence of a reduction of activity (as in Figs. 5.3*C* and *E*). This is also relevant for the duration of ripple events, which measurement is based on the time the ripple amplitude exceeds a certain threshold (Papatheodoropoulos et al., 2007; Koniaris et al., 2011).

This might be of particular relevance when it comes to clarify some apparently opposite effects of certain drugs. For example, *in vitro*, zolpidem and diazepam show similar effects in network frequency but they display opposite effect in amplitude and duration (measured in the field) at low (<1 μM) concentrations (Papatheodoropoulos et al., 2007). While diazepam tends to reduce amplitude and duration, zolpidem tends to increase these measures. In light of the present results, this seemingly opposite effect could be explained as follows. The similar change in network frequency indicate that both drugs might induce a selective increase of peak conductance on the synapses between PV^+BCs. However, diazepam, and not zolpidem, might introduce an increase in decay time on the GABAergic currents in the perisomatic compartments of pyramidal cells (Zarnowska et al., 2009). Such increase in the decay time constant on those specific GABA conductances might dampen the amplitude of ripples and reduce their duration when measured in the extracellular field.

In summary, to further test the predictions of the model, more experimental work is necessary to describe the effects of the mentioned drugs on inhibitory synapses in the network, namely, the synapses in CA3 that are involved in the generation of the input to CA1, the

synapses coordinating the oscillation (here between PV^+BC), and the synapses mediating the readout (perisomatic $GABA_A$-receptor mediated currents on pyramidal cells in CA1)

In conclusion, frequency-sensitivity to GABAergic modulation is not an intrinsic property of interneuronal network oscillations; it depends on the noise conditions that can be strongly affected by the nature of the excitatory drive to interneurons. Therefore, the frequency-resistance of ripples to inhibitory modulation is not a valid argument against an interneuronal pacemaker.

5.5 Methods

Most of the methods used in the present chapter (network models, driving conditions, data analysis, etc.) have been described in the Methods section of chapters 2 and 3 (please refer to the main text for indications). In the following, I limit the description to those methods that have not been previously described.

5.5.1 Tonic drive

Interneurons were driven by tonic excitatory conductances (see section 3.5.1, Model synapses) that were kept constant throughout the simulation. The conductance values were normally distributed across the population with a mean of 17.4 nS and standard deviation of 0.5 nS, yielding a coefficient of variation of 3%, as in ING models (Traub et al., 1996; Wang and Buzsáki, 1996).

5.5.2 Model of extracellular field ripples

I assumed that ripples in the extracellular field as measured experimentally in the CA1 *stratum pyramidale* are mainly generated by perisomatic inhibitory currents in pyramids, and that such currents reflect the collective activity of PV^+BCs (Schlingloff et al., 2014). To obtain an approximation of the local field potential (LFP) of ripples in the model, I assumed that the perisomatic inhibitory activity experienced by interneurons in the network is similar to that experienced by CA1 pyramidal cells. Therefore, I used the average inhibitory current experienced by the population of interneurons as an approximation for the LFP. It could be argued that $GABA_A$ channels expressed in the perisomatic area of pyramids have different peak conductances and decay time constants as those expressed in interneurons. However, since here the purpose of modeling the LFP is simply to illustrate qualitative *changes* in LFP ripple amplitude as caused by drugs that alter $GABA_A$ parameters, the initial (control) condition of such parameters and their absolute amplitudes are not relevant.

6 Recruitment of oriens-lacunosum moleculare interneurons during hippocampal ripples

Within the hippocampal network, oriens-lacunosum-moleculare (O-LM) interneuron occupy a privileged position to sample the output of local pyramidal cells and modulate their input from thalamus and entorhinal cortex. Here, we used cell-attached and whole-cell recordings in vitro to study the activity of pyramidal cells and O-LM interneurons during ripples. O-LM cells received ripple-associated synaptic input that arrived delayed with respect to the maximum amplitude of field ripples and was locked to the ascending phase of field oscillations. In line, O-LM cells episodically discharged late during ripples, and firing was phase-locked to field oscillations. The recruitment of these interneurons is determined by the balance between the excitatory and inhibitory network activities they experience. The present data suggests a previously uncharacterized role of O-LM neurons during sharp wave-associated activity.[1]

6.1 O-LM interneurons in the CA1 network

Within the neuronal network of the hippocampus, oriens-lacunosum-moleculare (O-LM) interneurons have a peculiar anatomical arrangement with respect to their somatic location and axonal projection area (Sik et al., 1995; Maccaferri, 2005). At distal apical dendrites of CA1 pyramidal cells, the axonal ramification of O-LM cells overlaps with the termination area of fibers from thalamus and entorhinal cortex, suggesting they can modulate input from these brain regions (Wouterlood et al., 1990; Colbert and Levy, 1992; Empson and Heinemann, 1995). Excitatory input onto O-LM cells is primarily local (Blasco-Ibáñez and Freund, 1995), which place them in a privileged position to sample the output of the pyramidal cell network in CA1. Here, we studied the postsynaptic currents on O-LM neurons as well as their spiking behavior during SWRs.

6.2 Synaptic input and spiking activity in O-LM neurons during ripples

We recorded from O-LM interneurons in area CA1 of the hippocampus using both cell-attached and whole-cell patch-clamp techniques. Visually identified by use of infrared-differential interference contrast video microscopy, the somata of these cells were found in stratum oriens and they typically appeared as ovaloids whose longer axis extended in

[1] The research presented in this chapter has also been published as an article (Pangalos et al., 2013) and is the result of a collaboration with several researchers. I developed the tools to analyze phase relationships and input resistance, performed the analyses of phase and input resistance and took part in the writing of the manuscript. Experiments were performed by Maria Pangalos in the lab of Dietmar Schmitz.

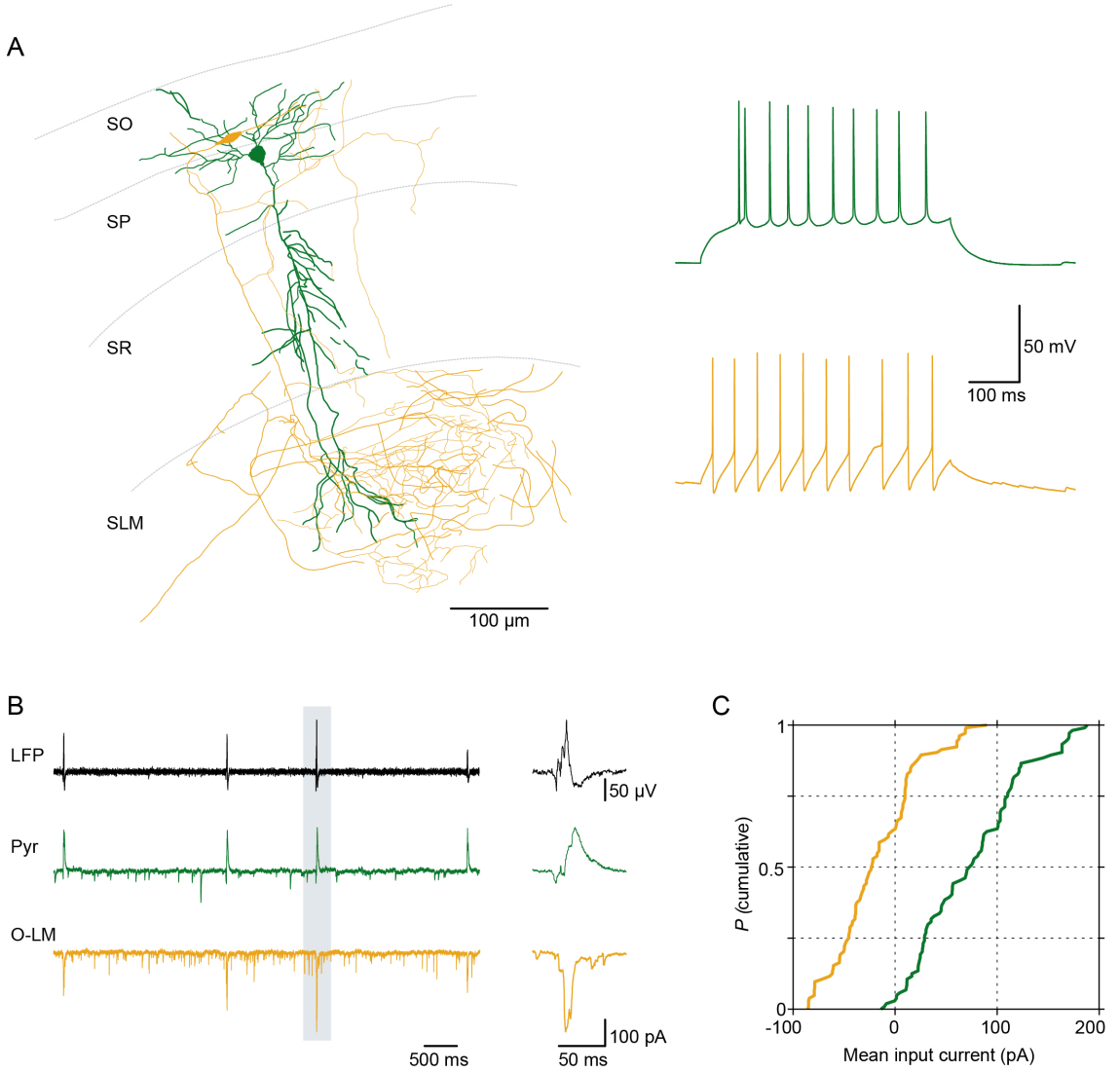

Fig. 6.1: Ripple-associated synaptic input onto O-LM and pyramidal neurons. ***A.*** *Left*: Reconstruction of an O-LM neuron (orange) and a principal cell (green) in area CA1 from a parallel recording. *Right*: Discharge patterns of the displayed cells. ***B.*** Simultaneous LFP and whole-cell voltage-clamp recordings at a slightly depolarized potential (~ -60 mV) unmasks inhibitory (outward) currents in the pyramidal neuron while currents in the O-LM cell remain largely inward (excitatory). *Right*: magnification the indicated period. ***C.*** Population analysis of average synaptic input current in pyramidal- and O-LM neurons (15 randomly picked events from seven pyramidal- and seven O-LM neurons). On average, O-LM neurons display consistently larger ripple-associated inward currents compared to pyramids ($P = 1.5 \times 10^{-26}$, K-S test). Quartiles for the distribution of input onto O-LM cells (orange): Median: -23.2 pA, P25: -47.6 pA, P75: +9.7 pA; for pyramidal cells (green): Median: +72.8 pA, P25: +28.8 pA, P75: +110.3 pA.

parallel with the pyramidal cell layer (Fig. 6.1*A*, orange). O-LM neurons fulfilled the following criteria: (1) axonal ramification in stratum lacunosum-moleculare as identified with post hoc staining, (2) saw-tooth like firing pattern upon mild depolarization, and (3) pronounced voltage sag following hyperpolarization. In the vicinity of O-LM cells ($\leqslant 146\mu$m electrode tip distance), we simultaneously recorded the LFP in the stratum pyramidale (Fig. 6.1*B*). In voltage-clamp recordings, we observed that O-LM neurons regularly received compound postsynaptic currents (cPSCs) associated with LFP ripples (Fig. 6.1*B*, orange traces). To characterize contributions of excitatory and inhibitory input onto O-LM neurons during SWRs, we compared this input with the input in pyramidal neurons (Fig. 6.1*B*, green traces; for details, please refer to Pangalos et al., 2013). We chose an intermediate holding potential for both cell types (~ -60 mV), which allowed us to simultaneously study excitatory and inhibitory contributions. Whereas principal cells displayed a mixed, preferentially outward (inhibitory) current during ripples, O-LM neurons revealed a preponderance of inward currents, indicating stronger excitatory input. For direct comparison, we pooled data from seven O-LM and seven pyramidal cells and found a systematic bias toward excitation in O-LM cells (15 randomly picked events per cell; $P = 1.5 \times 10^{-26}$, Kolmogorov-Smirnov (K–S) test; Fig. 6.1*C*).

6.2.1 Timing of excitatory input

Excitatory input onto CA1 principal neurons during ripples is phasic, coherent across cells, and phase-locked to the LFP (Maier et al., 2011). To similarly characterize the compound excitatory postsynaptic currents (cEPSCs) onto O-LM neurons, we collected cEPSCs recorded close to the reversal potential of Cl^- (-74 mV) and derived their corresponding conductances (for details, please refer to Pangalos et al., 2013). Simultaneous recordings of voltage-clamp signals and the LFP allowed us to compare the timing of excitatory input relative to ripples. First, we juxtaposed the envelopes of conductances and LFPs in the ripple band (127–300 Hz; Fig. 6.2*A*). Across recordings, the peak of excitatory input sampled from O-LM neurons lagged 3.3 ± 0.3 ms behind the peak of the LFP (n = 27 parallel O-LM cell and LFP recordings, 1,791 events analyzed in total; Fig. 6.2*B*). In addition, we determined the phase-coupling of excitatory input relative to ripple cycles. Across cells, phases ranged between 152° and 284°. Input-to-ripple phase was $209 \pm 6°$ on average, demonstrating robust phase coupling to the ascending part of ripple oscillations (Fig. 6.2*C*). Similarly, in 18 cells recorded in the current-clamp configuration at resting membrane potential, we observed a coherence peak at ∼200 Hz, indicating phase-coupling of ripple-associated postsynaptic potentials and the LFP oscillation (see Fig. S4 in Pangalos et al., 2013).

To corroborate the excitatory nature of ripple-locked currents in O-LM neurons, we used intracellular blockers of Cl^--mediated inhibition. In five repatch-experiments with pharmacologically isolated, stimulus-induced IPSCs, we first verified that perfusion of O-LM cells with the Cl-channel blocker disodium 4,4'-diisothiocyanatostilbene-2,2'-disulfonate (DIDS; intracellularly applied as CsF-DIDS) significantly reduced inhibition (IPSC reduction to 13.1 ± 3.6% of control; P = 0.008, rank-sum test). Having established the efficacy of intracellular CsF-DIDS application, we compared SWR-associated currents without and after perfusion of O-LM neurons with CsF-DIDS (seven repatch experiments with CsF-DIDS application longer than 10 min). In either condition, cEPSC phases were locked to LFP ripples (ranges: 158–223° in control and 157–301° in CsF-DIDS), demonstrating phasic excitatory input (for details, please refer to the suplementary material in Pangalos et al., 2013).

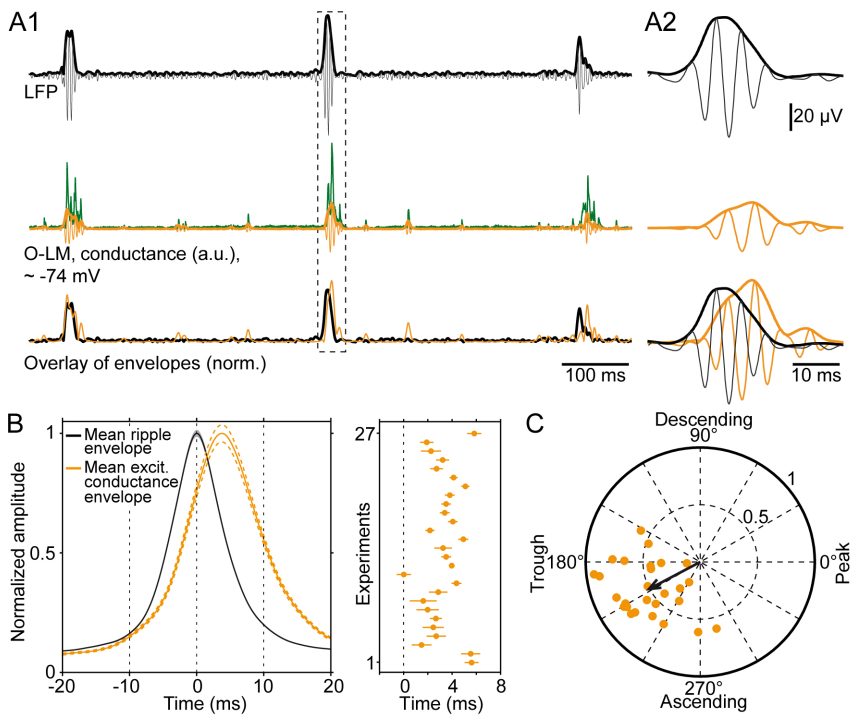

Fig. 6.2: Synaptic input onto O-LM cells is coherent with ripples. ***A.*** Illustration of the analysis. (*A1*) *Top*: ripple (127-300 Hz band-pass filtered LFP, black) overlaid with the envelope (black, bold) derived from the Hilbert transform. *Middle*: input conductance (green), its band-pass filtered version (orange) and the corresponding Hilbert envelope (orange, bold). *Bottom*: overlay of normalized envelopes of LFP and excitatory conductances. (*A2*) Magnification of the highlighted period. ***B.*** *Left* Average envelopes of ripples (black) and excitatory conductances (orange) of 27 cells. The average excitatory input conductance in O-LM neurons lags behind the field ripples by 3.3 ± 0.3 ms. *Right* The orange dots represent the time points of conductance envelope peaks for all 27 cells (range: 0 ms to 5.8 ms). ***C.*** Phases of excitatory conductances with respect to LFP ripples for 27 O-LM cells; orange dots represent the strength and phase of single-cell vectors (black circles and numbers, vector strength scaling; average vector: 208° with a vector strength of 0.51). Across cells, the analysis reveals a strong locking to early ascending ripple phases (mean phase estimation error: 27.1 ± 1.5°; for details, see Pangalos et al., 2013).

6.2.2 Timing of spiking activity

Having established ripple-coupled excitatory currents, we asked whether this input is sufficient to recruit O-LM cells into the spiking network. Perfusion of neurons with the patch-pipette solution during whole-cell recordings changes the intracellular milieu, which might lead to alteration of the firing properties of the cell. We therefore checked in the noninvasive cell-attached recording configuration whether O-LM neurons expressed spikes. In accord with ripple-locked excitatory input, we identified spiking in 13 of 22 experiments. Spikes arrived delayed after the ripple maximum (Fig. 6.3*A*), with a peak spike probability at 6.5 ms (SD: 5.7 ms; 569 spikes; Fig. 6.3*B*). Action currents showed a preference for the ascending phase of ripple cycles (mean phase: 219 ± 9°; 350 spikes; 13 cells; range: 173° to 267°; Fig. 6.3*C*). Collectively, these data demonstrate that ripple-locked excitatory input is sufficient to drive suprathreshold activity in O-LM neurons and spikes are tightly coupled with ripple cycles.

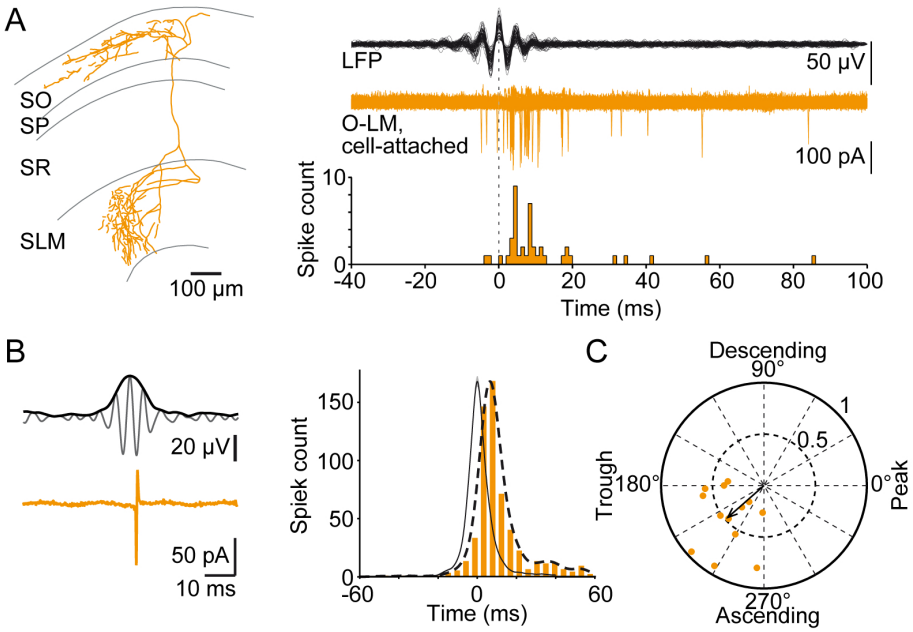

Fig. 6.3: O-LM cells discharge during SWRs, and spikes are phase-locked to ripple oscillation cycles. ***A.*** *Left*: reconstruction of an O-LM neuron. *Right*: overlaid traces of 87 band-pass filtered (127-300 Hz) ripple episodes (*top*, black) and respective cell-attached signals recorded from the displayed neuron (*middle*, orange); all traces were aligned to the ripple maximum (dotted line). *Bottom*: Spike time histogram of action-currents demonstrating delayed activation of the cell and ripple-locked discharge. ***B.*** *Top left*: the 127-300 Hz band-pass filtered LFP overlaid with its envelope; *bottom left*: simultaneously recorded action-currents from the recording shown in (*A*). *Right*: the spike-time histogram (orange) includes all action currents obtained from 13 cell-attached recordings. Overlaid histogram profile (dashed line) represents the sum of Gaussians ($\sigma = 3.7$ ms) centered on the spike times. Spikes occur late during ripples. ***C.*** Polar phase plot indicating average firing phases for the 13 cells recorded in the cell-attached mode (single-cell phase vector tips and vector strength, orange dots); the arrow represents the average vector (221° with a vector strength of 0.47). Note that spike phases cluster to the early ascending phase of ripples.

6.2.3 Determinant factors in cell recruitment

Although all sampled O-LM cells received synaptic input, we identified spiking only in ∼59% of recorded neurons (13 of 22 cell-attached experiments). We asked whether differences in intrinsic cellular properties could account for this disparity. Neither resting membrane potential (P = 0.68, K–S test), nor firing threshold (P = 0.98, K–S test) or input resistance (P = 0.68, K–S test) were different in spiking and nonspiking cells (see Fig. S6 in Pangalos et al., 2013). To further investigate the relation between input currents and spiking, we analyzed O-LM cells separately with respect to spiking (or 'active') vs. not spiking (or 'silent') behavior during ripples. Indeed, spiking probability, i.e., the fraction of SWRs with spikes for a given cell, was correlated with the average excitatory current magnitude in that cell (at -74 mV; R = -0.5, P = 0.017; Fig. 6.4*A*). Close to the inhibitory reversal potential, we found systematically larger cEPSCs for active compared with silent cells (at -74 mV, for spiking and silent cells: -82.7 ± 2.7 pA vs. -41.3 ± 2.1 pA; P = 1.6 x 10–24, K–S test; Fig. 6.4*B*, *D*, and *E* Left). In addition, when we compared inputs at slightly depolarized voltages to unmask inhibitory synaptic input (–54 mV holding potential), we found only small outward (inhibitory) components in discharging cells in contrast to silent O-LM neurons (Fig. 6.4*E*, right). Fig. 6.4*C* summarizes the result for -54 mV holding potential, indicating consistently smaller inward (excitatory) currents with an additional outward current contribution in nonspiking O-LM cells (for spiking and silent cells: -52.4 ± 2.2 pA vs. -8.7 ± 2.5 pA; P = $4.1 \times 10^{-}33$, K–S test). Together, these data demonstrate overall larger excitatory input in spiking O-LM neurons during ripples and more pronounced inhibitory input in silent cells.

6.3 Discussion

Here, we report on two major findings: First, O-LM interneurons consistently receive ripple-associated phasic synaptic input; this input comprises strong excitation, and the ratio of excitation to inhibition in O-LM cells is larger than in CA1 principal cells. Ripple-associated excitation in O-LM neurons lags the LFP ripple by several milliseconds and is phase-locked with field ripples. Second, we observed the suprathreshold recruitment of O-LM cells in 13 out of 22 recordings. Spikes occurred delayed by several milliseconds with respect to the peak of ripples, and they were oscillation-coherent with a preference for the ascending ripple phase.

6.3.1 Network activity determines recruitment of O-LM cells

Our finding of ripple-associated recruitment of O-LM cells is in strong contrast to the previously held view that O-LM neurons exhibit an abrupt drop of spiking during SWRs (Klausberger et al., 2003); however, this previous study was conducted on animals anesthetized with urethane and ketamine. By contrast, a recent study on head-fixed, nonanesthetized mice (Varga et al., 2012) demonstrated activation of O-LM cells during SWRs, in line with our *in vitro* results. In addition to these reports, our data unveil mechanisms that underlie ripple-coherent postsynaptic currents/potentials in the recruitment of O-LM interneurons. To elucidate determinants for spiking and inactivity in O-LM cells, we performed a battery of analyses: Spiking probability was correlated with the magnitude of the respective excitatory input, and the magnitude of excitation was larger in activated versus silent cells. As factors for active participation, we ruled out resting membrane potential, action potential threshold, and input resistance, i. e., intrinsic cellular properties. In addition, across cells,

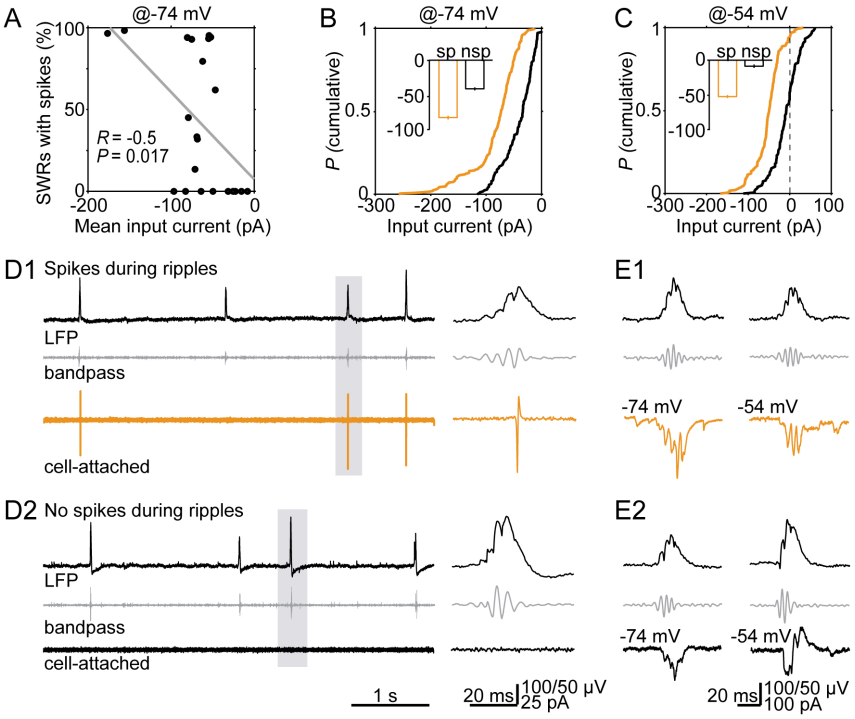

Fig. 6.4: The magnitude of input currents determines the recruitment of O-LM neurons during ripples. ***A.*** The spiking probability of O-LM cells during SWRs is correlated to their mean input current (R = -0.5; P = 0.017; n = 22 experiments). ***B.*** Cumulative probability of the average input current in O-LM cells held at -74 mV for spiking (orange) and silent cells (black). Quartiles of spiking cells: Median: -72.9 pA, P25: -93.8 pA, P75: -53.7 pA; quartiles of non-spiking cells: Median: -33.8 pA, P25: -59.1 pA, P75: -19.3 pA. The inset shows the mean values (sp: spiking; nsp: nonspiking or silent). ***C.*** Distributions of average input currents for spiking (orange) and silent (black) O-LM neurons held at -54 mV. Quartiles of spiking cells: Median: -49.2 pA, P25: -66.6 pA, P75: -33.5 pA; quartiles of nonspiking cells: Median: -8.2 pA, P25: -27.4 pA, P75: 12.1 pA. The inset shows the means values. ***D.*** *Top*: unfiltered LFP, *middle*: 127-300 Hz band-pass filtered LFP, *bottom*: cell-attached recording of a spiking (*top panel, D1*, orange) and of a non-spiking O-LM cell (*bottom panel, D2*, black). The *right panels* show magnifications of the highlighted events. ***E.*** *Top*: unfiltered LFP, *middle*: band-pass filtered LFP, *bottom*: cPSCs of a spiking (*E1*, orange) and a non-spiking O-LM cell (*E2*, black) close to the reversal potential of Cl^- (-74 mV, *left*) and at -54 mV (*right*).

we found that the input magnitude and the probability of recruitment were independent of the cell depth below the slice surface, arguing against differences in the amount of severed inputs to influence recruitment (see Fig. S7 in Pangalos et al., 2013). However, for slices in which O-LM neurons exhibited action potentials during ripples, ripple amplitude, as well as the peak amplitude and incidence of sharp waves were enhanced, suggesting an influence of levels of excitability (see Fig. S8 in Pangalos et al., 2013). Finally, ripple-accompanied inhibition was more pronounced for nonspiking vs. discharging cells. Taken together, all these findings advocate that the magnitude of excitatory network activity and the ratio of excitatory and inhibitory input determine whether O-LM cells are recruited into the active network.

6.3.2 Origin of the delayed ripple-locked activity

The maximum of ripple-locked excitation and the peak of O-LM cell spiking probability lagged the field ripple by several milliseconds. Such delayed ripple-locked activity can be interpreted in different ways depending on the ripple-pacemaker hypothesis one endorses.

Inhibition-first hypothesis. During SWRs *in vitro*, the strong rhythmic perisomatic inhibition provided by the PV^+BC network allows only a very sparse firing of pyramidal cells. Such sparse but precisely timed activity might be sufficient to explain ripple-locked input into an O-LM neuron. In this view, the delayed input of O-LM cells can be accounted for by the action of axo-axonic cells during ripples. Such cells target the axon initial segment of principal neurons (Maccaferri et al., 2000), have their peak firing probability early during ripples and are silent after the ripple maximum (Klausberger et al., 2003). This behavior might account for the delayed recruitment of O-LM cells during ripples.

Excitation-first hypothesis. As shown recently for gamma oscillations in area CA3, pyramidal cell axon spiking outnumbers firing observed at the level of the soma (Dugladze et al., 2012). This experimental observation might also be applicable to ripples in area CA1, an assumption that is supported by modeling results suggesting a network of coupled axons as the origin of ripples (Traub et al., 1999; Draguhn et al., 1998; Bähner et al., 2011; Traub et al., 2012). In this framework, the output of the axonal network might represent the source of field-ripple-coherent excitatory input onto O-LM interneurons. According to this hypothesis, the delayed arrival of input could also be explained by synaptic facilitation, a well known property of excitatory synapses onto O-LM cells in area CA1 (McBain et al., 1994; Ali and Thomson, 1998; Losonczy et al., 2002). Specifically, these connections have a low initial release probability and therefore express robust short-term facilitation that might be regulated by neuromodulation (McBain et al., 1994). In support, presynaptic glutamatergic terminals targeting onto O-LM neurons are highly equipped with metabotropic glutamate receptors (Klausberger et al., 2003; Losonczy et al., 2002).

In summary, we have demonstrated reliable subthreshold activation of O-LM neurons during ripples and the input-dependent suprathreshold recruitment of these cells into the active network. Our findings point to a previously uncharacterized role of O-LM neurons with respect to modulation of ripple-correlated input from entorhinal afferents into CA1. Future work will have to define the behavioral consequences of ripple-associated recruitment of O-LM cells, or their inactivity.

7 Outlook

In this final chapter, I further explore some implications and predictions of the findings presented throughout this thesis. Additionally, I suggest a few lines of theoretical and experimental research that could further advance our understanding of the mechanisms involved in SWR generation.

7.1 Implications of the dual-pathway hypothesis

Considering the intralaminar connectivity of CA1 and the results presented in Chapter 3 on 'Transient Oscillations', I hypothesized that deep and superficial pyramids mediate two excitatory pathways that favor oscillations in the fast gamma range (90–140 Hz) and ripple range (140–200 Hz), respectively (Fig. 3.6*B*). In the following, I briefly discuss some aspects of this hypothesis that deserve further theoretical and experimental analysis.

The results presented in Chapter 3 predict that selective depolarization of the deep calbindin-immunonegative (CB^-) pyramidal cells would favor the emergence of oscillations in the fast gamma range, whereas depolarization of the superficial calbindin-immunoreactive (CB^+) pyramidal cells would favor the expression of oscillations in the ripple band. Such prediction could be tested, for example, by selective optogenetic depolarization of CB^+ pyramidal cells in CA1. The model presented here predicts that such targeted depolarization could evoke frequencies significantly higher than those evoked by unspecific depolarization of pyramidal cells (Stark et al., 2014).

In the general case, however, both subclasses of pyramidal cells and PV^+BC can receive concurrent excitatory input. In such a scenario of unspecific drive, I hypothesized that the intralaminar connectivity between pyramidal cells and PV^+BC could function as a winner-take-all network in which ripples and fast gamma compete for expression (Fig. 3.6*B*). Whether such a network can act as a bistable switch that favors either fast-gamma or ripples is a matter of future theoretical research that would involve extending the present model to consider the simultaneous activation of the proposed pathways (arrows in Fig. 3.6*B*) with variable relative strengths.

Another possibility, suggested here and elsewhere (Slomianka et al., 2011; Mizuseki et al., 2011), is that the deep and superficial pyramidal cells are differentially targeted by anatomically segregated pathways. For example, an experimental study has suggested that deep pyramidal cells might receive a strong influence from the direct entorhinal input (Mizuseki et al., 2011). If this is the case, the dual-pathway hypothesis predicts that excitatory input from the entorhinal cortex would favor oscillations in the fast gamma range. In line with this prediction, a study *in vivo* has shown that, after disruption of the Schaffer collateral (SC) input to CA1, SWRs are still present but with a significant reduction in the average ripple frequency ($\sim$120 Hz compared to $\sim$150 Hz in control) (Nakashiba et al., 2008, 2009). The mechanisms underlying such a frequency reduction are not clear, but it has been suggested that the alteration in the ripple frequency might be due to a change in the types of interneurons recruited in the absence of SC input, or alternatively, due to an hypothesized

ability of the CA1 network to generate slower oscillations autonomously (Buzsáki et al., 1992). I propose that the disruption of the SC contributes to dis-inhibit the input from the temporoammonic pathway allowing the targeted influence of the entorhinal cortex onto deep pyramids to favor oscillations in the fast-gamma range. Further experimental work in this direction should be aimed at examining the putative differential origin of the excitatory afferents innervating deep and superficial pyramidal cells in CA1.

If the direct projections from EC preferentially innervate deep pyramids as predicted, the O-LM cells acquire an important role in modulating the expression of fast-gamma or ripples. It has been shown that O-LM cell activity can reduce the influence of entorhinal input to CA1 and, at the same time, also boost the SC input by inhibition of interneurons in *stratum radiatum* (Leão et al., 2012). Further experimental work in this direction should be aimed at testing whether the activation of O-LM cells is correlated with the expression of higher ripple frequencies *in vivo*.

So far, most studies have treated SWRs as a single class of network oscillation, disregarding the functional relevance the observed variability in ripple-frequency may have (Buzsáki, 2015; Girardeau and Zugaro, 2011). However, it is possible that a functional differentiation between those SWRs containing fast gamma and ripples exists. A preliminary indication in this direction can be found in the aforementioned study from Nakashiba et al. (2009). They showed that, even in the absence of SC input, the minority of events displaying high intrinsic ripple frequency (i.e., within the control range) were capable of supporting the reactivation of experience-related sequences, in contrast to their slower counterparts. Further computational and experimental studies should be aimed at disentangling the putative differential function of fast-gamma associated and ripple-associated SWR events.

7.2 Synaptic input to the basket cell network

In spite of the central role played by PV^+BCs during SWRs, there is surprisingly little evidence on the synaptic input they receive during these network events. Such information could provide valuable insights on the mechanisms underlying SWRs. In light of the present results, the analysis of excitatory currents on PV^+BC is of paramount importance.

The model presented in Chapter 3 (Fig. 3.6*B*) predicts that, during fast gamma events, BCs should experience a strongly modulated oscillatory excitatory input due to the recruitment of the pyramidal-interneuron loop. During faster events, on the other hand, the degree of oscillatory modulation should be significantly smaller in comparison. Unfortunately, testing this prediction would require difficult experiments involving whole-cell voltage-clamp recordings of BCs *in vivo* (Lee et al., 2006).

The characterization of excitatory synaptic currents onto BCs could also provide insights on the pacemaking mechanism dominating the ripple frequency. In chapter 4, I argued that ripples *in vitro* are well described by a directly driven interneuronal network where the pyramidal-interneuron loop is not effectively recruited. In such a case, the inhibition-first hypothesis predicts an excitatory input containing a weak ripple component. The excitation-first hypothesis, on the other hand, predicts an excitatory input with a strong oscillatory modulation (Traub and Bibbig, 2000; Memmesheimer, 2010). This oscillatory excitation should also exhibit a low mean, which is a requirement for the effective entrainment of the interneuronal network, as shown in Chapter 2 (Fig. 2.4). Whole-cell recordings on identified fast-spiking BCs *in vitro* would provide typical values of modulation depth and mean conductances, which could be later compared to those depicted in Figure 2.4*D*. This

would allow an assessment of the putative pacemaker mechanism that is dominating the ripple frequency.

The analysis of synaptic currents onto BCs might require certain care. Concurrently with the excitatory current we aim at characterizing, PV^+BC receive strongly modulated inhibitory input from their recurrent collaterals (Bartos et al., 2002). Disentangling these two oscillatory components (excitatory versus inhibitory) reliably might require the use of intracellular blockers or, alternatively, analyzing the phase of the oscillatory current as a function of holding potential (Hulse et al., 2016).

7.3 Intra-ripple frequency accommodation

The phenomenon of intra-ripple frequency accommodation (IFA) imposes constraints on the existing models of ripple generation. The experimental results presented in Chapter 4 require that the observed relationship between the time courses of excitation and instantaneous frequency be accounted for (Fig. 4.4). In Chapter 3, I showed that a transiently excited interneuronal network not only displays IFA but also exhibits the experimentally observed relationship between the excitatory phase and the instantaneous frequency observed experimentally (Fig. 3.2). Could IFA also be explained by excitation-first models?

Independently of the mechanism used to generate the excitatory ripple, the phenomenon of IFA requires a change in the parameters controlling the frequency within the time course of a single SWR.

In the axon-plexus model, for example, one factor that could dynamically control the frequency is the spike-to-spike latency as spikes propagate and reproduce within the axon plexus (Traub and Bibbig, 2000). One mechanism that could mediate a slow down of the frequency within a SWR is the decrease in action potential amplitude with somatic depolarization of pyramidal cells (Shu et al., 2006). Such latency adaptation might require the inclusion of additional active currents in the axon-plexus model (Shu et al., 2007).

For the synchrony propagation model proposed by Memmesheimer (2010), I am not aware of a mechanism that could generate IFA.

In summary, the *in silico* models presented in this thesis make specific experimental predictions, which will allow to test the inhibition-first hypothesis for the generation of ripple oscillations, and explore the functional role of the intralaminar connectivity in the *stratum pyramidale* of CA1.

Bibliography

Aika, Y., Ren, J. Q., Kosaka, K., and Kosaka, T. (1994). Quantitative analysis of GABA-like-immunoreactive and parvalbumin-containing neurons in the CA1 region of the rat hippocampus using a stereological method, the disector. *Exp Brain Res*, 99(2):267–76.

Ali, A. B. and Thomson, A. M. (1998). Facilitating pyramid to horizontal oriens-alveus interneurone inputs: dual intracellular recordings in slices of rat hippocampus. *J. Physiol. (Lond.)*, 507 (Pt 1):185–99.

Amaral, D. G. and Witter, M. P. (1989). The three-dimensional organization of the hippocampal formation: a review of anatomical data. *Neuroscience*, 31(3):571–91.

Ariav, G., Polsky, A., and Schiller, J. (2003). Submillisecond precision of the input-output transformation function mediated by fast sodium dendritic spikes in basal dendrites of CA1 pyramidal neurons. *J Neurosci*, 23(21):7750–8.

Axmacher, N., Elger, C. E., and Fell, J. (2008). Ripples in the medial temporal lobe are relevant for human memory consolidation. *Brain*, 131(Pt 7):1806–17.

Başar, E. and Güntekin, B. (2008). A review of brain oscillations in cognitive disorders and the role of neurotransmitters. *Brain Res.*, 1235:172–93.

Bähner, F., Weiss, E. K., Birke, G., Maier, N., Schmitz, D., Rudolph, U., Frotscher, M., Traub, R. D., Both, M., and Draguhn, A. (2011). Cellular correlate of assembly formation in oscillating hippocampal networks in vitro. *Proc Natl Acad Sci U S A*, 108(35):E607–16.

Bartos, M., Vida, I., Frotscher, M., Meyer, A., Monyer, H., Geiger, J. R. P., and Jonas, P. (2002). Fast synaptic inhibition promotes synchronized gamma oscillations in hippocampal interneuron networks. *Proc Natl Acad Sci U S A*, 99(20):13222–7.

Bartos, M., Vida, I., and Jonas, P. (2007). Synaptic mechanisms of synchronized gamma oscillations in inhibitory interneuron networks. *Nat Rev Neurosci*, 8(1):45–56.

Behrens, C. J., van den Boom, L. P., de Hoz, L., Friedman, A., and Heinemann, U. (2005). Induction of sharp wave-ripple complexes in vitro and reorganization of hippocampal networks. *Nat Neurosci*, 8(11):1560–7.

Bezaire, M. J. and Soltesz, I. (2013). Quantitative assessment of CA1 local circuits: knowledge base for interneuron-pyramidal cell connectivity. *Hippocampus*, 23(9):751–85.

Blasco-Ibáñez, J. M. and Freund, T. F. (1995). Synaptic input of horizontal interneurons in stratum oriens of the hippocampal CA1 subfield: structural basis of feed-back activation. *Eur. J. Neurosci.*, 7(10):2170–80.

Bouyer, J. J., Montaron, M. F., and Rougeul, A. (1981). Fast fronto-parietal rhythms during combined focused attentive behaviour and immobility in cat: cortical and thalamic localizations. *Electroencephalogr Clin Neurophysiol*, 51(3):244–52.

Bragin, A., Engel, J., Wilson, C. L., Fried, I., and Buzsáki, G. (1999). High-frequency oscillations in human brain. *Hippocampus*, 9(2):137–42.

Bragin, A., Jandó, G., Nádasdy, Z., Hetke, J., Wise, K., and Buzsáki, G. (1995). Gamma (40-100 Hz) oscillation in the hippocampus of the behaving rat. *J. Neurosci.*, 15(1 Pt 1):47–60.

Brown, M. W. and Aggleton, J. P. (2001). Recognition memory: what are the roles of the perirhinal cortex and hippocampus? *Nat. Rev. Neurosci.*, 2(1):51–61.

Brunel, N. (2000). Dynamics of Sparsely Connected Networks of Excitatory and Inhibitory Spiking Neurons. *Journal of Computational Neuroscience*, 8(3):183–208.

Brunel, N. and Hakim, V. (2008). Sparsely synchronized neuronal oscillations. *Chaos*, 18(1):015113.

Brunel, N. and Wang, X.-J. (2003). What determines the frequency of fast network oscillations with irregular neural discharges? I. Synaptic dynamics and excitation-inhibition balance. *J Neurophysiol*, 90(1):415–30.

Buck, J. (1988). Synchronous Rhythmic Flashing of Fireflies. II. *The Quarterly Review of Biology*, 63(3):265–289.

Buhl, E. H., Cobb, S. R., Halasy, K., and Somogyi, P. (1995). Properties of unitary IPSPs evoked by anatomically identified basket cells in the rat hippocampus. *Eur J Neurosci*, 7(9):1989–2004.

Buhl, E. H., Han, Z. S., Lörinczi, Z., Stezhka, V. V., Karnup, S. V., and Somogyi, P. (1994). Physiological properties of anatomically identified axo-axonic cells in the rat hippocampus. *J Neurophysiol*, 71(4):1289–307.

Buhl, E. H., Szilágyi, T., Halasy, K., and Somogyi, P. (1996). Physiological properties of anatomically identified basket and bistratified cells in the CA1 area of the rat hippocampus in vitro. *Hippocampus*, 6(3):294–305.

Butters, N. and Cermak, L. S. (1988). 14 A case study of the forgetting of autobiographical knowledge: implications for the study of retrograde amnesia. *Autobiographical memory*, page 253.

Buzsáki, G. (1984). Long-term changes of hippocampal sharp-waves following high frequency afferent activation. *Brain Res.*, 300(1):179–82.

Buzsáki, G. (1986). Hippocampal sharp waves: their origin and significance. *Brain Res*, 398(2):242–52.

Buzsáki, G. (1989). Two-stage model of memory trace formation: a role for "noisy" brain states. *Neuroscience*, 31(3):551–70.

Buzsáki, G. (1998). Memory consolidation during sleep: a neurophysiological perspective. *J Sleep Res*, 7 Suppl 1:17–23.

Buzsaki, G. (2006). *Rhythms of the Brain*. Oxford University Press.

Buzsáki, G. (2015). Hippocampal sharp wave-ripple: A cognitive biomarker for episodic memory and planning. *Hippocampus*, 25(10):1073–188.

Buzsáki, G. and Draguhn, A. (2004). Neuronal oscillations in cortical networks. *Science*, 304(5679):1926–9.

Buzsáki, G., Horváth, Z., Urioste, R., Hetke, J., and Wise, K. (1992). High-frequency network oscillation in the hippocampus. *Science*, 256(5059):1025–7.

Buzsáki, G., Leung, L. W., and Vanderwolf, C. H. (1983). Cellular bases of hippocampal EEG in the behaving rat. *Brain Res.*, 287(2):139–71.

Buzsáki, G. and Moser, E. I. (2013). Memory, navigation and theta rhythm in the hippocampal-entorhinal system. *Nat. Neurosci.*, 16(2):130–8.

Buzsáki, G. and Wang, X.-J. (2012). Mechanisms of gamma oscillations. *Annu. Rev. Neurosci.*, 35:203–25.

Buzsáki, G. and Watson, B. O. (2012). Brain rhythms and neural syntax: implications for efficient coding of cognitive content and neuropsychiatric disease. *Dialogues Clin Neurosci*, 14(4):345–67.

Carr, M. F., Jadhav, S. P., and Frank, L. M. (2011). Hippocampal replay in the awake state: a potential substrate for memory consolidation and retrieval. *Nat. Neurosci.*, 14(2):147–53.

Colbert, C. M. and Levy, W. B. (1992). Electrophysiological and pharmacological characterization of perforant path synapses in CA1: mediation by glutamate receptors. *J. Neurophysiol.*, 68(1):1–8.

Csicsvari, J., Hirase, H., Czurkó, A., Mamiya, A., and Buzsáki, G. (1999a). Fast network oscillations in the hippocampal CA1 region of the behaving rat. *J. Neurosci.*, 19(16):RC20.

Csicsvari, J., Hirase, H., Czurkó, A., Mamiya, A., and Buzsáki, G. (1999b). Oscillatory coupling of hippocampal pyramidal cells and interneurons in the behaving Rat. *J. Neurosci.*, 19(1):274–87.

Csicsvari, J., Hirase, H., Mamiya, A., and Buzsáki, G. (2000). Ensemble patterns of hippocampal CA3-CA1 neurons during sharp wave-associated population events. *Neuron*, 28(2):585–94.

de la Prida, L. M., Huberfeld, G., Cohen, I., and Miles, R. (2006). Threshold behavior in the initiation of hippocampal population bursts. *Neuron*, 49(1):131–42.

Deuchars, J. and Thomson, A. M. (1996). CA1 pyramid-pyramid connections in rat hippocampus in vitro: dual intracellular recordings with biocytin filling. *Neuroscience*, 74(4):1009–18.

Diba, K. and Buzsáki, G. (2007). Forward and reverse hippocampal place-cell sequences during ripples. *Nat. Neurosci.*, 10(10):1241–2.

Dickinson, R., de Sousa, S. L. M., Lieb, W. R., and Franks, N. P. (2002). Selective synaptic actions of thiopental and its enantiomers. *Anesthesiology*, 96(4):884–92.

Dougherty, K. A., Islam, T., and Johnston, D. (2012). Intrinsic excitability of CA1 pyramidal neurones from the rat dorsal and ventral hippocampus. *J. Physiol. (Lond.)*, 590(Pt 22):5707–22.

Dragoi, G. and Tonegawa, S. (2011). Preplay of future place cell sequences by hippocampal cellular assemblies. *Nature*, 469(7330):397–401.

Draguhn, A., Traub, R. D., Schmitz, D., and Jefferys, J. G. (1998). Electrical coupling underlies high-frequency oscillations in the hippocampus in vitro. *Nature*, 394(6689):189–92.

Dugladze, T., Schmitz, D., Whittington, M. A., Vida, I., and Gloveli, T. (2012). Segregation of axonal and somatic activity during fast network oscillations. *Science*, 336(6087):1458–61.

Ego-Stengel, V. and Wilson, M. A. (2010). Disruption of ripple-associated hippocampal activity during rest impairs spatial learning in the rat. *Hippocampus*, 20(1):1–10.

Empson, R. M. and Heinemann, U. (1995). The perforant path projection to hippocampal area CA1 in the rat hippocampal-entorhinal cortex combined slice. *J. Physiol. (Lond.)*, 484 (Pt 3):707–20.

English, D. F., Peyrache, A., Stark, E., Roux, L., Vallentin, D., Long, M. A., and Buzsáki, G. (2014). Excitation and inhibition compete to control spiking during hippocampal ripples: intracellular study in behaving mice. *J. Neurosci.*, 34(49):16509–17.

Eschenko, O., Ramadan, W., Mölle, M., Born, J., and Sara, S. J. (2008). Sustained increase in hippocampal sharp-wave ripple activity during slow-wave sleep after learning. *Learn. Mem.*, 15(4):222–8.

Ferguson, K. A., Huh, C. Y. L., Amilhon, B., Williams, S., and Skinner, F. K. (2013). Experimentally constrained CA1 fast-firing parvalbumin-positive interneuron network models exhibit sharp transitions into coherent high frequency rhythms. *Front Comput Neurosci*, 7:144.

Fisahn, A., Contractor, A., Traub, R. D., Buhl, E. H., Heinemann, S. F., and McBain, C. J. (2004). Distinct roles for the kainate receptor subunits GluR5 and GluR6 in kainate-induced hippocampal gamma oscillations. *J. Neurosci.*, 24(43):9658–68.

Forro, T., Valenti, O., Lasztoczi, B., and Klausberger, T. (2015). Temporal organization of GABAergic interneurons in the intermediate CA1 hippocampus during network oscillations. *Cereb. Cortex*, 25(5):1228–40.

Foster, D. J. and Wilson, M. A. (2006). Reverse replay of behavioural sequences in hippocampal place cells during the awake state. *Nature*, 440:680–683.

Freund, T. F. (2003). Interneuron Diversity series: Rhythm and mood in perisomatic inhibition. *Trends Neurosci.*, 26(9):489–95.

Freund, T. F. and Buzsáki, G. (1996). Interneurons of the hippocampus. *Hippocampus*, 6(4):347–470.

Ganter, P., Szücs, P., Paulsen, O., and Somogyi, P. (2004). Properties of horizontal axo-axonic cells in stratum oriens of the hippocampal CA1 area of rats in vitro. *Hippocampus*, 14(2):232–43.

Ganzetti, M. and Mantini, D. (2013). Functional connectivity and oscillatory neuronal activity in the resting human brain. *Neuroscience*, 240:297–309.

Girardeau, G., Benchenane, K., Wiener, S. I., Buzsáki, G., and Zugaro, M. B. (2009). Selective suppression of hippocampal ripples impairs spatial memory. *Nat. Neurosci.*, 12(10):1222–3.

Girardeau, G. and Zugaro, M. (2011). Hippocampal ripples and memory consolidation. *Curr. Opin. Neurobiol.*, 21(3):452–9.

Goodman, D. and Brette, R. (2009). The Brian simulator. *Front. Neurosci.*

Gupta, A. S., van der Meer, M. A., Touretzky, D. S., and Redish, A. D. (2010). Hippocampal replay is not a simple function of experience. *Neuron*, 65(5):695–705.

Hájos, N., Karlócai, M. R., Németh, B., Ulbert, I., Monyer, H., Szabó, G., Erdélyi, F., Freund, T. F., and Gulyás, A. I. (2013). Input-output features of anatomically identified CA3 neurons during hippocampal sharp wave/ripple oscillation in vitro. *J. Neurosci.*, 33(28):11677–91.

Halasy, K., Buhl, E. H., Lörinczi, Z., Tamás, G., and Somogyi, P. (1996). Synaptic target selectivity and input of GABAergic basket and bistratified interneurons in the CA1 area of the rat hippocampus. *Hippocampus*, 6(3):306–29.

Hebb, D. O. (1949). *The organization of behavior: A neuropsychological approach.* John Wiley & Sons.

Huber, R., Ghilardi, M. F., Massimini, M., and Tononi, G. (2004). Local sleep and learning. *Nature*, 430(6995):78–81.

Hulse, B. K., Moreaux, L. C., Lubenov, E. V., and Siapas, A. G. (2016). Membrane Potential Dynamics of CA1 Pyramidal Neurons during Hippocampal Ripples in Awake Mice. *Neuron*, 89(4):800–13.

Ishizuka, N., Weber, J., and Amaral, D. G. (1990). Organization of intrahippocampal projections originating from CA3 pyramidal cells in the rat. *J. Comp. Neurol.*, 295(4):580–623.

Jahnke, S., Timme, M., and Memmesheimer, R.-M. (2015). A Unified Dynamic Model for Learning, Replay, and Sharp-Wave/Ripples. *J. Neurosci.*, 35(49):16236–58.

Jasper, H. and Penfield, W. (1949). Electrocorticograms in man: effect of voluntary movement upon the electrical activity of the precentral gyrus. *Archiv für Psychiatrie und Nervenkrankheiten*, 183(1-2):163–174.

Karson, M. A., Tang, A.-H., Milner, T. A., and Alger, B. E. (2009). Synaptic cross talk between perisomatic-targeting interneuron classes expressing cholecystokinin and parvalbumin in hippocampus. *J. Neurosci.*, 29(13):4140–54.

Katona, L., Lapray, D., Viney, T. J., Oulhaj, A., Borhegyi, Z., Micklem, B. R., Klausberger, T., and Somogyi, P. (2014). Sleep and movement differentiates actions of two types of somatostatin-expressing GABAergic interneuron in rat hippocampus. *Neuron*, 82(4):872–86.

Kempter, R., Gerstner, W., van Hemmen, J. L., and Wagner, H. (1998). Extracting oscillations. Neuronal coincidence detection with noisy periodic spike input. *Neural Comput*, 10(8):1987–2017.

Kiss, J., Buzsaki, G., Morrow, J. S., Glantz, S. B., and Leranth, C. (1996). Entorhinal cortical innervation of parvalbumin-containing neurons (Basket and Chandelier cells) in the rat Ammon's horn. *Hippocampus*, 6(3):239–46.

Klausberger, T., Magill, P. J., Márton, L. F., Roberts, J. D. B., Cobden, P. M., Buzsáki, G., and Somogyi, P. (2003). Brain-state- and cell-type-specific firing of hippocampal interneurons in vivo. *Nature*, 421(6925):844–8.

Klausberger, T., Marton, L. F., O'Neill, J., Huck, J. H. J., Dalezios, Y., Fuentealba, P., Suen, W. Y., Papp, E., Kaneko, T., Watanabe, M., Csicsvari, J., and Somogyi, P. (2005). Complementary roles of cholecystokinin- and parvalbumin-expressing GABAergic neurons in hippocampal network oscillations. *J Neurosci*, 25(42):9782–93.

Klimesch, W. (1999). EEG alpha and theta oscillations reflect cognitive and memory performance: a review and analysis. *Brain Res. Brain Res. Rev.*, 29(2-3):169–95.

Koniaris, E., Drimala, P., Sotiriou, E., and Papatheodoropoulos, C. (2011). Different effects of zolpidem and diazepam on hippocampal sharp wave-ripple activity in vitro. *Neuroscience*, 175:224–34.

Lapray, D., Lasztoczi, B., Lagler, M., Viney, T. J., Katona, L., Valenti, O., Hartwich, K., Borhegyi, Z., Somogyi, P., and Klausberger, T. (2012). Behavior-dependent specialization of identified hippocampal interneurons. *Nat Neurosci*, 15(9):1265–71.

Leão, R. N., Mikulovic, S., Leão, K. E., Munguba, H., Gezelius, H., Enjin, A., Patra, K., Eriksson, A., Loew, L. M., Tort, A. B. L., and Kullander, K. (2012). OLM interneurons differentially modulate CA3 and entorhinal inputs to hippocampal CA1 neurons. *Nat. Neurosci.*, 15(11):1524–30.

Lee, A. K., Manns, I. D., Sakmann, B., and Brecht, M. (2006). Whole-cell recordings in freely moving rats. *Neuron*, 51(4):399–407.

Lee, A. K. and Wilson, M. A. (2002). Memory of sequential experience in the hippocampus during slow wave sleep. *Neuron*, 36(6):1183–94.

Lee, S.-H., Marchionni, I., Bezaire, M., Varga, C., Danielson, N., Lovett-Barron, M., Losonczy, A., and Soltesz, I. (2014). Parvalbumin-positive basket cells differentiate among hippocampal pyramidal cells. *Neuron*, 82(5):1129–44.

Li, X. G., Somogyi, P., Ylinen, A., and Buzsáki, G. (1994). The hippocampal CA3 network: an in vivo intracellular labeling study. *J. Comp. Neurol.*, 339(2):181–208.

Losonczy, A., Zhang, L., Shigemoto, R., Somogyi, P., and Nusser, Z. (2002). Cell type dependence and variability in the short-term plasticity of EPSCs in identified mouse hippocampal interneurones. *J. Physiol. (Lond.)*, 542(Pt 1):193–210.

Maccaferri, G. (2005). Stratum oriens horizontal interneurone diversity and hippocampal network dynamics. *J. Physiol. (Lond.)*, 562(Pt 1):73–80.

Maccaferri, G., Roberts, J. D., Szucs, P., Cottingham, C. A., and Somogyi, P. (2000). Cell surface domain specific postsynaptic currents evoked by identified GABAergic neurones in rat hippocampus in vitro. *J. Physiol. (Lond.)*, 524 Pt 1:91–116.

Maex, R. and Schutter, E. D. (2003). Resonant synchronization in heterogeneous networks of inhibitory neurons. *J. Neurosci.*, 23(33):10503–14.

Maier, N., Morris, G., Johenning, F. W., and Schmitz, D. (2009). An approach for reliably investigating hippocampal sharp wave-ripples in vitro. *PLoS ONE*, 4(9):e6925.

Maier, N., Nimmrich, V., and Draguhn, A. (2003). Cellular and network mechanisms underlying spontaneous sharp wave-ripple complexes in mouse hippocampal slices. *J Physiol*, 550(Pt 3):873–87.

Maier, N., Tejero-Cantero, A., Dorrn, A. L., Winterer, J., Beed, P. S., Morris, G., Kempter, R., Poulet, J. F. A., Leibold, C., and Schmitz, D. (2011). Coherent phasic excitation during hippocampal ripples. *Neuron*, 72(1):137–52.

Manns, J. R. and Eichenbaum, H. (2006). Evolution of declarative memory. *Hippocampus*, 16(9):795–808.

Masquelier, T., Hugues, E., Deco, G., and Thorpe, S. J. (2009). Oscillations, phase-of-firing coding, and spike timing-dependent plasticity: an efficient learning scheme. *J. Neurosci.*, 29(43):13484–93.

Maviel, T., Durkin, T. P., Menzaghi, F., and Bontempi, B. (2004). Sites of neocortical reorganization critical for remote spatial memory. *Science*, 305(5680):96–9.

McBain, C. J., DiChiara, T. J., and Kauer, J. A. (1994). Activation of metabotropic glutamate receptors differentially affects two classes of hippocampal interneurons and potentiates excitatory synaptic transmission. *J. Neurosci.*, 14(7):4433–45.

Megías, M., Emri, Z., Freund, T. F., and Gulyás, A. I. (2001). Total number and distribution of inhibitory and excitatory synapses on hippocampal CA1 pyramidal cells. *Neuroscience*, 102(3):527–40.

Meltzer, J. A., Zaveri, H. P., Goncharova, I. I., Distasio, M. M., Papademetris, X., Spencer, S. S., Spencer, D. D., and Constable, R. T. (2008). Effects of working memory load on oscillatory power in human intracranial EEG. *Cereb. Cortex*, 18(8):1843–55.

Memmesheimer, R.-M. (2010). Quantitative prediction of intermittent high-frequency oscillations in neural networks with supralinear dendritic interactions. *Proc Natl Acad Sci U S A*, 107(24):11092–7.

Mizuseki, K., Diba, K., Pastalkova, E., and Buzsáki, G. (2011). Hippocampal CA1 pyramidal cells form functionally distinct sublayers. *Nat. Neurosci.*, 14(9):1174–81.

Naber, P. A., da Silva, F. H. L., and Witter, M. P. (2001). Reciprocal connections between the entorhinal cortex and hippocampal fields CA1 and the subiculum are in register with the projections from CA1 to the subiculum. *Hippocampus*, 11(2):99–104.

Nakashiba, T., Buhl, D. L., McHugh, T. J., and Tonegawa, S. (2009). Hippocampal CA3 output is crucial for ripple-associated reactivation and consolidation of memory. *Neuron*, 62(6):781–7.

Nakashiba, T., Young, J. Z., McHugh, T. J., Buhl, D. L., and Tonegawa, S. (2008). Transgenic inhibition of synaptic transmission reveals role of CA3 output in hippocampal learning. *Science*, 319(5867):1260–4.

Nguyen, D. P., Kloosterman, F., Barbieri, R., Brown, E. N., and Wilson, M. A. (2009). Characterizing the dynamic frequency structure of fast oscillations in the rodent hippocampus. *Front Integr Neurosci*, 3:11.

Nimmrich, V., Maier, N., Schmitz, D., and Draguhn, A. (2005). Induced sharp wave-ripple complexes in the absence of synaptic inhibition in mouse hippocampal slices. *J Physiol*, 563(Pt 3):663–70.

O'Keefe, J. (1976). Place units in the hippocampus of the freely moving rat. *Exp. Neurol.*, 51(1):78–109.

O'Keefe, J. and Recce, M. L. (1993). Phase relationship between hippocampal place units and the EEG theta rhythm. *Hippocampus*, 3(3):317–30.

Pangalos, M., Donoso, J. R., Winterer, J., Zivkovic, A. R., Kempter, R., Maier, N., and Schmitz, D. (2013). Recruitment of oriens-lacunosum-moleculare interneurons during hippocampal ripples. *Proc Natl Acad Sci U S A*, 110(11):4398–403.

Papatheodoropoulos, C., Sotiriou, E., Kotzadimitriou, D., and Drimala, P. (2007). At clinically relevant concentrations the anaesthetic/amnesic thiopental but not the anticonvulsant phenobarbital interferes with hippocampal sharp wave-ripple complexes. *BMC Neurosci*, 8:60.

Papp, E., Leinekugel, X., Henze, D. A., Lee, J., and Buzsáki, G. (2001). The apical shaft of CA1 pyramidal cells is under GABAergic interneuronal control. *Neuroscience*, 102(4):715–21.

Pastalkova, E., Itskov, V., Amarasingham, A., and Buzsáki, G. (2008). Internally generated cell assembly sequences in the rat hippocampus. *Science*, 321(5894):1322–7.

Patel, J., Fujisawa, S., Berényi, A., Royer, S., and Buzsáki, G. (2012). Traveling theta waves along the entire septotemporal axis of the hippocampus. *Neuron*, 75(3):410–7.

Pawelzik, H., Bannister, A. P., Deuchars, J., Ilia, M., and Thomson, A. M. (1999). Modulation of bistratified cell IPSPs and basket cell IPSPs by pentobarbitone sodium, diazepam and Zn2+: dual recordings in slices of adult rat hippocampus. *Eur. J. Neurosci.*, 11(10):3552–64.

Pawelzik, H., Hughes, D. I., and Thomson, A. M. (2002). Physiological and morphological diversity of immunocytochemically defined parvalbumin- and cholecystokinin-positive interneurones in CA1 of the adult rat hippocampus. *J. Comp. Neurol.*, 443(4):346–67.

Pfeiffer, B. E. and Foster, D. J. (2013). Hippocampal place-cell sequences depict future paths to remembered goals. *Nature*, 497(7447):74–9.

Ponomarenko, A. A., Korotkova, T. M., Sergeeva, O. A., and Haas, H. L. (2004). Multiple GABAA receptor subtypes regulate hippocampal ripple oscillations. *Eur. J. Neurosci.*, 20(8):2141–8.

Ribot, T. and Fitzgerald, J. (1883). *The diseases of memory.* Number 46. Fitzgerald.

Samsonovich, A. V. and Ascoli, G. A. (2005). A simple neural network model of the hippocampus suggesting its pathfinding role in episodic memory retrieval. *Learning & Memory*, 12(2):193–208.

Schlingloff, D., Káli, S., Freund, T. F., Hájos, N., and Gulyás, A. I. (2014). Mechanisms of sharp wave initiation and ripple generation. *J. Neurosci.*, 34(34):11385–98.

Schnitzler, A. and Gross, J. (2005). Normal and pathological oscillatory communication in the brain. *Nature reviews neuroscience*, 6(4):285–296.

Scoville, W. B. and Milner, B. (2000). Loss of recent memory after bilateral hippocampal lesions. 1957. *J Neuropsychiatry Clin Neurosci*, 12(1):103–13.

Sederberg, P. B., Schulze-Bonhage, A., Madsen, J. R., Bromfield, E. B., McCarthy, D. C., Brandt, A., Tully, M. S., and Kahana, M. J. (2007). Hippocampal and neocortical gamma oscillations predict memory formation in humans. *Cereb. Cortex*, 17(5):1190–6.

Senior, T. J., Huxter, J. R., Allen, K., O'Neill, J., and Csicsvari, J. (2008). Gamma oscillatory firing reveals distinct populations of pyramidal cells in the CA1 region of the hippocampus. *J. Neurosci.*, 28(9):2274–86.

Shu, Y., Hasenstaub, A., Duque, A., Yu, Y., and McCormick, D. A. (2006). Modulation of intracortical synaptic potentials by presynaptic somatic membrane potential. *Nature*, 441(7094):761–5.

Shu, Y., Yu, Y., Yang, J., and McCormick, D. A. (2007). Selective control of cortical axonal spikes by a slowly inactivating K+ current. *Proc. Natl. Acad. Sci. U.S.A.*, 104(27):11453–8.

Siapas, A. G. and Wilson, M. A. (1998). Coordinated interactions between hippocampal ripples and cortical spindles during slow-wave sleep. *Neuron*, 21(5):1123–8.

Sik, A., Penttonen, M., Ylinen, A., and Buzsáki, G. (1995). Hippocampal CA1 interneurons: an in vivo intracellular labeling study. *J. Neurosci.*, 15(10):6651–65.

Slomianka, L., Amrein, I., Knuesel, I., Sørensen, J. C., and Wolfer, D. P. (2011). Hippocampal pyramidal cells: the reemergence of cortical lamination. *Brain Struct Funct*, 216(4):301–17.

Smith, H. M. (1935). Synchronous Flashing of Fireflies. *Science*, 82(2120):151–152.

Somogyi, P., Katona, L., Klausberger, T., Lasztóczi, B., and Viney, T. J. (2014). Temporal redistribution of inhibition over neuronal subcellular domains underlies state-dependent rhythmic change of excitability in the hippocampus. *Phil. Trans. R. Soc. B*, 369(1635):20120518.

Somogyi, P., Nunzi, M. G., Gorio, A., and Smith, A. D. (1983). A new type of specific interneuron in the monkey hippocampus forming synapses exclusively with the axon initial segments of pyramidal cells. *Brain Res.*, 259(1):137–42.

Stark, E., Roux, L., Eichler, R., Senzai, Y., Royer, S., and Buzsáki, G. (2014). Pyramidal cell-interneuron interactions underlie hippocampal ripple oscillations. *Neuron*, 83(2):467–80.

Sullivan, D., Csicsvari, J., Mizuseki, K., Montgomery, S., Diba, K., and Buzsáki, G. (2011). Relationships between hippocampal sharp waves, ripples, and fast gamma oscillation: influence of dentate and entorhinal cortical activity. *J. Neurosci.*, 31(23):8605–16.

Takács, V. T., Klausberger, T., Somogyi, P., Freund, T. F., and Gulyás, A. I. (2012). Extrinsic and local glutamatergic inputs of the rat hippocampal CA1 area differentially innervate pyramidal cells and interneurons. *Hippocampus*, 22(6):1379–91.

Taxidis, J., Coombes, S., Mason, R., and Owen, M. R. (2012). Modeling sharp wave-ripple complexes through a CA3-CA1 network model with chemical synapses. *Hippocampus*, 22(5):995–1017.

Thomson, A. M., Bannister, A. P., Hughes, D. I., and Pawelzik, H. (2000). Differential sensitivity to Zolpidem of IPSPs activated by morphologically identified CA1 interneurons in slices of rat hippocampus. *Eur. J. Neurosci.*, 12(2):425–36.

Traub, R. D. and Bibbig, A. (2000). A model of high-frequency ripples in the hippocampus based on synaptic coupling plus axon-axon gap junctions between pyramidal neurons. *J Neurosci*, 20(6):2086–93.

Traub, R. D., Schmitz, D., Jefferys, J. G., and Draguhn, A. (1999). High-frequency population oscillations are predicted to occur in hippocampal pyramidal neuronal networks interconnected by axoaxonal gap junctions. *Neuroscience*, 92(2):407–26.

Traub, R. D., Schmitz, D., Maier, N., Whittington, M. A., and Draguhn, A. (2012). Axonal properties determine somatic firing in a model of in vitro CA1 hippocampal sharp wave/ripples and persistent gamma oscillations. *Eur J Neurosci*, 36(5):2650–60.

Traub, R. D., Whittington, M. A., Colling, S. B., Buzsáki, G., and Jefferys, J. G. (1996). Analysis of gamma rhythms in the rat hippocampus in vitro and in vivo. *J. Physiol. (Lond.)*, 493 (Pt 2):471–84.

Valero, M., Cid, E., Averkin, R. G., Aguilar, J., Sanchez-Aguilera, A., Viney, T. J., Gomez-Dominguez, D., Bellistri, E., and de la Prida, L. M. (2015). Determinants of different deep and superficial CA1 pyramidal cell dynamics during sharp-wave ripples. *Nat. Neurosci.*, 18(9):1281–90.

Van Strien, N., Cappaert, N., and Witter, M. (2009). The anatomy of memory: an interactive overview of the parahippocampal–hippocampal network. *Nature Reviews Neuroscience*, 10(4):272–282.

Varela, F., Lachaux, J. P., Rodriguez, E., and Martinerie, J. (2001). The brainweb: phase synchronization and large-scale integration. *Nat. Rev. Neurosci.*, 2(4):229–39.

Varga, C., Golshani, P., and Soltesz, I. (2012). Frequency-invariant temporal ordering of interneuronal discharges during hippocampal oscillations in awake mice. *Proc. Natl. Acad. Sci. U.S.A.*, 109(40):E2726–34.

Viereckel, T., Kostic, M., Bähner, F., Draguhn, A., and Both, M. (2013). Effects of the GABA-uptake blocker NNC-711 on spontaneous sharp wave-ripple complexes in mouse hippocampal slices. *Hippocampus*, 23(5):323–9.

Wang, S.-H., Teixeira, C. M., Wheeler, A. L., and Frankland, P. W. (2009). The precision of remote context memories does not require the hippocampus. *Nat. Neurosci.*, 12(3):253–5.

Wang, X. J. and Buzsáki, G. (1996). Gamma oscillation by synaptic inhibition in a hippocampal interneuronal network model. *J Neurosci*, 16(20):6402–13.

Whittington, M. A., Jefferys, J. G., and Traub, R. D. (1996). Effects of intravenous anaesthetic agents on fast inhibitory oscillations in the rat hippocampus in vitro. *Br. J. Pharmacol.*, 118(8):1977–86.

Whittington, M. A., Traub, R. D., and Jefferys, J. G. (1995). Synchronized oscillations in interneuron networks driven by metabotropic glutamate receptor activation. *Nature*, 373(6515):612–5.

Whittington, M. A., Traub, R. D., Kopell, N., Ermentrout, B., and Buhl, E. H. (2000). Inhibition-based rhythms: experimental and mathematical observations on network dynamics. *Int J Psychophysiol*, 38(3):315–36.

Wouterlood, F. G., Saldana, E., and Witter, M. P. (1990). Projection from the nucleus reuniens thalami to the hippocampal region: light and electron microscopic tracing study in the rat with the anterograde tracer Phaseolus vulgaris-leucoagglutinin. *J. Comp. Neurol.*, 296(2):179–203.

Ylinen, A., Bragin, A., Nádasdy, Z., Jandó, G., Szabó, I., Sik, A., and Buzsáki, G. (1995). Sharp wave-associated high-frequency oscillation (200 Hz) in the intact hippocampus: network and intracellular mechanisms. *J Neurosci*, 15(1 Pt 1):30–46.

Zarnowska, E. D., Keist, R., Rudolph, U., and Pearce, R. A. (2009). GABAA receptor alpha5 subunits contribute to GABAA,slow synaptic inhibition in mouse hippocampus. *J. Neurophysiol.*, 101(3):1179–91.

Acknowledgements

In one way or another, many people have contributed to the development of the work presented here.

First of all, I would like to thank Richard Kempter for his meticulous advice and patience. Throughout these years he has been the main provider of motivation and support.

I would like to thank the people from the Schmitzlab, who have consistently helped me to keep my feet to the ground: Dietmar Schmitz for giving support, and at the same time, keeping a healthy resistance to my views; Prateep Beed for his friendship and refreshing attitude towards science, and Anja Gundlfinger for the introduction in experimental procedures. I would like to specially thank my two most important collaborators, Nikolaus Maier and Maria Pangalos: working with you guys has been such an enriching experience in so many aspects. I hope you have learned from me at least a fraction of what I've learned from you.

I would like to thank my officemates: Robert Schmidt and Paula Kuokkanen for all the help and support at the beginning of my studies; Jorge Jaramillo for all the good fun; Thomas McColgan and Nikolai Chenkov for the python advice; Martina Michalikova for the stress-relieving and Andre Holzbecher for the feedback on the text. All of them have been a source of joy and interesting discussions throughout these years.

Many great thanks to those who helped me get started with my thesis: Jan-Hendrik Schleimer and Jorge Jaramillo, and to those who helped me getting it done: Maria Pangalos, Nikolaus Maier, Nikolai Chenkov, André Holzbecher and Eric Reifenstein.

Finally, I would like to thank all my friends who, knowingly or not, provided support in the difficult times: Francisca Albert; Marcos Barra; Florencia Campetella, who also provided valuable feedback; Marisol Castillo; Isabel Kuklinski; Carla Messenger; Pedro Ortega; Rodrigo Santa María, Alvaro Recabarren; Eric Reifenstein; Rodrigo Sigala; Jorge Urzua and Brunel Wester, who also contributed with illustrations. I would like to specially thank Irene Selka for her support and company during the most difficult periods.

Selbständigkeitserklärung

Ich erkläre, dass ich die vorliegende Arbeit selbständig und nur unter Verwendung der angegebenen Literatur und Hilfsmittel angefertigt habe.

Berlin, December 2, 2016 José Ramón Donoso Leiva